PRODUCTION OF OMEGA AND PHI MESONS BY 193 GEV/C PIONS AND 250 GEV/C PROTONS ON A BERYLLIUM TARGET

BY

JAMES NUGENT BELLINGER

B.S., Southern Illinois University, 1977
M.S., University of Illinois (Chicago Circle), 1979

THESIS

Submitted in partial fulfillment of the requirements
for the degree of Doctor of Philosophy in Physics
in the Graduate College of the
University of Illinois at Urbana-Champaign, 1985

Urbana, Illinois

PRODUCTION OF OMEGA AND PHI MESONS BY 193 GEV/C PIONS AND 250 GEV/C PROTONS ON A BERYLLIUM TARGET

James Nugent Bellinger, Ph.D.
Department of Physics
University of Illinois at Urbana-Champaign, 1985

Omegas and phis were observed in di-muon events. Differential cross sections with respect to perpendicular momentum and Feynman-X for both meson types and both beam types are compared. When a simple parton fusion model is used to describe the Feynman-X distributions the omega appears to be produced predominantly by gluon fusion.

Acknowledgements

This thesis is based on an experiment to which I was a relative latecomer. Therefore, the list of those to whom I am indebted is long.

First, I thank my wife Eva, for her love and her support and her endurance.

I thank my advisor, Dr. Lee Holloway, for his instruction, advice, and encouragement, and his insistence on testing by hand, to make sure one has a feel for the physics.

My fellow students and co-workers deserve and have my gratitude for their friendship and their contributions to this experiment, and the many, sometimes fruitful, discussions we have had. Thomas Graff, Wei Guo Li, and Patrick Lukens worked and studied together with me on E673. Our predecessors, Howard Budd, Steven Hahn, and Paul Schoessow, helped build both experiments, in effect, and I gratefully acknowledge their labors and recall their advice.

The post-docs, George Alverson, Selcuk Cihangir, and Inga Karliner, contributed much to the experiment and gave me valuable aid. So did the professors who worked with us; Louis Koester, Robert Sard, Guilio Ascoli, Ulrich Kruse; and I must not forget Lorella

Jones and James Wiss, with whom I have had useful discussions.

I am also indebted to other workers on our experiment; John Cooper, our spokesman, Dan Bauer, Stephen Pordes, Jeff Wilson, Chris Davis, Alvin Laasanen, Jim Simmons, Thomas Kirk, Art Garfinkel, William Oliver, Alan Wehmann, Virgil Barnes, and Ron Thornton. Together, we formed a dedicated team; and I have learned from their enthusiasm, competence, and patience.

I am grateful for, and continually impressed by, the professionalism, friendliness, and patience of Dave Lesny and Jerry Wray of the University of Illinois physics computing staff. Vaidotas Simaitis and Robert Downing helped me understand how the electronics they built worked. I also wish to thank the many at Fermilab who supported and maintained their machinery and computing facilities: they perform smoothly and efficiently - and from my point of view, invisibly - but I know they are there and am grateful.

My thanks also go out the the taxpayers of the United States, who supported this research with U.S. Department of Energy Contract Number DE-AC02-76ER1195.

Last, but hardly least, I here express my thanks to Him who not only made us all, but made a world for us to explore.

TABLE OF CONTENTS

Introduction

I base this thesis on the data accumulated by Fermilab experiment number 673 of 1982. John Cooper was spokesman for our collaboration, which included physicists from the University of Illinois at Urbana, Fermilab, Purdue University, the University of Pennsylvania, and Tufts University.

The experiment was designed to study the production of charmonium states by pions and protons striking a beryllium target. We chose to study the chi states by observing their decays via gamma emission to the J/psi meson, which in turn decays to two muons. Our apparatus was designed to trigger on these high mass di-muons, but we have a substantial number of low mass di-muon events as well, in particular, very clear omega and phi signals. (Figure 1-1 and Figure 1-2)

Our open geometry, with the famous Chicago Cyclotron magnet as our spectrometer magnet, gave us good resolution, sufficient to distinguish the omega signal from the rho signal, though at the price of a large background from pion decays in flight. In consequence, we see the omega very plainly, but find the rho almost washed out in the background. The phi peak is clear, but is perched on a large background; so measurements of it are subject to larger errors than measurements of the omega.

I chose to study the differences in production of omegas and phis when produced by protons and pions, as displayed in the distributions of perpendicular momentum and Feynman-x of the omegas and phis. Insofar as these mesons are produced directly, by simple interactions of partons rather than decay of higher mass resonances, their distributions reflect the aboriginal parton distributions.

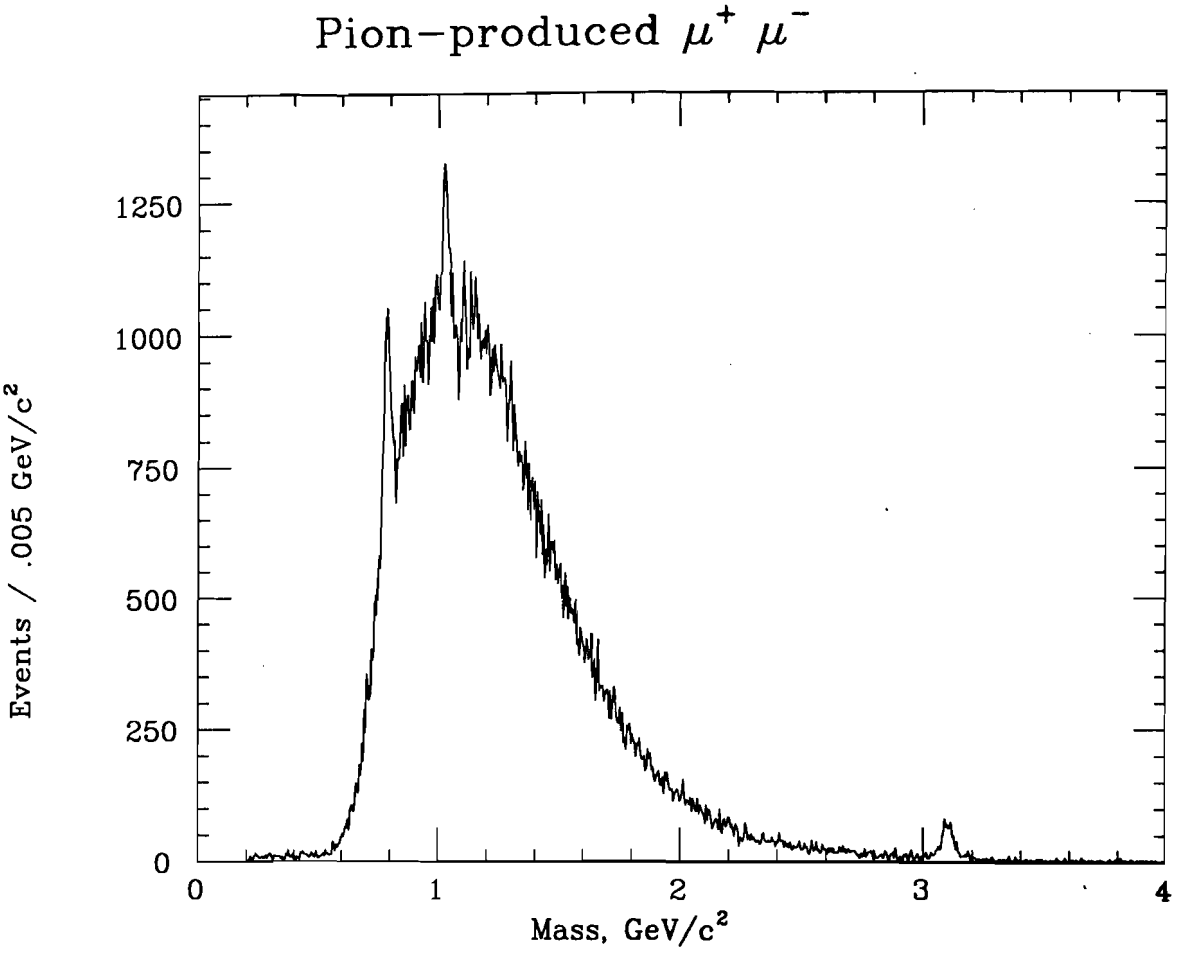

Figure 1-1

E673 di-muon spectrum
193 GeV/c negative pions on Be
Events per 0.005 GeV/c**2

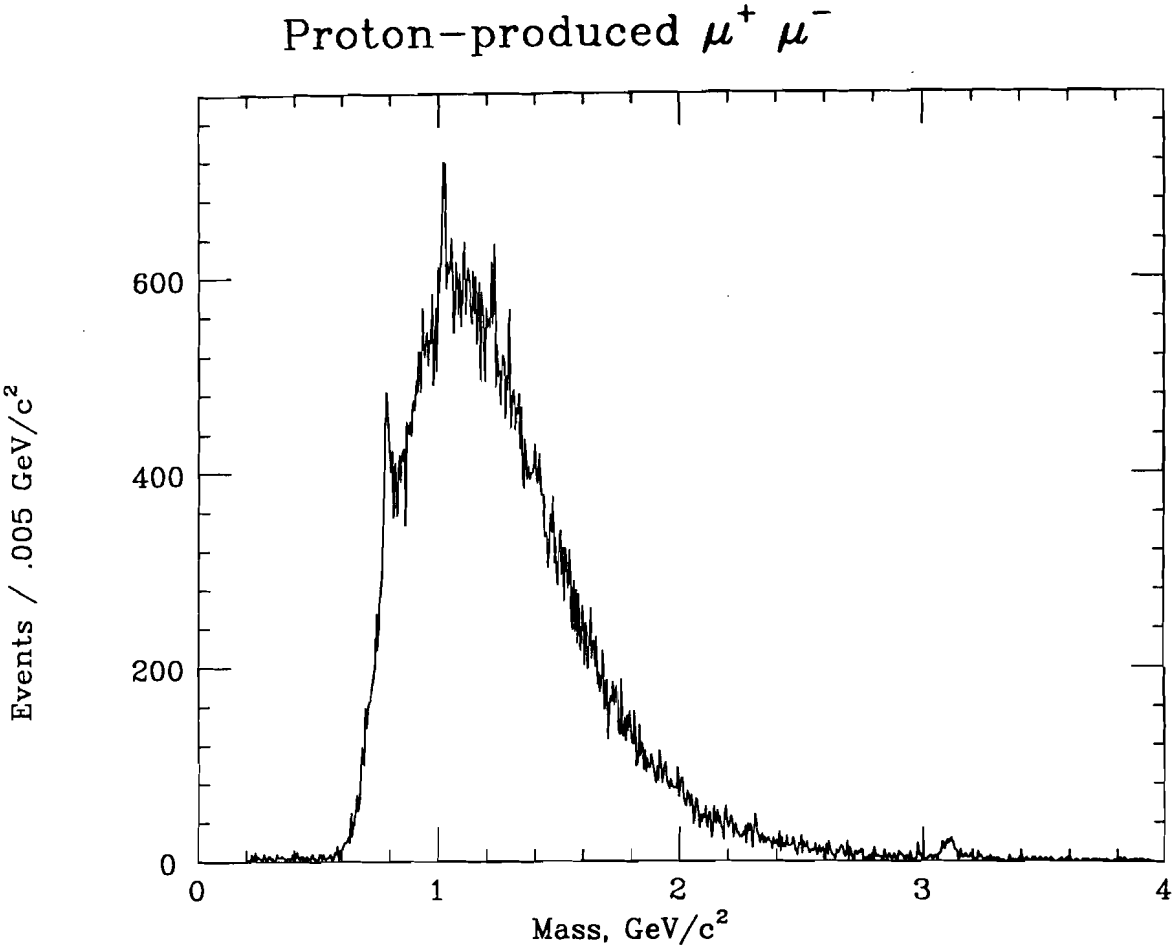

Figure 1-2

E673 di-muon spectrum
250 GeV/c protons on Be
Events per 0.005 GeV/c**2

Theory

2.1 Studying Partons

One approach to studying quark distributions inside particles —protons, for example—is to study the distributions of the mesons produced in collisions. If a meson is formed by simple fusion of a quark from one proton and an anti-quark from another proton, and if both quarks are representative of all similar partons in their respective protons, then the Feynman-X (see Table 2-1, Definitions) and perpendicular momentum distributions of the meson are completely and simply determined by the Feynman-X and perpendicular momentum distributions of the quarks and anti-quarks in the proton. There are other possible simple models of meson formation, such as gluon fusion and color evaporation, but the principle remains virtually the same.

For example, consider the perpendicular momentum distribution of partons relative to the center of mass of the proton. If this distribution is gaussian, (as suggested by Feynman, Ref 33) with a sigma of A for the up quark and B for the anti-up quark, a meson formed by fusing an up quark from one proton and an anti-up quark from another proton will have a perpendicular momentum distribution

which is gaussian distributed with a sigma which is the square root of the sum of the squares of A and B.

The above argument does not apply to pions and kaons: these are copiously produced by decays of other hadrons, and have perpendicular momentum distributions skewed to low values, so that their distributions fall much more steeply than the other light mesons. (See Ref 42, 51)

Unfortunately, the above model relies heavily on the assumption that the partons, and the resulting meson, undergo no other interactions. There is an alternative model, for the other extreme, the thermodynamic or "fireball" model (for example, see M. Perl, High Energy Hadron Physics, Wiley, 1974). In this model, partons undergo so many interactions in the process of forming new hadrons that the distribution of hadrons with respect to momentum comes to depend solely on their respective energies, rather than on any structure in the original parton distributions. Since most of the partons have the greatest part of their momentum in a longitudinal direction, rather than perpendicular, one could argue that most of the momentum smearing (due to multiple interactions) will be in the longitudinal direction and that the perpendicular momentum distributions will be less affected. This simple model predicts a distribution of particles with respect to energy given by

$$\frac{d\sigma}{dE} = C\frac{E^2}{e^{E\beta}-1} \qquad \beta \equiv \frac{1}{kT}$$

where k is Boltzmann's constant and T is the temperature in degrees

Kelvin. This model, though primitive, has been fairly successful in predicting the behavior of centrally-produced hadrons.

Recent results from a muon scattering experiment (Arneodo et al, Ref 9) suggest that the Lund string fragmentation model, including soft gluon emission and a relatively low average perpendicular momentum of the quark, fits the data better than simply attributing the hadron's perpendicular momentum to the quarks, especially for hadrons moving backwards in the center of mass frame. They find that these hadrons have an average perpendicular momentum which rises more slowly with increasing absolute value of Feynman-X than do the hadrons moving forward in the center of mass frame. This they attribute to the extra Pperp given the forward-going "struck parton" by the recoil of the soft gluon it subsequently emits.

We have very low acceptance for particle moving backwards in the center of mass frame, so we cannot test their model, but I offer it as an alternative interpretation of the results.

2.2 Naive Parton Model

Let us assume that the parton fusion model describes the production of omega and phi mesons well. If one knows the distribution of the fraction of momentum each variety of parton

Table 2-1

Definitions

Pbeam	=	4-momentum of the beam particle
Plab	=	magnitude of the momentum of the beam particle in the lab frame
Mb	=	Mass of the beam particle (pion or proton)
Ptarg	=	4-momentum of the target particle
Mt	=	Mass of the target particle (proton or neutron)
s	=	total energy squared of the interaction
	=	(Pbeam + Ptarg)**2
	=	Mb**2 + Mt**2 + 2 * Mt * SQRT(Mb**2 + Plab**2)
Px	=	component of a particle's momentum in the x-direction
Py	=	component of a particle's momentum in the y-direction
Pz	=	component of a particle's momentum in the z-direction (which is the beam direction)
E	=	total energy of a particle
XF	=	Feynman-X, fraction of available longitudinal momentum carried by a particle of mass M in the center of mass frame
	=	Pzcm / SQRT(s/4 - M*M)
Pperp	=	magnitude of the momentum component perpendicular to the beam direction
	=	SQRT(Px*Px + Py*Py)
Ycm	=	rapidity in the center-of-mass frame
	=	0.5 * ln((E + Pz) / (E - Pz))

carries in each of the colliding hadrons, then it is straightforward to predict the distributions of the resulting hadrons in terms of first order processes. Higher order processes are far more difficult, and sometimes not well understood, and will not be considered in this thesis. The three lowest order production processes, not including decays, are light quark fusion, heavy quark fusion, and gluon fusion (Figure 2-1).

Since these parton interactions occur in an environment populated by a "sea" of gluons which is weighted to the low momentum (soft) end of the spectrum, I assume that if two partons fuse to form a colored state, a zero momentum gluon will carry off the color, leaving the meson in the color singlet state. This will not always be a good approximation, as is shown in Ref 9 and Ref 23, in which soft gluon emission is seen to substantially increase the Pperp of muons and cause an excessive rise in the production cross section of the J/psi respectively.

As a further simplification, I neglect all heavy quarks save the strange quark, and further neglect its contribution to omega production. Despite omega/phi mixing, this last should be a fair approximation, since the light quark components dominate in the omega and in the interacting hadrons. The light quark masses are assumed to be zero; and both flavors of light quark are assumed to have the same coupling in the interaction (the latter assumption based on the isospin invariance of the resulting meson).

The cross-section may be described by the following form, in the naive first approximation:

$$\frac{d\sigma}{dx_F} = \left\{ \begin{array}{l} \frac{q_H^2}{4\pi}\left(F_b^S(x_1)F_T^{\bar{S}}(x_2) + F_b^{\bar{S}}(x_1)F_T^S(x_2)\right) \\ + \\ \frac{q_L^2}{4\pi}\left(F_b^U(x_1)F_T^{\bar{U}}(x_2) + F_b^{\bar{U}}(x_1)F_T^U(x_2) \right. \\ \left. + F_b^d(x_1)F_T^{\bar{d}}(x_2) + F_b^{\bar{d}}(x_1)F_T^d(x_2)\right) \\ + \\ \frac{q_G^2}{4\pi} G_b(x_1)\, G_T(x_2) \end{array} \right\} \qquad \begin{array}{l} x_1 - x_2 = x_F \\ x_1 x_2 = \frac{m^2}{s} \end{array}$$

The F's are quark and anti-quark Feynman-X distribution functions, for the beam (b) particle and the target (T) particle respectively. The G's are the gluon distribution functions. The initial "constant" C is actually a function of the center-of-mass energy squared, or "s". Since we do not fully understand our beam (especially the proton beam) or our "live time," I will not be studying the cross sections, but instead ratios of the "g" values and the relative production rates due to these first order processes.

X1 and X2 are readily expressible in terms of XF of the resulting meson, the meson's mass, the parton masses, and the center-of-mass energy.

$$x_1 = \frac{1}{2}\left(x_F + \sqrt{x_F^2 + 4\lambda}\right) \qquad x_2 = \frac{1}{2}\left(-x_F + \sqrt{x_F^2 + 4\lambda}\right)$$

$$\lambda \equiv \frac{m^2}{s}$$

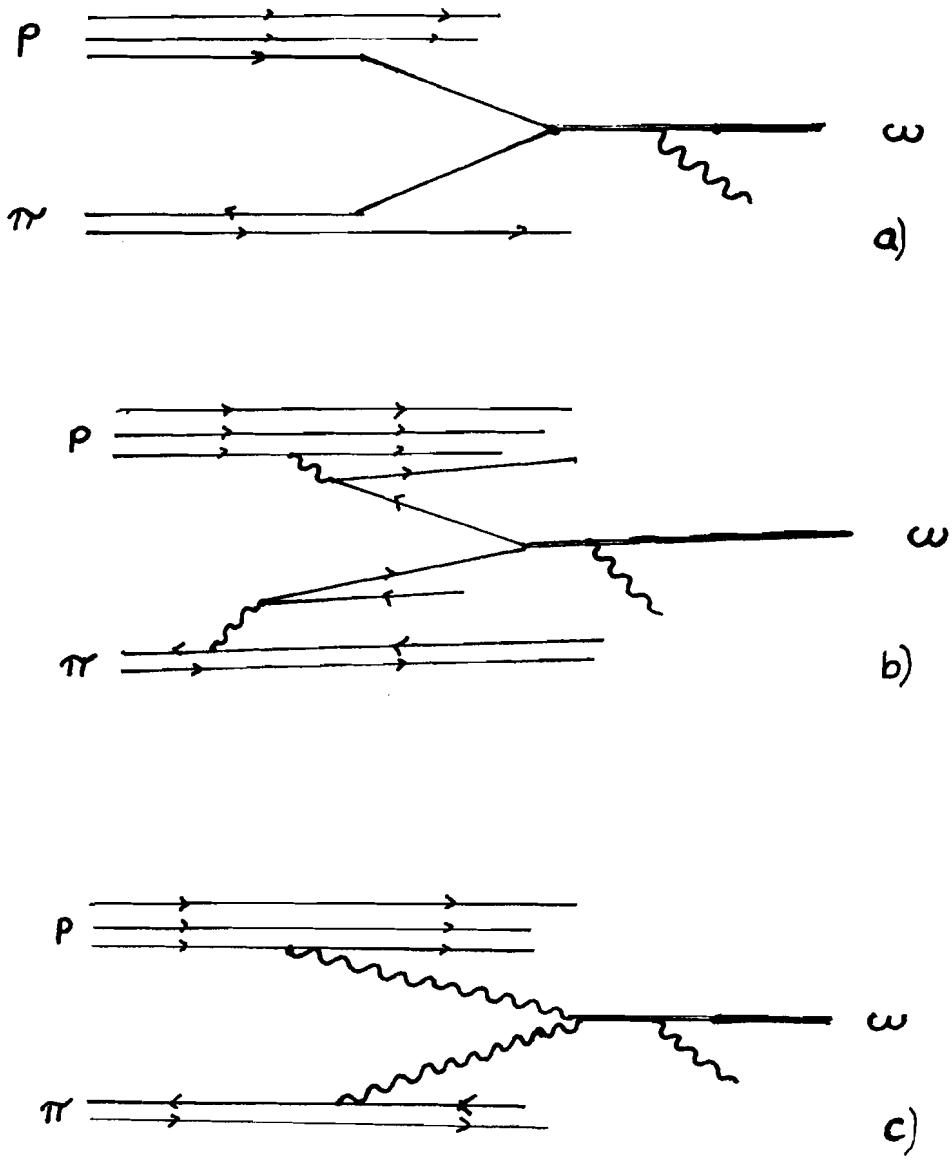

Figure 2-1

Diagrams of elementary processes
a) light quark fusion
b) heavy quark fusion
c) gluon fusion

Each of the combinations of parton distributions in the expression for the differential cross section form independent "product distributions" in XF: one for strange quark fusion, one for light quark fusion and one for gluon fusion. Notice that these "product distributions" are like convolutions of the parton distributions. A product distribution depends on the mass of the resulting meson, so a distribution calculated for one meson is not suitable for use with another.

I treat these product distributions as absolute and vary their coefficients "g" to obtain the best fit to my XF product distributions, and attempt to determine their true ratios. Further, each of these independent product distributions has a different integral; I therefore take the ratio of the products of the "g" and the definite integrals of their respective product distributions, and determine the ratio of production of the meson due to the various processes.

2.3 Parton Distribution Functions

Unfortunately, the parton distribution functions are not well known, and there is considerable variation in their descriptions. I examine four different collections of parton distribution functions, with special emphasis on those collected by Kuhn (Ref 54) and those collected by Daum et al (ACCMOR, Ref 32). These are summarized in Table 2-2, and sample product distributions are displayed in Figure

2-2. The pion is assumed to be negative. Notice the similarity of the Kuhn and Daum product distributions.

Independent attempts to measure the gluon distribution function (Wahlen, Ref 72, and Para, Ref 63) find gluon distributions for iron of the form

$$x\,G(x) = 2.62\ (1.0 + 3.5\,x)\ (1-x)^{**}A \qquad A = 5.9 \pm 0.5$$

which is roughly consistent with $(1-x)^{**}5$. A separate experiment (NA-3, Charpentier, Ref 17)finds

$$x\,G(x) = c\ (1-x)^{**}A \qquad A = 5.1 \pm 0.3 \text{ for protons}$$
$$A = 2.38 \pm 0.12 \text{ for pions}$$

The pion valence quark distribution was found (Varela, NA-10, Ref 71) to be, when high-mass (> 4.0 GeV/c**2) di-muons were present,

$$x\,V(x) = c\ x^{**}A\ (1-x)^{**}B \qquad A = 0.38 \pm 0.02 \pm 0.04$$
$$B = 1.12 \pm 0.03 \pm 0.02$$

when assuming

$$x\,S(x) = c\ (1-x)^{**}D \qquad D = 8.7 \text{ pion}$$
$$x\,S(x) = c\ (1-x)^{**}D \qquad D = 8.0 \text{ proton}$$

and (CDHS)

$$x\,U(x) = c\ x^{**}A\ (1-x)^{**}B \qquad A = 0.51 \pm 0.02 \text{ proton}$$
$$B = 2.83 \pm 0.10 \text{ proton}$$

I combined the Wahlen gluon distribution for iron, the Charpentier distribution for pion gluons, and the Varela distributions for pion

quarks, and called the result the Moriond distribution. I took distributions for proton down quarks and proton sea quarks from the Daum et al distributions. The Moriond distributions are included for comparison only, as they have been determined for momentum transfers greater than 4 or 5 GeV/c, and are unsuitable for low mass di-muons. One group integrated the Alterelli-Parisi equations to describe the evolution of the parameters with increasing momentum transfer, but unfortunately this does not work backwards: I get rubbish if I try to extrapolate the parameters to the the region of the omega mass.

The Varela (Ref 71) paper included plots of the parameters for valence pion quarks, which I used to extrapolate linearly back to estimate the distribution at Q = Ø.782. I find

$$x\,V(x) = c * x^{**}A * (1-x)^{**}B \qquad A = Ø.17 \;+/-\; Ø.Ø9$$
$$B = Ø.7Ø2 \;+/-\; Ø.231$$

Nothing similar seems to be available for the proton.

Two recent papers proffered parameterizations intended to be valid for Q > 2.Ø GeV/c for the proton (Gluck, Ref 4Ø) and the pion (Owens, Ref 62). Those for the proton used a different parameterization from the rest I have used. In order to be able to compare them with other work, I refit his parameterization to the x**A * (1-x)**B form by minimizing the integrated deviation between his function and mine. The combination of these two sets of distributions I call the TWOQ set.

Notice that as the value of Q declines, the distribution function for pion valence quarks becomes "harder", in the sense that it includes more high momentum fraction particles. The situation for gluons is less clear, but it is supposed to become harder as well.

For this model, and these sets of distributions, the product distributions are dominated by the distributions of the partons in the beam. Thus, if a meson is formed solely by simple parton fusion, one would expect that as the Q**2 declined, the meson would carry off a greater fraction of the interaction energy, on the average.

2.1 Expectations For Omega Production

Other experiments (Ref 51, 12, 1) have found an omega:rho ratio of about 1:1, though Antipov et al (Ref 6) found that the ratio declined with increasing XF. They interpreted this as reflecting an excess of rho mesons from "diffractive scattering" (excitation followed by disintegration) of the beam particle (pion) for XF > Ø.6, but similar production mechanisms for rho and omega when XF < Ø.6 . Most omegas and rhos seemed to be produced in the central (low XF) region. The results of Higgens et al (Ref 47) are consistent with dominantly centrally produced rhos (they did no omega studies). In Ref 57 it is argued that for rho production by 16 GeV/c pions, rho production by "beam fragmentation" (diffractive scattering) dominates central (low XF) production by 3.1 +/- Ø.3 mb to 1.6 +/- Ø.5 mb.

Table 2-2

Parton Distribution Functions

Type	Parton	Function	
		Daum	Kuhn
Pion	down =up-bar	0.55 (1-x)**0.9 x**0.4	0.75 (1-x)**1.0 * x**0.5
Pion	up-bar =down =strange =strange-bar	0.09 (1-x)**4.4	0.10 (1-x)**5.0
Proton	up	1.09 (1-x)**3.0 x**0.5	1.74 (1-x)**2.61 * (1 + 2.3*x) * x**0.5
Proton	down	1.23 (1-x)**4.0 x**0.5	1.11 (1-x)**3.1 * x**0.5
Proton	up-bar =down-bar =strange =strange-bar	0.17 (1-x)**6.0	0.26 (1-x)**9.0
Pion	gluon	2.0 (1-x)**3.0	0.25 (1-x)**3.0
Proton	gluon	2.5 (1-x)**4.0	0.375 (1-x)**5.0

Table 2-2
(continued)
Parton Distribution Functions

Type	Parton	Function Moriond (Q**2 > 25(GeV/c)**2)
Pion	down =up-bar	1.0 (1-x)**1.12 x**0.38
Pion	up-bar =down =strange =strange-bar	1.0 (1-x)**8.7
Proton	up	1.0 (1-x)**2.83 x**0.51
Proton	down	1.23 (1-x)**4.0 x**0.5
Proton	up-bar =down-bar =strange =strange-bar	0.17 (1-x)**8.0
Pion	gluon	2.0 (1-x)**2.83
Proton	gluon	1.0 (1-x)**5.9 * (1.0 + 3.5*x)

Table 2-2
(continued)
Parton Distribution Functions

Type	Parton	Function TWOQ (Q = 2 GeV/c)
Pion	down =up-bar	1.Ø (1-x)**Ø.7 x**Ø.4
Pion	up-bar =down =strange =strange-bar	1.Ø (1-x)**5
Proton	up	1.Ø (1-x)**1.56 x**Ø.335
Proton	down	1.Ø (1-x)**2.Ø6 x**Ø.282
Proton	up-bar =down-bar =strange =strange-bar	1.Ø (1-x)**7.Ø
Pion	gluon	1.Ø (1-x)**3.11 * (1.Ø + 6.Ø*x)
Proton	gluon	1.Ø (1-x)**5

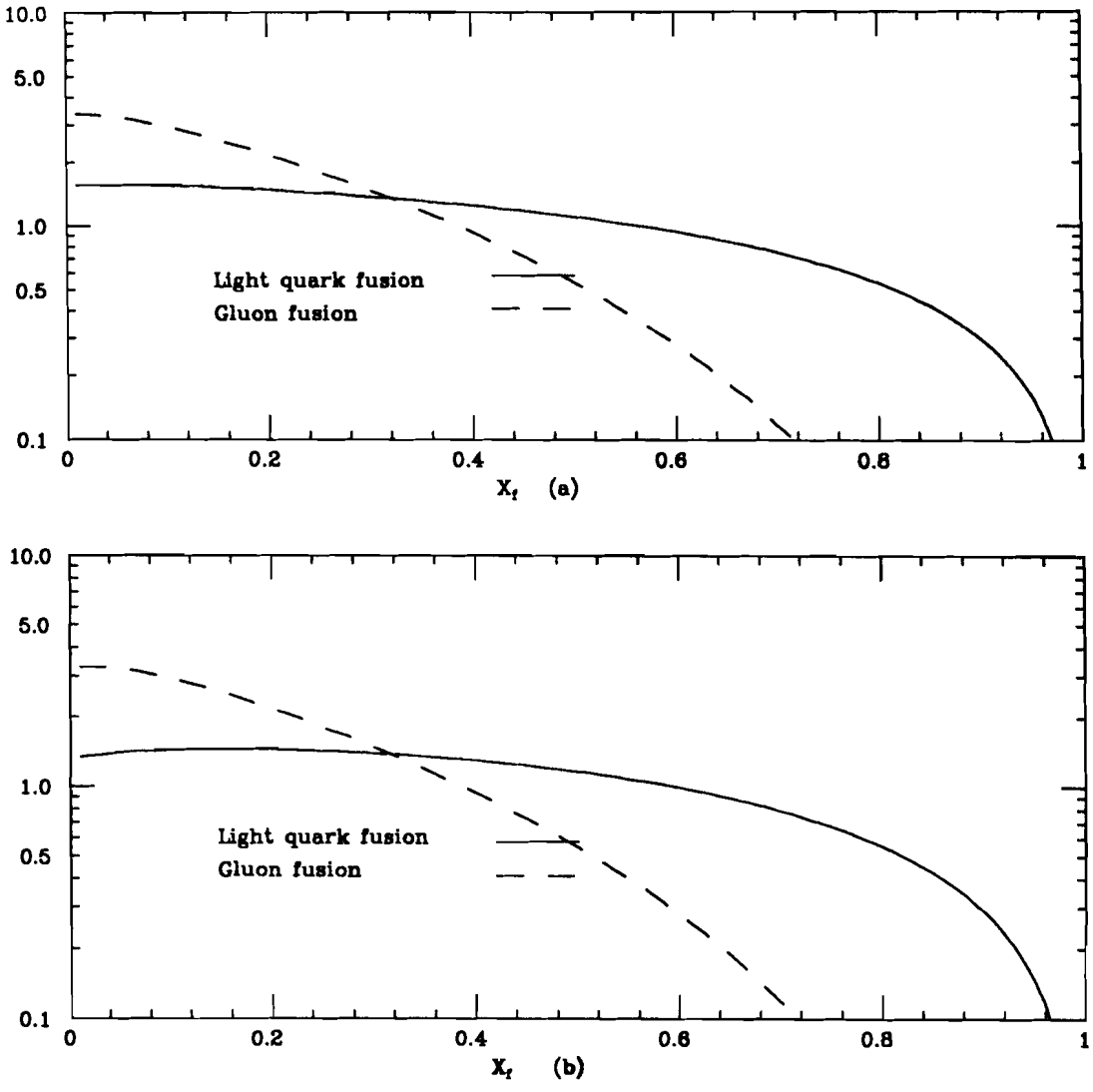

Figure 2-2

Comparison of product distributions for pion-produced omegas with a beryllium target
Distributions are normalized.
a) from Daum et al parton distributions
b) from Kuhn parton distributions

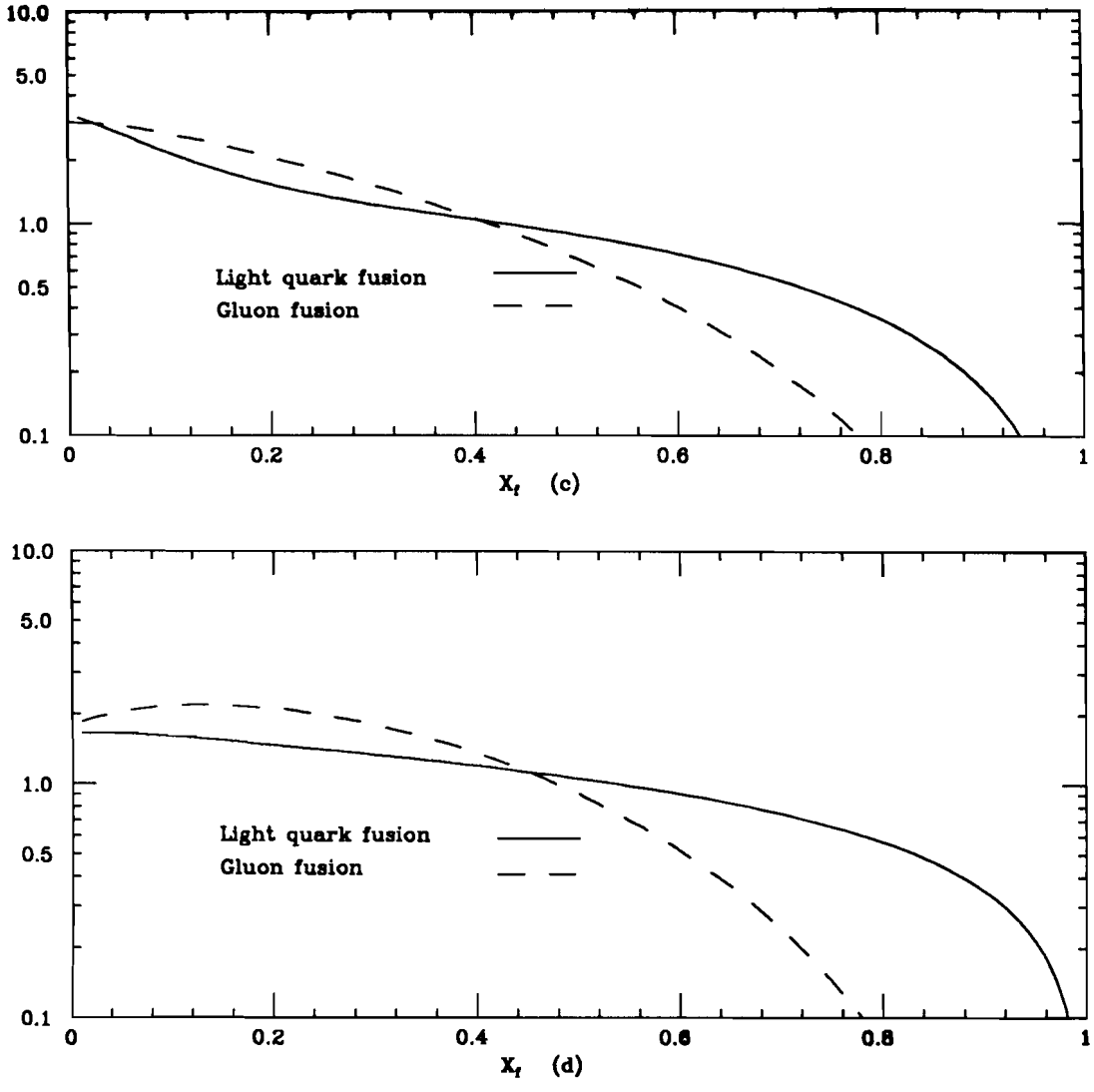

Figure 2-2
(continued)

Comparison of product distributions for pion-produced omegas with a beryllium target
Distributions are normalized.
c) from the Moriond distributions
d) from the TWOQ distributions

At 40 GeV/c, (Ref 44) central production dominates; and the ratios of rhos produced by various interactions are consistent, in their central region (-1.0 < Ycm < 1.0), with models in which both valence quarks from the beam pion interact. Ycm is the rapidity in the center-of-mass, defined in Table 2-1.

Thus, except for the beam fragmentation region, in which one may have an excess of rho mesons, rho and omega mesons are produced in equal numbers in the same regions of the interaction. Since rho production, once again excepting the beam fragmentation region, is consistent with quark fusion, we may infer that omegas are likewise produced by quark fusion.

In this experiment, as shall be later shown, I study a portion of the central production region (0.1 < XF < 0.3) and a portion of the forward region (0.3 < XF < 0.7). In this intermediate region I will test the naive parton fusion model and see how well it applies to low Q**2 regions.

Chapter 3

Apparatus

3.1 Overview

This experiment, as its ancestors E-610 and E-369, centered around its spectrometer, the Chicago Cyclotron Magnet (CCM). In a simultaneous experiment by Fermilab the CCM was made super-conducting. Its virtually trouble-free performance was a tribute to the Fermilab engineers and technicians who redesigned and rebuilt it. The CCM served as the reference point for the muon lab, its center defining (0,0,0). The beam direction gave us positive z, up pointed to positive y; x was to the left of an observer staring in the direction of positve z—a right handed coordinate system.

Upstream of the CCM we put our target and multi-wire proportional chambers (MWPC's) for straight-line tracking. Downstream we had four drift chambers and three muon hodoscopes for measuring the new track directions and for muon identification respectively. Within the CCM we set 5 MWPC's for matching upstream and downstream tracks and for detecting the very curved tracks of low momentum particles.

Behind the last drift chamber and in front of the steel hadron absorber, we assembled an array of lead glass blocks with proportional tubes for photon detection. We also had a Cerencov counter, but it suffered an accident. The overall view of our apparatus is shown in Figure 3-1.

3.2 Beam Line And Upstream Trigger

We used beams of secondary particles channeled to us through a string of tunable magnets which were set to ensure an adequate supply of the proper particle type with the proper momentum. Our first, and longest, run used negative pions at 193 GeV/c. We received a nominal total of 333 billion pions, at a rate of about 3 million per spill. From this we accumulated about 2.2 million events which satisfied our trigger. The second and third runs used protons at 200 and 250 GeV/c respectively, but we had very little data from the second run. We only received about 27.7 billion protons at 200 GeV/c, but about 115 billion at 250 GeV/c. Beam spills came each 12 sec and lasted about 0.7sec. The proton beam was contaminated with about 13% mesons; so before the proton runs we installed 3 low pressure helium Cerencov counters in the beam line to identify the protons. A pion would be half again as likely as a proton to produce a J/psi so the contribution from the unwanted pi-mesons to our J/psi signal would have been

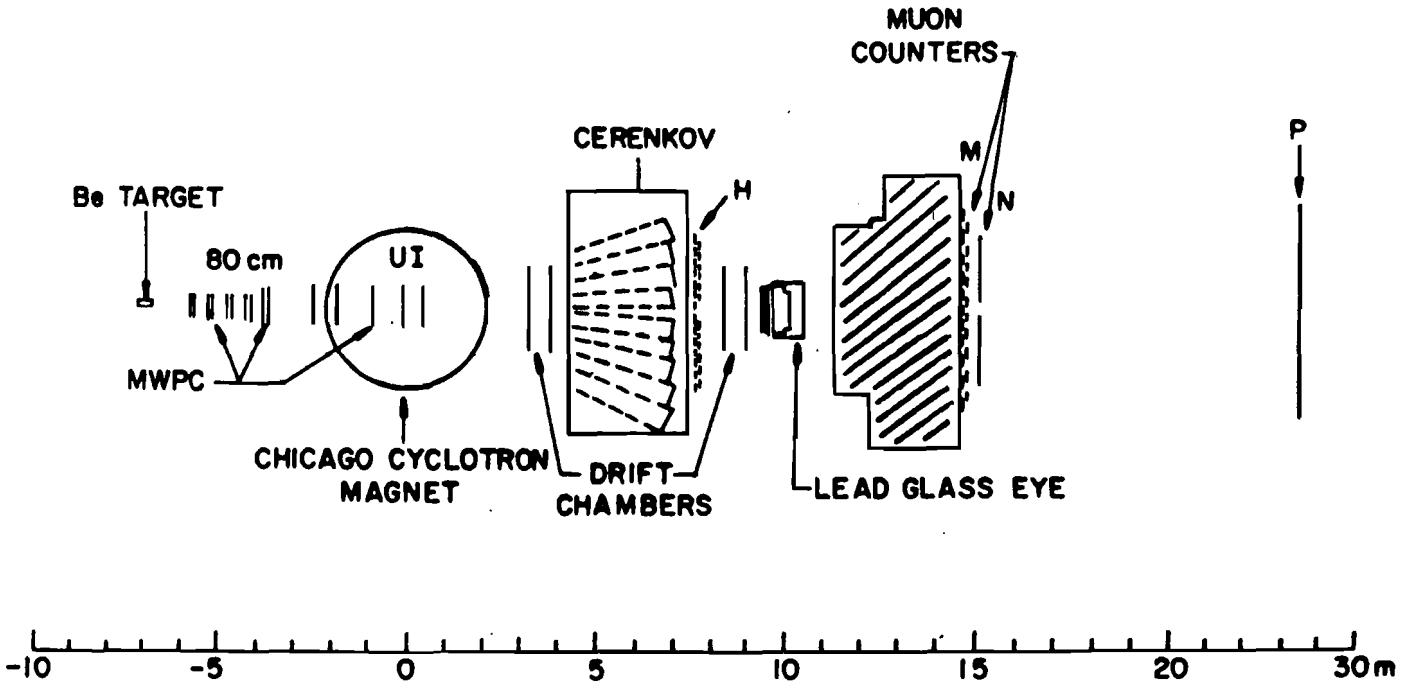

Figure 3-1

E673 Apparatus

significant. Branson et al (Ref 13) found a cross section for J/psi production by pions of 141 +/- 10 nb versus 82 +/- 4 nb for protons.

Figure 3-2 shows the beam line. A complete description of the beam line is beyond the scope of this chapter; let it suffice to say that we found that the beam line required continual attention, and that we appreciate the patience of the Fermilab staff, to whom we frequently appealed for help.

In order to ensure that we looked at one particle at a time, we installed 6 identical thin hodoscopes (8 elements, 0.16cm thick, 2.5cm wide elements, about 0.001 radiation lengths) and and 5 identical MWPC's in the beam line (.212cm wire spacing, about 0.001 radiation lengths), each detector with an active area of 20 x 20cm. An additional MWPC was inserted and hodoscopes 2 through 4 were removed for the electron calibration runs. We required a hit element in each of the 4 hodoscopes in the upstream beam line, and exactly one each in the 2 situated just upstream of the target.

As a further guarantee against halo particles, we installed "veto jaws" — hodoscopes that surrounded the beam, leaving a 10cm square hole — and rejected the event if these jaws were hit. Even so, I have found events with tracks from extraneous particles; but in off-line analysis I used the MWPC information to eliminate these events.

The beam MWPC's and hodoscopes were distributed about one of the main beam bending magnets, called 1E41, in order to determine the beam particle momentum accurately (Figure 3-3). In practice, all 4 beam hodoscopes had to be efficient in order to measure the beam momentum; so in about 11% of events we used the nominal momentum. We were still able to get good beam position information most of the time, which aided substantially in finding the vertex.

After a beam particle traversed the beam line, it entered our laboratory. About 1.5m before it reached the target, it passed through the last two beam MWPC's and the last two beam hodoscopes. Here again, if more than one element in any hodoscope was hit, we vetoed the event, which presumable was contaminated with additional beam particles.

The last parts of our upstream trigger were three thin (.16cm) scintillation counters in the beam path, the smaller ("T0" : 7.6 x 5.1cm) just upstream of the target and the other two ("T1" and "T2" : 12.7 x 12.7cm) just downstream. We required, of course, that the upstream counter record a hit.

The downstream pair were treated somewhat differently. We wanted to trigger on events which produced at least two particles, so the counters' outputs were discriminated. In the following description, T0 is assumed to have had a signal.

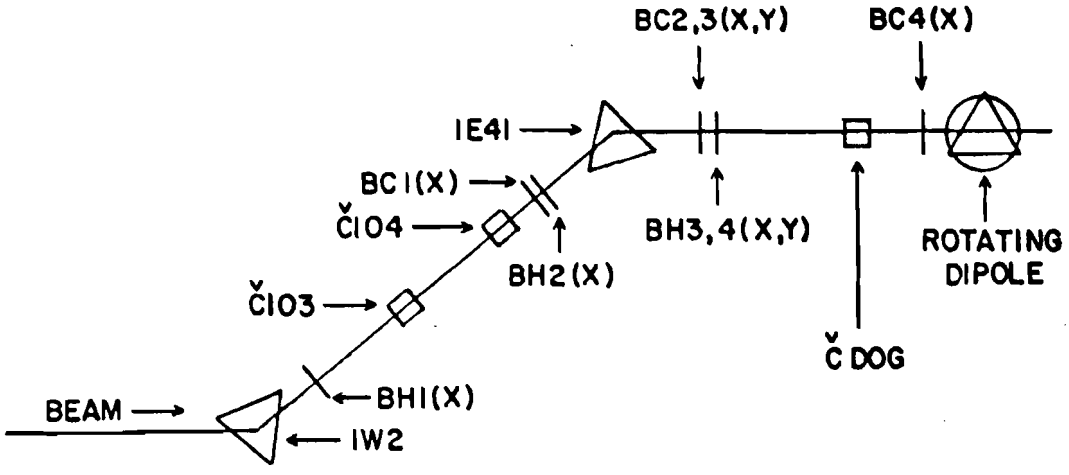

Figure 3-2

E673 Beam Line

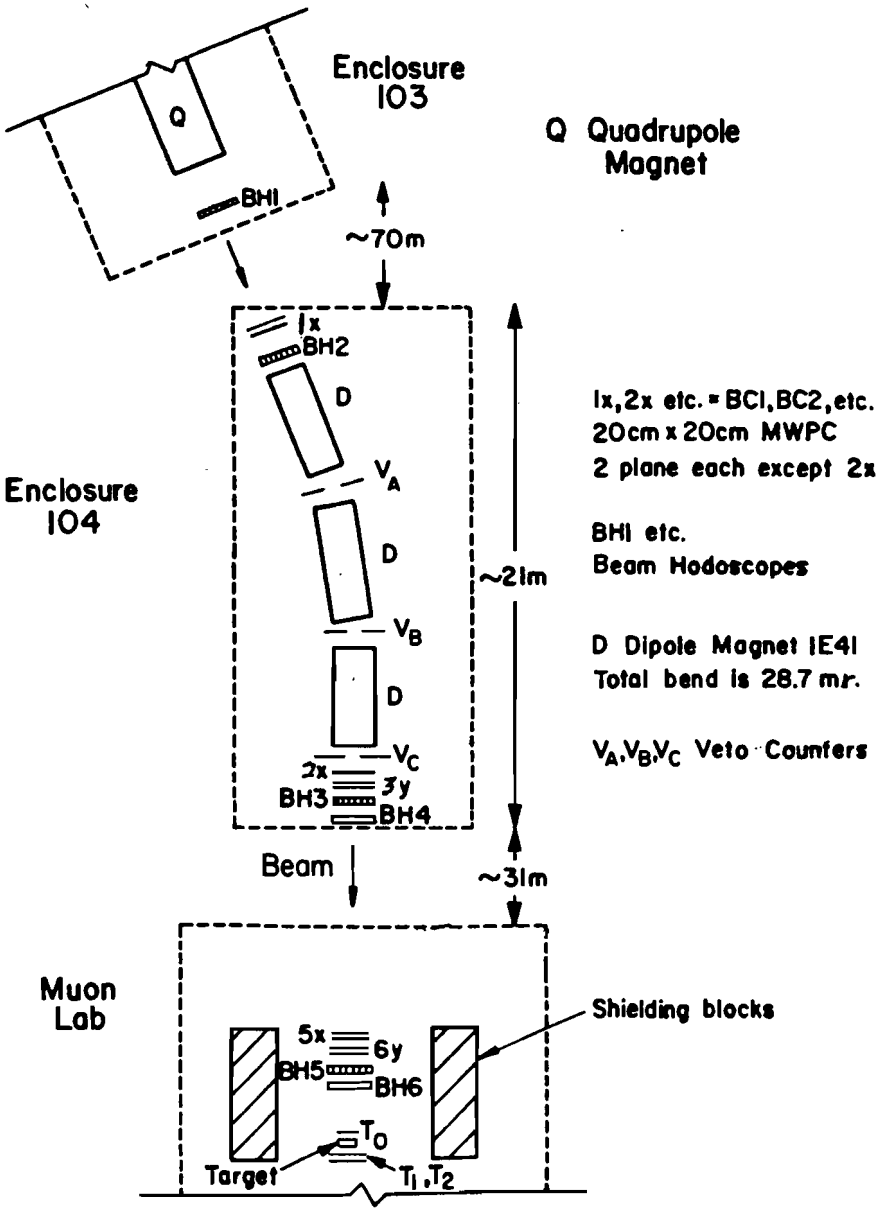

Figure 3-3

Detail of the beam line:
1E41 - the bending magnet

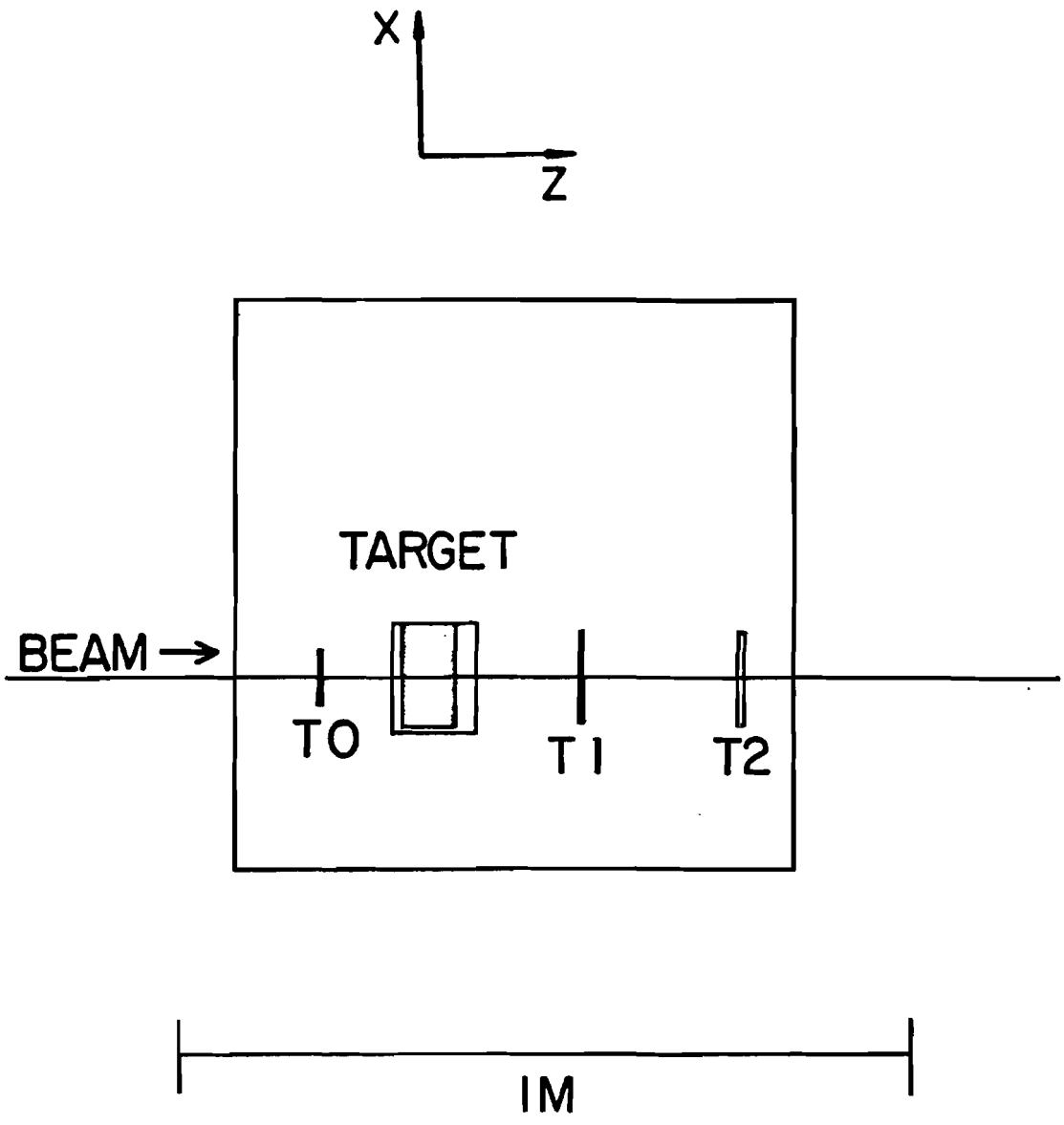

Figure 3-4

The target and target counters

The signals from T1 and T2 were split. For each counter, one part went to a discriminator to detect minimizing ionizing particles (if both T1 and T2 fired here, we had a ULO signal). The other part was attenuated first. If both T1 and T2 fired here, the result was a UHI signal. Plots of the ratio of UHI to ULO versus the attenuation for T1 or T2 were made for test runs with the target in and with the target out. The difference between the two curves (target in - target out) for a given counter's attenuation described the probability that the counters would fire when there was an interaction in the target, as a function of the given attenuation. Each counter's attenuation was set to maximize the probability that both would fire when there was an interation in the target. This process was iterated once to check that the attenuations were correct.

For a target we used a solid prism of beryllium made of 6 1.3cm thick slabs, the whole being Ø.22 radiation lengths thick. This construction prevented any "tracking effects" - particles guided along crystal planes. The target was 13.2cm wide and 7.6cm high, more than enough to cover our expected beam, which was about 4-5cm in diameter. (Figure 3-4) We placed this 690cm upstream of the center of the CCM.

3.3 Downstream Trigger

Our downstream trigger required that there have been a hit in our H (for hadron) hodoscope array in an element 1Øcm away from the beam (Figure 3-5). This was intended to require that there have been at least one fast charged particle moving on a path different from that of beam particles. This array was segmented in x, but signals from both ends of the long hodoscopes were timed with a TDC for y-measurement. Because the drift chambers worked much better than in E61Ø, the H hodoscope information was only used as a final check of track quality in the last stages of track refitting. The y-measurements were never used. Its only other function was to help require that our events be true high energy interactions, not beam particles or "knock-on" (electron scattering) events.

The heart of our downstream trigger was the M and N hodoscope arrays, situated behind about 3.5 meters of steel, about 22m from the target. The M hodoscope, segmented in x, had a hollow bow-tie shape (Figure 3-6) which required low momentum (hence widely deflected) particles to have a large transverse component if they were to be detected. This cut suppressed low mass di-muons, and most low mass meson-decays-in-flight, to enhance the signal in the high mass region. Since we wanted opposite sign muons, we required that there be hits (by definition muons) in diagonally opposing quadrants of the arrays. The N hodoscope provided the y information.

We also installed an array called the P-hodoscope array, located about 8 meters farther downstream. It was intended to help in reconstructing muon tracks, but it covered such a small angle in y (about 2/3 that of N) that its only use was for checking the M and N hodoscopes for efficiency and noisiness during the run.

Since our steel hadron absorber was not infinitely thick, we had a number of pion punch-throughs. In order to reduce their influence, we vetoed the event if more than 1 of the the central 4 M hodoscope elements fired. Our monte carlos predicted that this would cut our J/psi sample by 10%; but cut punch-through background by 40% or more.

The computer had to be ready to read an event before it was possible to read the event, of course. The more wires which were hit in the 80cm chambers, the UI chambers, and the drift chambers, the longer the event took to read in, so our "dead" (busy) time varied noticeably. The average dead time and its variation are not well known.

The final requirement for a trigger was good beam. This would have been a trivial requirement were it not for the fact that in order to accomodate a neutrino experiment, the beam spill was not uniform but was punctuated with extremely high intensity bursts of particles ("pings"). Our beam-measuring devices overloaded and did not reliably record the burst intensity, but the intensity was at least half again as great as for normal spill. These bursts were too intense for our wire chambers to sustain without tripping-off their

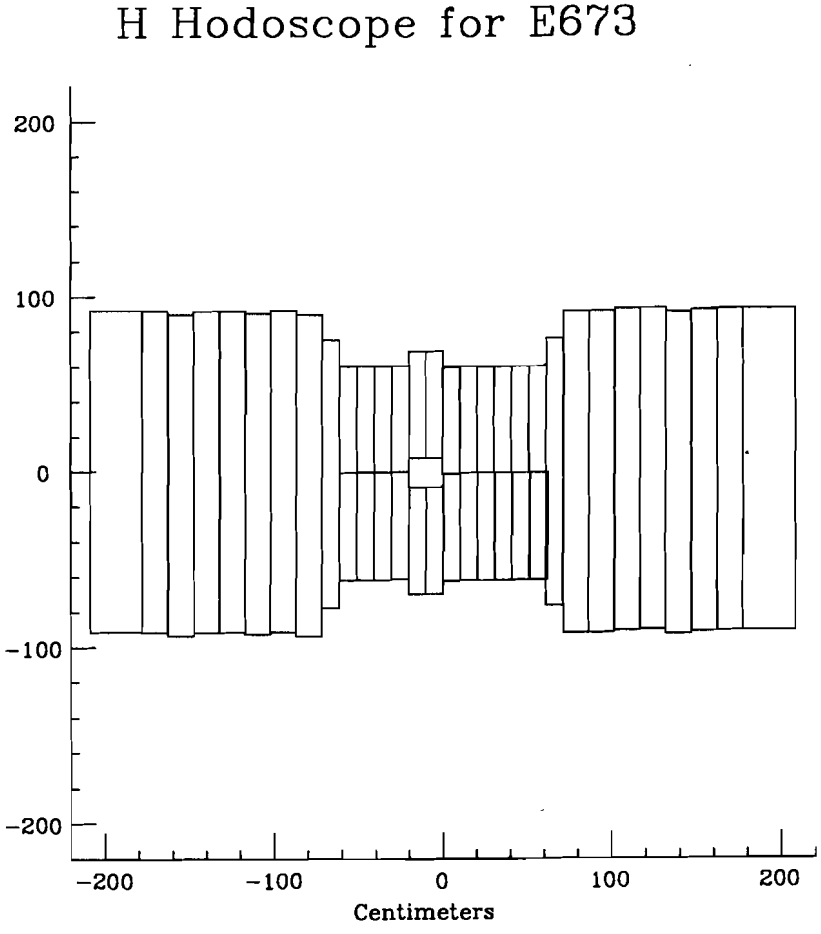

Figure 3-5

The hadron (H) hodoscope

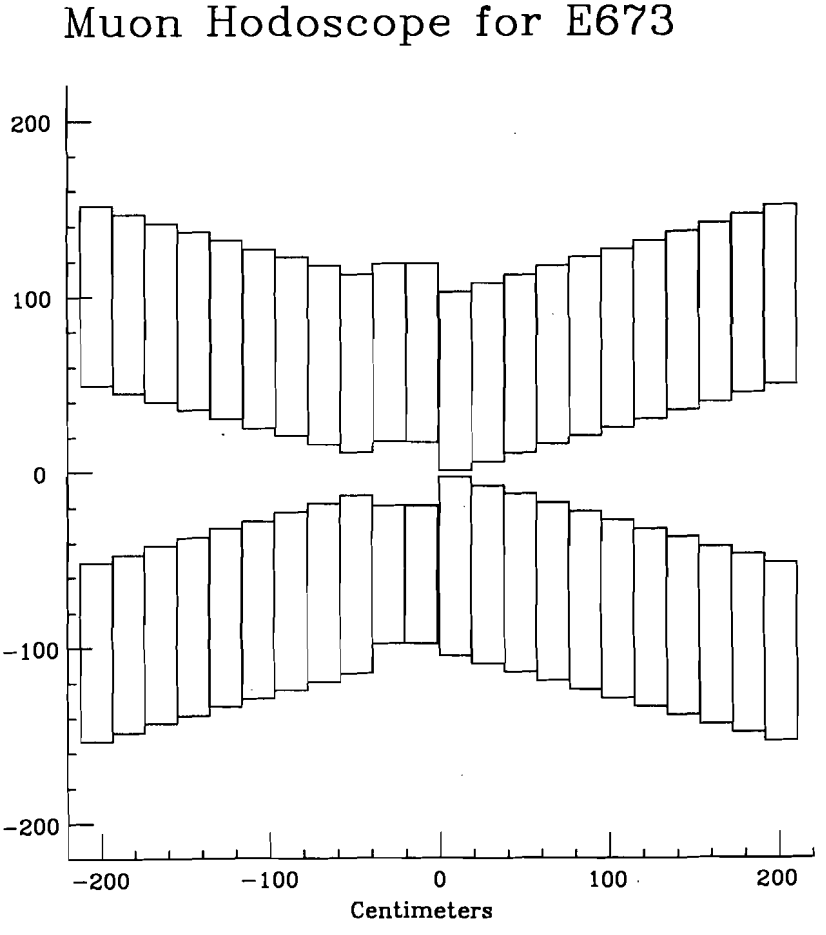

Figure 3-6

The first muon (MUON) hodoscope
x-measuring

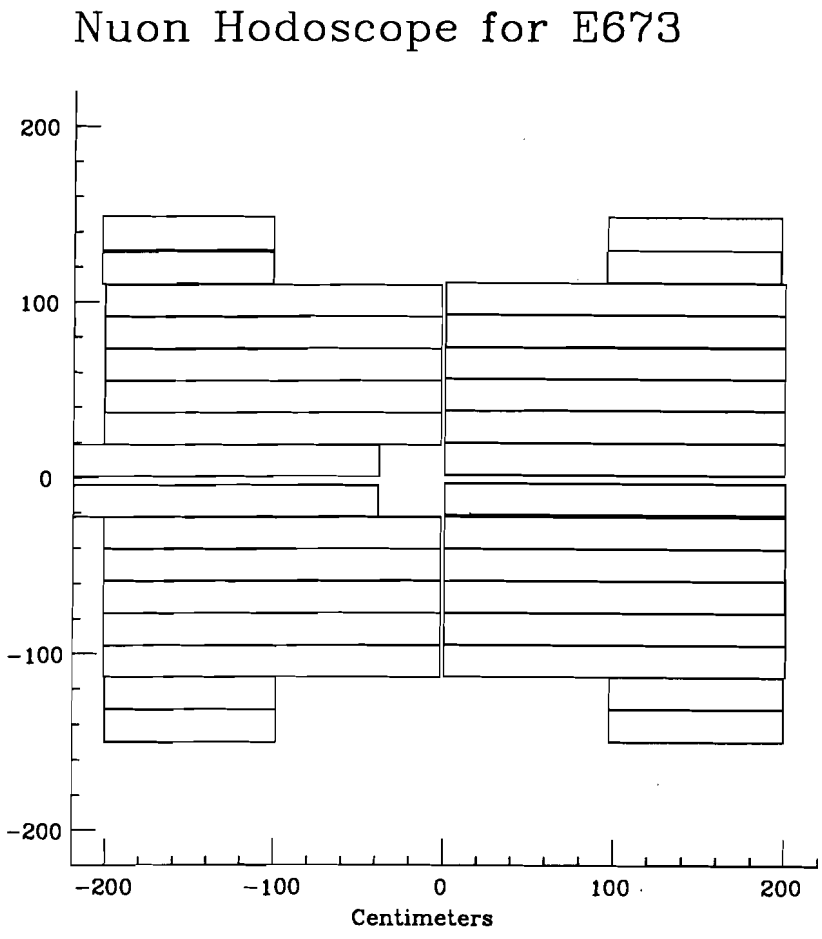

Figure 3-7

The second muon (NUON) hodoscope
y-measuring

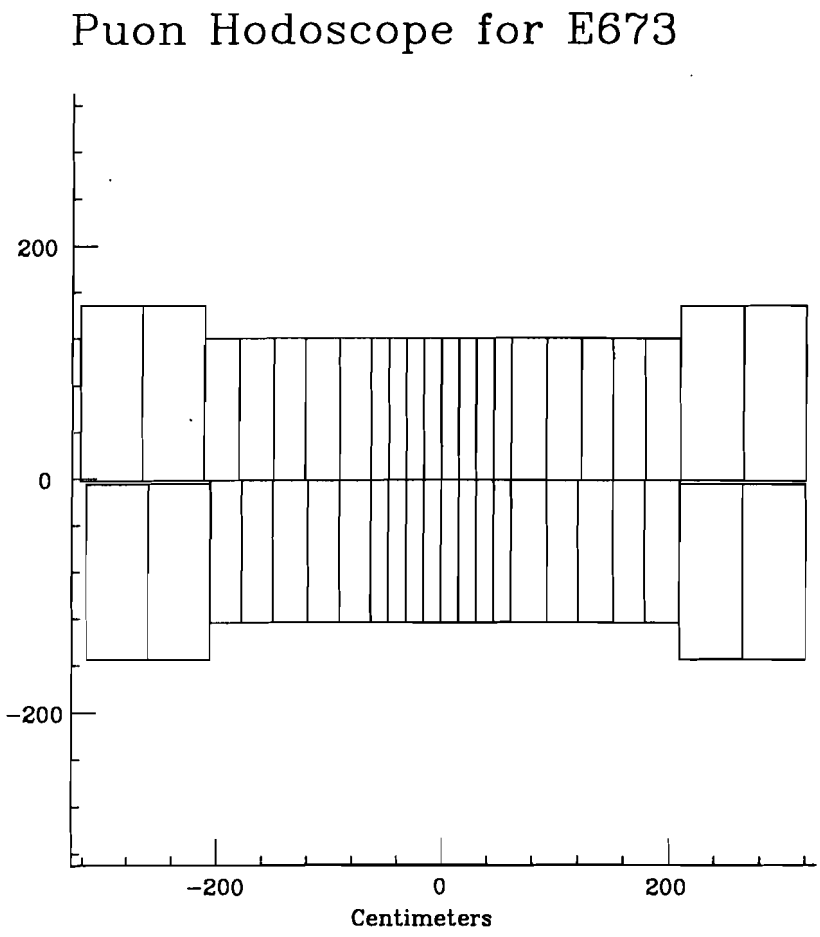

Figure 3-8

The third muon (PUON) hodoscope x-measuring

power supplies, so their voltages were ramped down and data-taking was suppressed during the bursts.

In summary, our trigger required that the beam particle be there and be alone ("clean beam"); that when it entered the lab and approached the target there be one particle; that the target hodoscopes have signals consistent with an interaction (UHI); that the H-hodoscope have an element, not close to the beam line, which fired; and that there be signals from opposite quadrants of our muon hodoscopes M and N (again, not too close to the beam line). The trigger also required that the computer be ready, the event be not less than 20 nanoseconds away from another event (defined as another UHI) to avoid confusion; and the event had to occur when we were expecting good beam. For details, see the thesis of Dr. Patrick Lukens (UI, 1984).

3.4 CCM

Our spectrometer magnet was the celebrated Chicago Cyclotron Magnet. The magnet gap had been widened to 127cm some years before, and just before our experiment began the magnet's coils were replaced with superconducting coils. These proved very reliable; more so, in fact, than the beam line magnets, whose power supplies were subject to coolant-water leaks. The superconducting coils were emersed in liquid helium, which was insulated from the rest of the world by

layers of thin metal, vacuum, and liquid nitrogen.

The CCM used a current of 670 amperes to produce a field of 12.194 kilogauss at the center. This value was chosen by turning on the lead glass phototubes and slowly raising the current in the CCM until the phototube performance began to be degraded, then backing down a few amps. The magnetic field of the CCM can be well approximated by an ideal ("hard-edge") solenoid of radius 252.46cm and magnetic field 12.194 kG. A particle with momentum P (in GeV/c) in the x-z plane followed a path, in the hard-edge approximation, with a radius of curvature (P x 273.5)cm. Dr. Thomas Kirk (Ref 52) devised an empirical fit to the field strength. This is the vertical component. (Figure 3-9)

$$B(r,y) = -12.194\,(kG) \cdot \frac{1 + 2\times10^{-6}\,y^2}{1 + 2.1\times10^{-7}\,e^{r/30}} \qquad , r^2 = x^2 + z^2$$

A charged particle traveling straight down the beam line was given a transverse momentum (momentum "kick") of 1.84 GeV. Such a particle, if it had a momentum less than 5.4 GeV/c, would miss our drift chambers downstream. Particles with less than 0.9 GeV/c momentum were always swept away from our downstream detectors, if they came from the target rather than a decay in flight. See chapter 4 for further discussion of this.

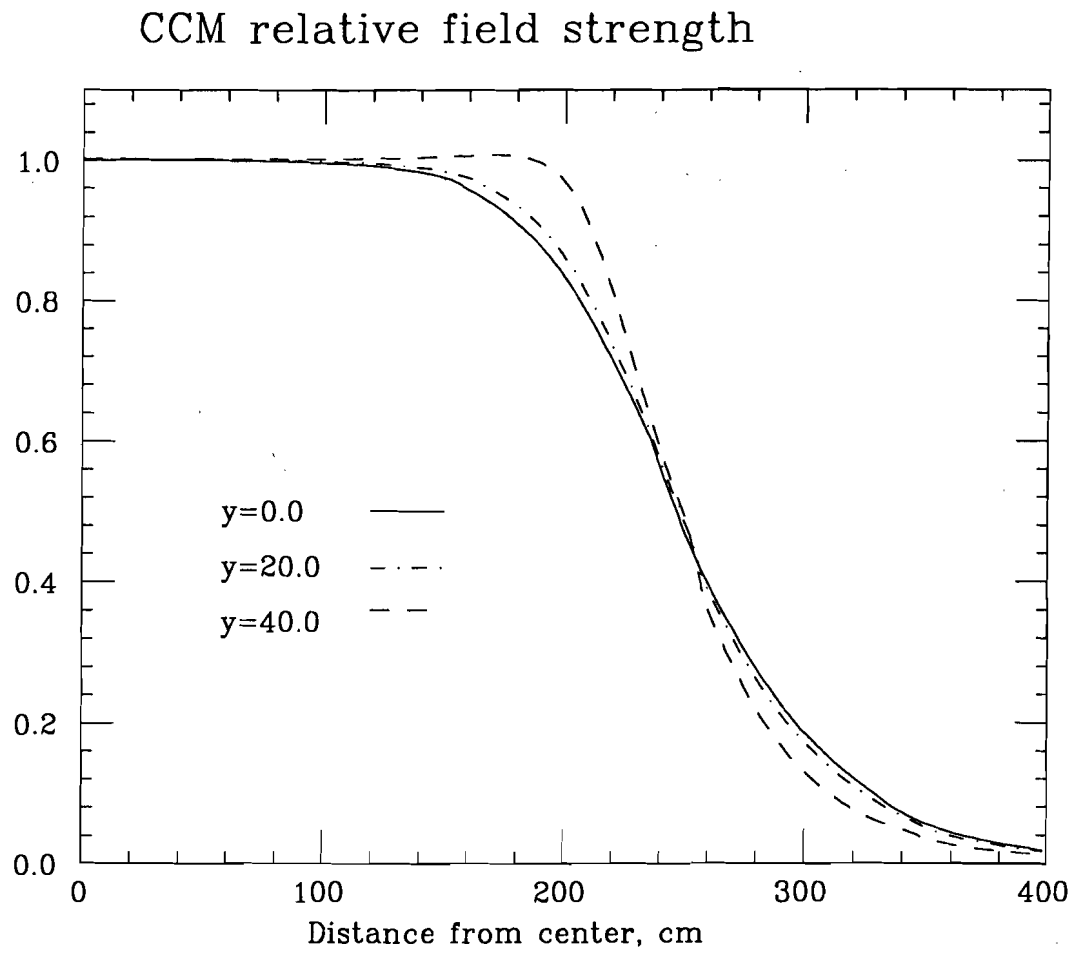

Figure 3-9

The magnetic field within and near the CCM for various elevations.

3.5 Particle Tracking And Identification Devices

Downstream from the target we placed 5 MWPC's 50cm apart each with two planes of wires for measuring y and x. Four of these formed the core of the upstream tracking; the fifth we installed tilted 45 degrees, to assist in track matching. Since the active area on each was 80cm square, we called these the 80cm chambers. Their wire spacing was 0.16cm. Very early in the experiment, the y-measuring plane of the third chamber shorted out, and we ran without it for the rest of the experiment.

On a platform attached to the CCM we set 5 chambers built at the University of Illinois (hence called UI chambers), each containing 3 planes of wires (Figure 3-10). The planes had wire spacings of 0.20cm. One plane measured y. The other two planes, tilted at +11 degrees and -11 degrees with respect to the vertical, were used for x measurements and track matching. For details on the construction of these chambers see the thesis of Dr. Howard Budd (UI, 1983).

The first chamber sat just on the fringes of the magnet, and could be used for track matching for high momentum particles, as these were hardly bent at all at that point. It also could be and sometimes was used in upstream track-finding. We developed several track-finders for tracking particles through the magnet, as they were bent; but none of these are used in this thesis.

Downstream from the magnet, in two pairs 5 meters apart, we placed the drift chambers (Figure 3-11). For E610, these chambers were a source of perpetual frustration; but after we thoroughly cleaned them and built an addition to the gas system which supplied trace amounts of ethanol to suppress sparking, they gave very good service until the last month, when number three failed. These chambers we used to determine what track a particle took after the magnet bent it, and therefore what its momentum must have been. Their design was innovative, using 2 anode wires 0.6cm apart and a charge coupled delay line (a flat bus) (Figure 3-12) between them. The anode wire pairs were 4cm apart, with a total active area of 2.4m x 1.5m and a resolution of 0.05cm in x and 1.5cm in y.

In between the drift chambers sat the room temperature air-filled multi-cell Cerencov counter (Figure 3-13). Its function was to distinguish pions from kaons in the momentum range 6 to 20 GeV/c. The Cerencov light was focused by large mirrors into phototubes seated in the base of Winston cones. Each phototube was equiped with its own electromagnet tuned to counteract the field of the CCM. The Cerencov phototubes were fried in an inadvertant exposure to light while their high voltage supplies were on. It was not used in this analysis. A more detailed description of the Cerencov counter and its use may be found in the theses of Dr. Paul Schoessow (UI, 1983) and Dr. J. Proudfoot (Oxford, 1978).

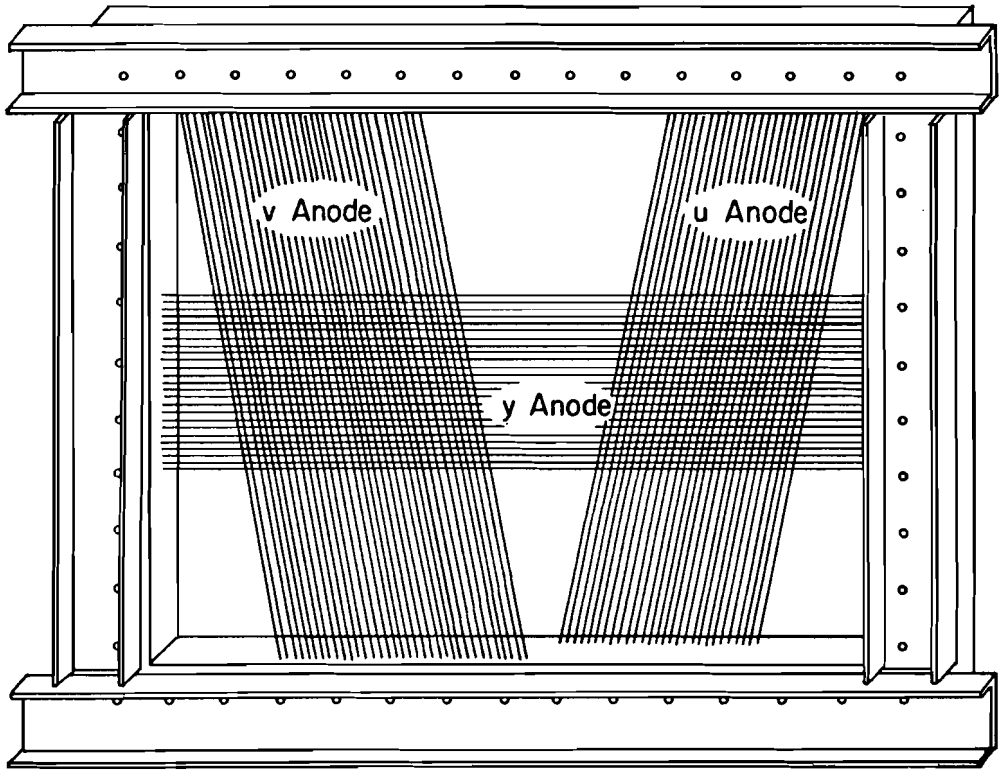

Figure 3-1Ø

MWPC's within the magnet
3 wire planes

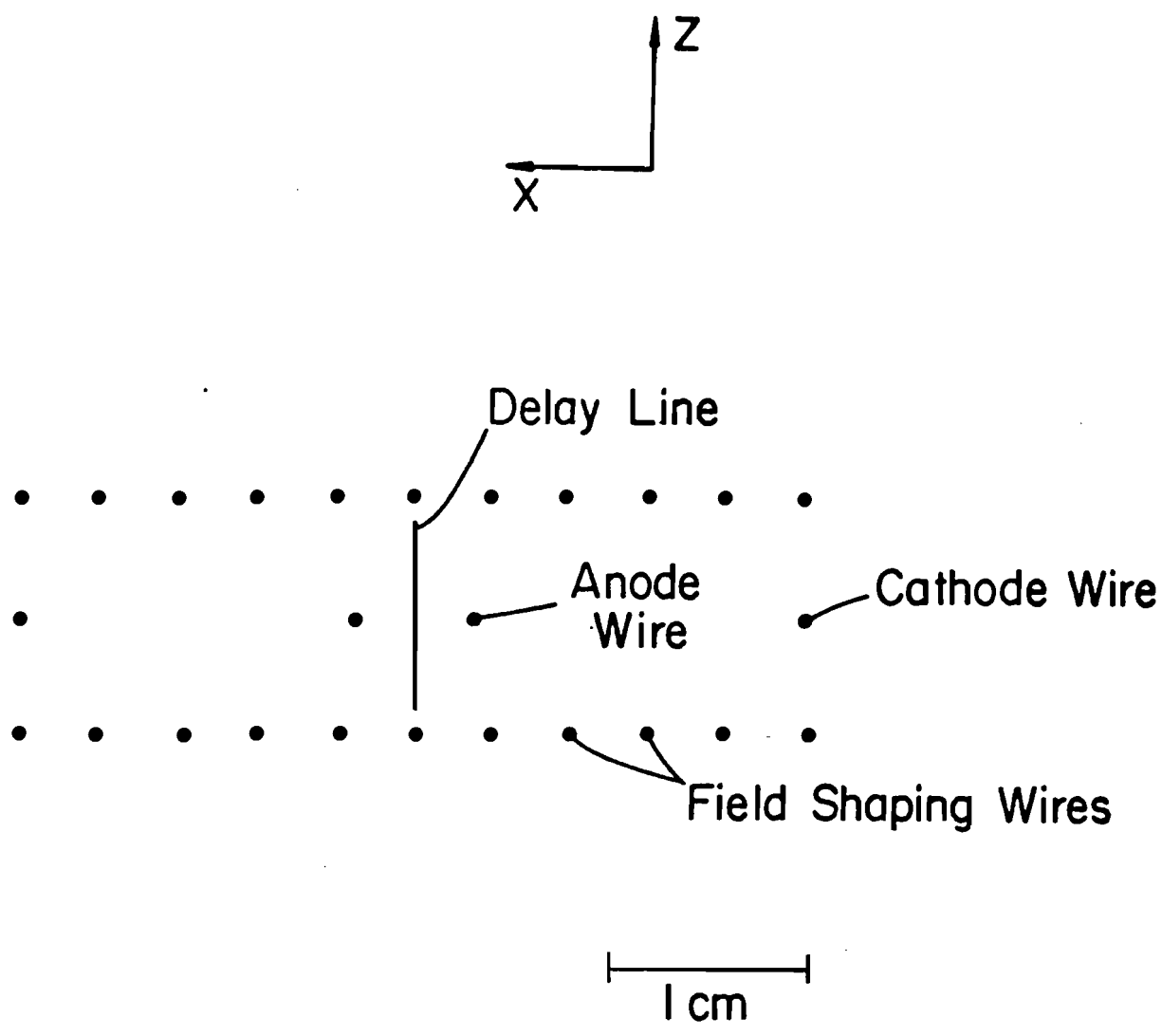

Figure 3-11

Downstream drift chamber cell

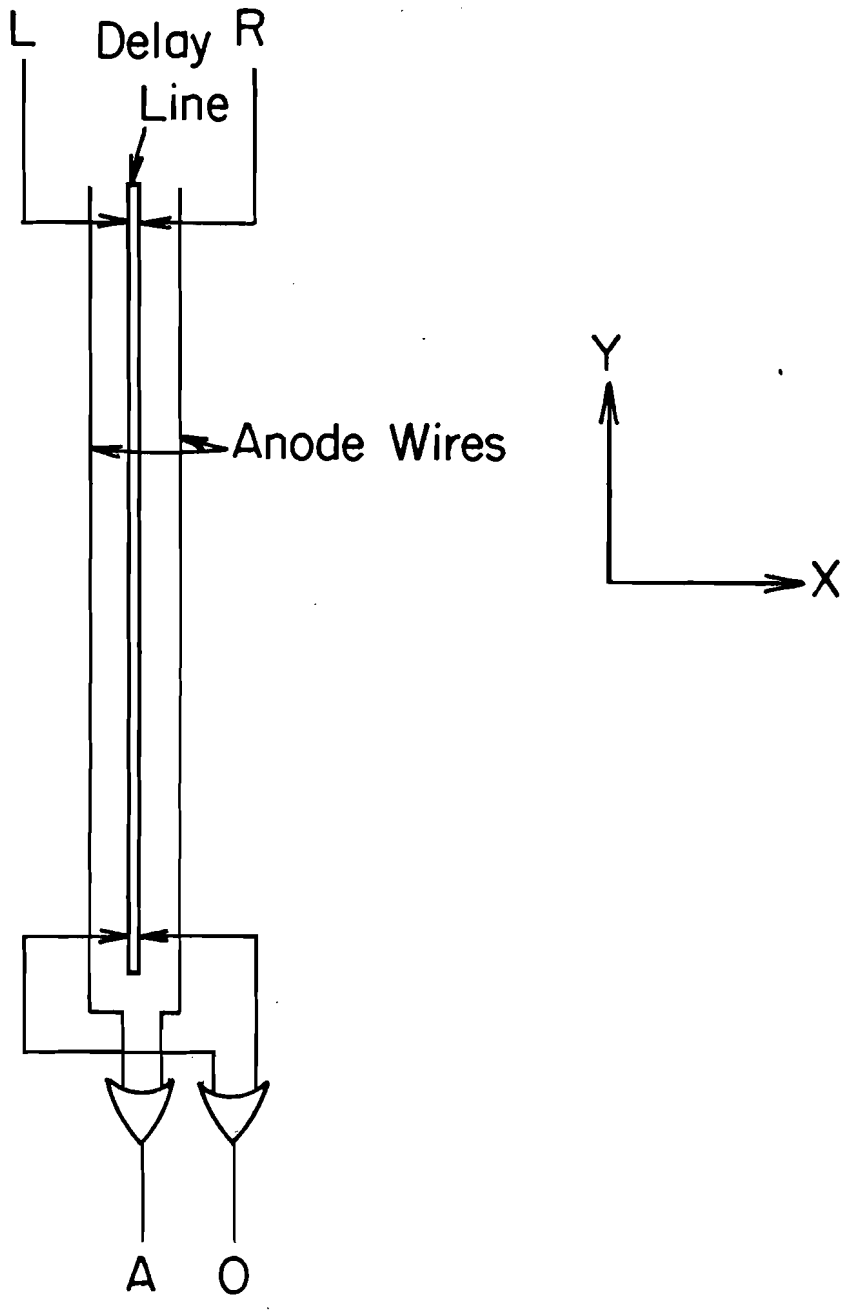

Figure 3-12

Schematic of drift chamber wire read-out

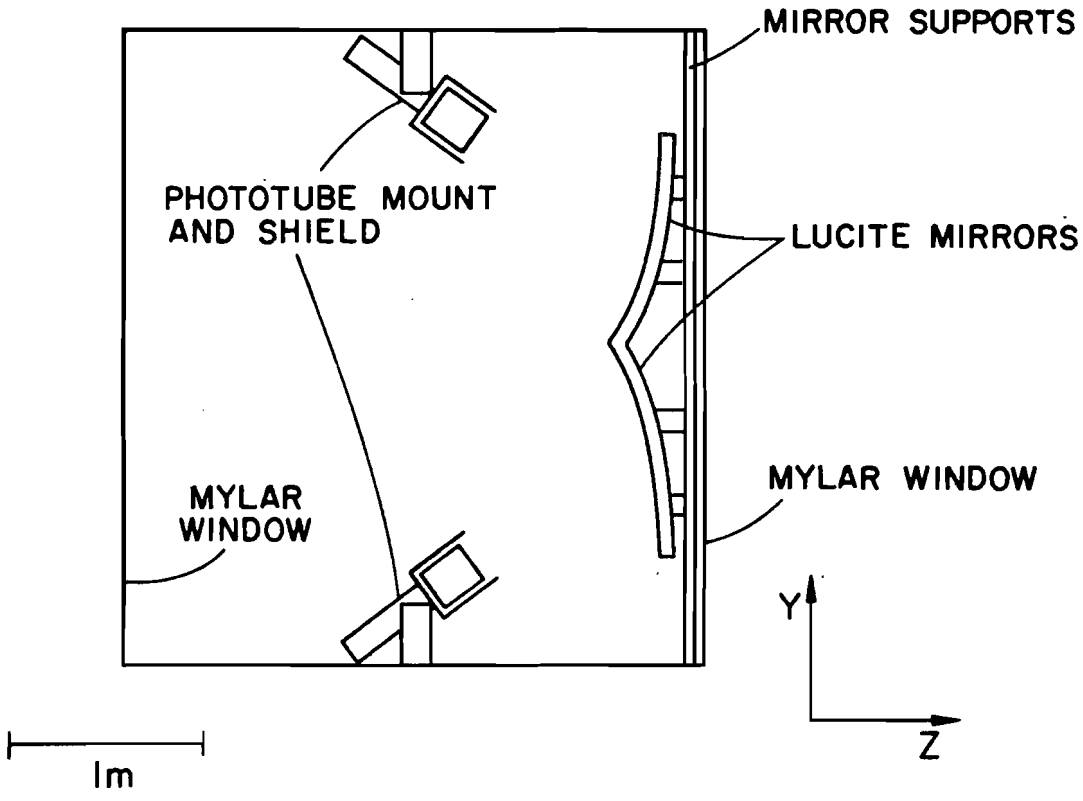

Figure 3-13

Cerencov counter

Behind the second pair of drift chambers we set our lead glass array (Figure 3-14). For full details on its operation, see the theses of Dr. Patrick Lukens (UI, 1984), and Dr. Stephen Hahn (UI, 1983). It consisted of

a passive pre-converter;

iron and lead sheets

(0.73 radiation lengths thick: 0.64cm Fe + 0.37cm Pb);

and an active pre-converter;

the Tufts lead glass

(48 transverse narrow lead glass prisms

2.4 radiation lengths: 58.4 x 6.25 x 6.25 cm);

followed by an array of proportional tubes

(3 planes of tubes, each at 60 degress with respect

to the other planes; 10.2cm deep);

and lastly was backed by the 99 longitudinal lead glass blocks which provided the bulk of the energy determination

(15cm X 15cm X 46cm, 18.33 radiation lengths).

The Tufts lead glass and the p-tubes were used principally to determine the position of an electromagnetic shower, and then the appropriate longitudinal lead glass blocks were used to find the photon energy. The tubes in each plane were staggered to give an effective wire spacing of 0.8cm. See the thesis of Dr. Thomas Graff (UI, 1984) for details of the p-tube construction.

The longitudinal lead glass blocks and the p-tubes recorded a good deal of stale energy, since the response of the phototube was not instantaneous and the physical size of the tubes (1.1cm diameter) meant that a significant time would pass before the old event's ions were swept out. We learned to live with it, thanks in part to the ingenuity of Dr. Lukens in his work on the gamma-finding algorithms.

3.6 Read-in

We used a PDP-11/34 as supplied by Fermilab for collecting and logging data to 6250 bpi tapes. Our data acquisition program was a specially tailored version of MULTI called Muon Lab MULTI, designed to read data from some non-standard sub-systems and to give us better diagnostics and graphics for better and faster on-line check-ups than the standard version. Dennis Ritchie, Terry Lagerlund, Dr. Hahn, and Dr. Lukens helped create and maintain it.

Most parts of our apparatus were easily read in using standard CAMAC devices, but 5 major systems were not. The lead glass signals were collected by a non-standard CAMAC-based ADC system built by LeCroy (model 2280). The internal protocols of this LeCroy system are non-standard, but the crate controller responds to Branch Highway signals in the usual way. The p-tubes I describe below.

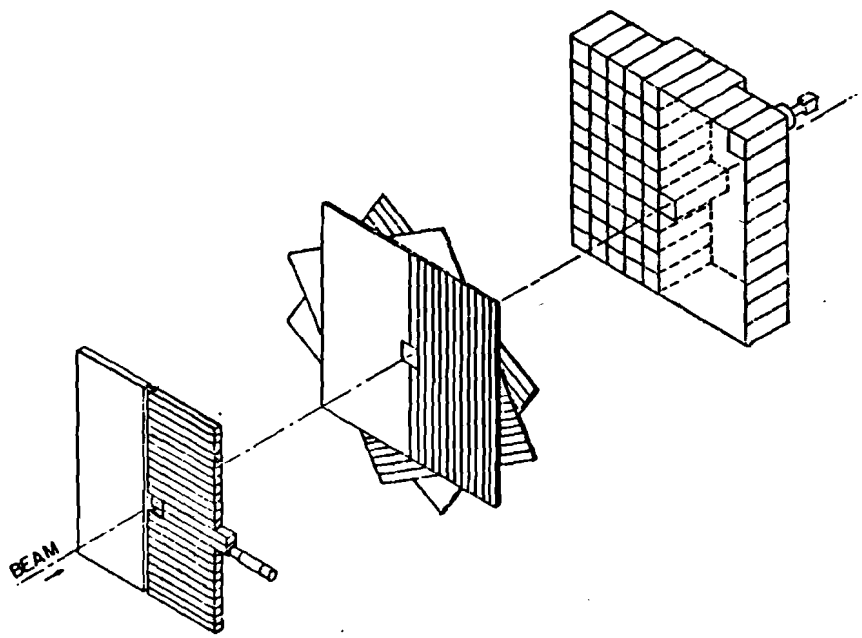

Figure 3-14

Photon calorimeter
a) Passive pre-converter (Pb + Fe)
followed by an active pre-converter
(transverse lead glass)
b) Shower-finding proportional tube array
c) Longitudinal lead glass blocks

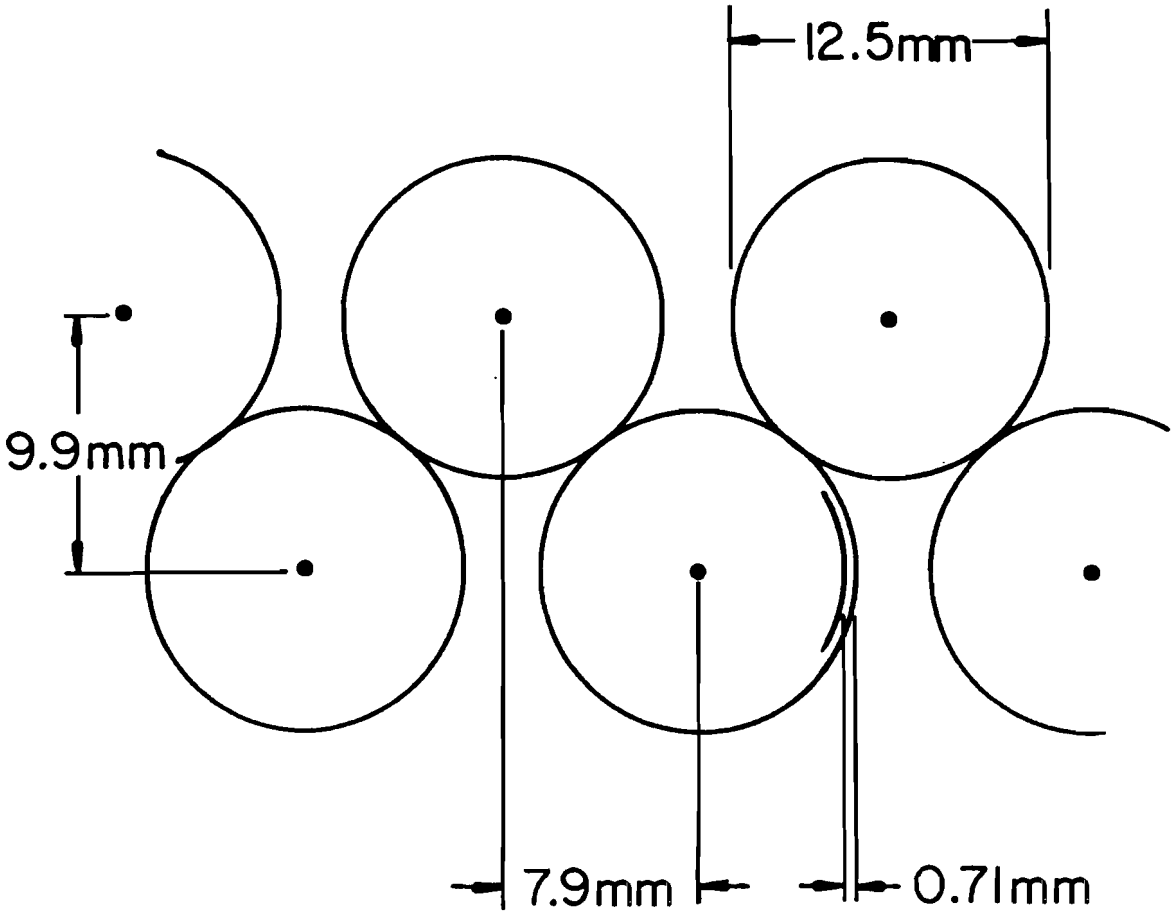

Figure 3-15

Detail of Proportional Tubes

The UI chambers were read by a set of encoders built at the University of Illinois by Robert Downing and James Kohlmier, and the encoded list of hit wires were then passed to a module in a CAMAC crate. Without such encoding, our data buffer would have been too large, as the UI planes contained over 5000 wires. The general outline of the UI-chamber readout system is in Figure 3-16. The amplified and discriminated signals from the wires were read into registers which encoded hits from adjacent wires. The encoders scanned their registers, and encoded all hits as a location of a wire pair and a two-bit flag telling which wires in the pair fired. These were passed to the readout module, which transmitted them to the CAMAC interface module on demand.

The 80cm and the beam chambers' wires were read in using a scanner, built at the University of Chicago by Thomas Nunamaker, which used a shift register recording method. Signals from the amplifiers were serially loaded into a shift register memory, which was then scanned by a CAMAC scanner. For details see Ref 61. The drift chamber wire signals were time-digitized, the delay lines likewise processed, and the results encoded by a Fermilab-built system called MUTES. For details on the MUTES (MUltihit Time Encoder System) see Ref 53, and for details on the UI chamber read-in system see the specifications at the University of Illinois HEP engineering offices.

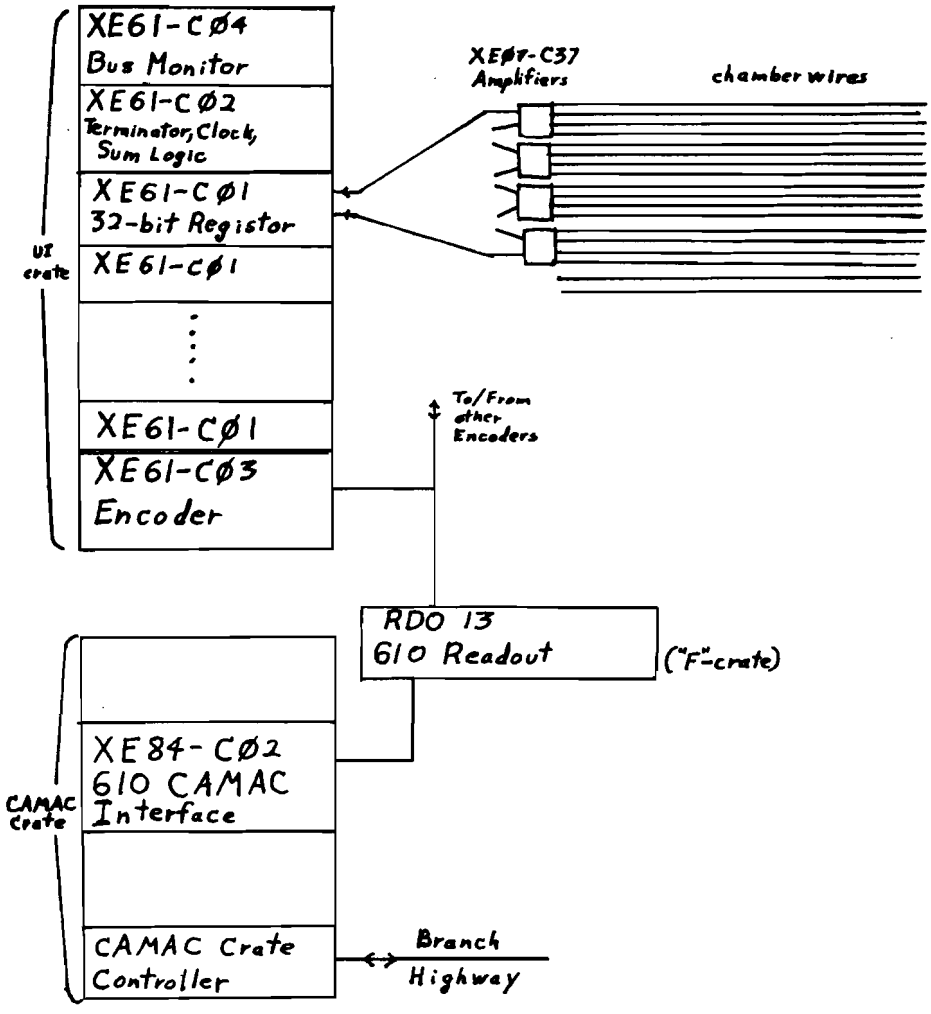

Figure 3-16

General Schematic of the UI-Chamber Read-out System

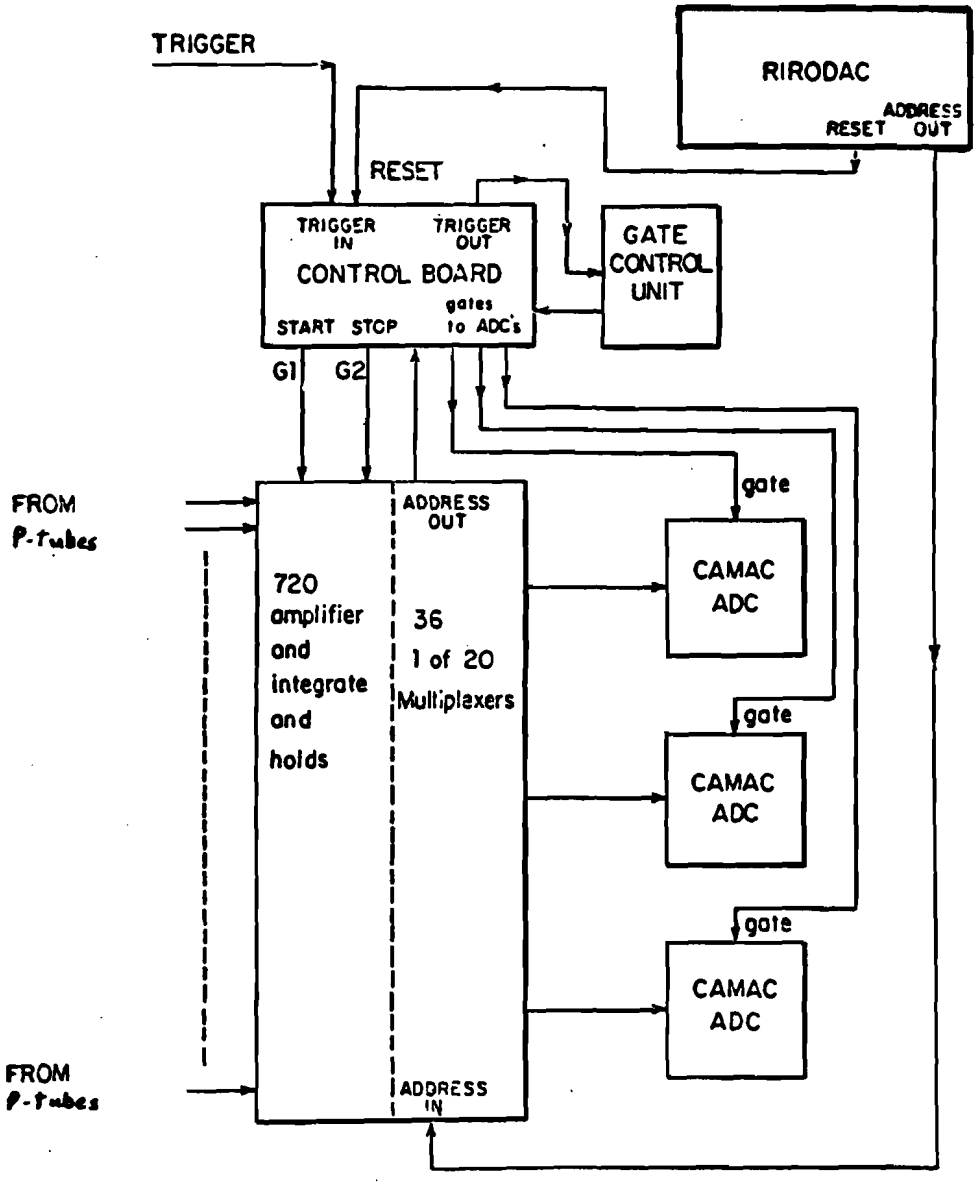

Figure 3-17

General Schematic of the P-tube
Read-out System

3.6.1 P-tube Read-in

The p-tube read-in was ingenious, if not altogether well suited for our experiment. The signal amplifiers and multiplexed read-in electronics were in fact actually designed for a liquid argon calorimeter intended for use in a low interaction rate environment. The p-tube signals were amplified, and the output held on large capacitors. This meant that ADC's measuring peak voltage were more appropriate than the total-charge measuring variety. The amplifiers as originally provided had a fall-off time of several hundred microseconds. These were modified to make the amplified signal decay away in 400 nsec, but a negative overshoot lasted 2 microseconds or so and tended to interfere with later events. A signal could almost be wiped out by a pile-up of negative overshoots from earlier interactions.

A slave computer (LSI-11/23) cleared the ADC's, instructed a "RIRODAC" module to send analog signals to the LARC module (the multiplexer), signaling that it should initialize itself and sample the next set of amplifier outputs. Then the computer waited for the ADC to finish digitizing, read in that set of pulse heights and repeated the process, sampling 30 tubes at a time for 600 tubes (Figure 3-17). This was the slowest single part of our entire read-in, and we needed some complicated custom-made apparatus--a CAMAC DATAWAY data "stealer" with an 18 line bus to a corresponding module in one of the PDP-11/34's CAMAC crates--to make sure we could communicate and record all this in a reasonable time. The cost,

however, was minimal; and to have built our own, as was done with the University of Illinois chamber read-out, would have been quite expensive.

3.6.2 Voltages

Our longitudinal lead glass blocks' phototubes were supplied with power by a LeCroy 4032-A high voltage power supply system, which proved quite reliable. The Tufts phototubes were supplied by NorthEastern power supplies via several distribution boxes which allowed us to easily vary the phototube voltages. The slave computer was also responsible for reading in these voltages, using for the Lecroy system the LeCroy 2132 CAMAC interface and controller; and for the NorthEastern system a Hewlett-Packard Digital Voltage Meter remotedly-controlled and read by a Fermilab-built CAMAC module. The latter system used an electro-mechanical multiplexer to switch the voltmeter from checking one distribution box to checking another. A resistor broke in one of the distribution boxes, providing excessively high voltages to the unfortunate DVM, but otherwise the system proved reliable.

The LeCroy system permitted the computer, in principle, to turn individual power channels off and on, set voltages, and read the voltages. The system would not work at all unless the power supply crates were linked in a particular order. The system generated false

error messages randomly, and after a few hours of good performance it would freeze and cease reading data. Replacing the 2132 module did not help. Fortunately the voltages were stable, and could be read out on the front panels of the power supply crates.

There were four LeCroy power supply crates and two DVM-linked distribution boxes. A crate would be polled once every 4 beam spills (48 seconds) and a distribution box tested every other spill.

Chapter 4

Tracking and Efficiency

4.1 Track Reconstruction

Track-finding was divided into three parts. First, naturally, was upstream (pre-magnet) tracking. This straight-line track-finding took about 60msec per event on a Cyber 175. If the event was found to have a satisfactory number of upstream tracks, downstream (post-magnet) was initiated. This took about 130msec per event. If downstream tracking found and matched at least two tracks of oppositely charged muons, the tracks were written out to a data summary tape (DST). In a later pass the muon tracks were refit by numerically integrating their equations of motion. This took about 1sec per event.

First, of course, the event was checked to make sure there had been no problems with read-in, and that the event had hits in opposite quadrants of the M and N hodoscopes. If the event passed the quick check, the data was fully unpacked into the proper buffers, and then upstream tracking began.

4.1.1 Upstream Tracking

Upstream tracking was divided into three parts, with the x- and y- views treated separately in each section.

First the program tried to locate the beam. Along the beam line we placed three MWPC's and four hodoscopes. (Figure 3-2) One hodoscope stood at the far end of the hall upstream of the magnet called 1E41, and another hodoscope and a MWPC stood next to 1E41 in that hall. These together served to find the beam's position and direction in the x-z plane upstream of 1E41. Just downstream of 1E41 we placed two MWPC's and two hodoscopes to determine as reliably as possible the x and y position of the beam after leaving 1E41. The beam traversed the rest of this hall and entered the Muon Lab proper. Just before the target, another set of two MWPC's and two hodoscopes were used to try to determine the x and y position of the beam. These MWPC's were double planes of 0.21cm wire spacing, so the resolution should have been about 0.03cm. By comparing this beam position with the vertex found at the end of upstream tracking, the resolution is seen to be about 0.1cm.

If all four sections worked, it was possible to determine the beam track upstream and downstream of 1E41 in the x-z plane, and thereby determine if there had been any deflection of the beam from its nominal bend. This additional deflection was used to determine the beam momentum. The two sections downstream of 1E41 then determined the beam position and direction in the y-z plane.

If the beam path was known, its track was projected into the center of the target, and that position was considered to be the preliminary interaction vertex. If the beam path was not known, we used the x and y measurements of the nearest working detector as the vertex position. In lieu of any good information, the default vertex was x=y=0.0.

Now that an interaction vertex was known, the second part of upstream tracking began. The function of this part was to find a better vertex. The first four 80cm chamber x-measuring planes, and the three working 80cm chamber y-measuring planes plus the first UI y-measuring plane were used in this stage in the x and y views respectively. In either view, the aim was to find as many 4-point tracks pointing to the vertex as possible, in order to determine the vertex as accurately as possible.

The track-finder made a list of the sparks in each plane, and kept a list of corresponding flags to tell if the spark had already been used. For 6 different pairs of planes, the program paired unused sparks from one plane with unused sparks from the other, tested whether the resulting track pointed within 5cm of the vertex, and then searched the other two planes to find sparks lying along the track. If these were found, the four points were used to define a track, and each spark flagged as used.

When the tracking finished in one view, the vertex-finding algorithm projected all the tracks to the center of the target, and looked for clusters of points (required to be less than 0.6cm apart). The biggest of these clusters was considered to point to the vertex, which was redefined as the average of the track projections which were members of that cluster.

The tracks found by the previous track-finder were then discarded, and the main track-finder began. The four x-measuring planes in the 80cm chambers were used to find tracks in the x-view, and the three y-measuring planes in the 80cm chambers and the five y-measuring planes the the UI chambers were used to find tracks in the y-view. The CCM's field was sufficiently uniform that vertical focussing effects could be ignored as a good first approximation, and even though four of the UI chambers were in the magnet, the y-projection of a particle's track could be and was treated as a straight line through all the chambers.

In either view, the track-finder began a cycle by drawing a line between the vertex and each spark, and calculating the angle of this line with respect to the beam line. These were stored in a buffer with as many levels as there were wire planes in that view. It then looked at the smallest angle, and compared it with the smallest angle in each of the other levels. If the difference between the smallest angle and the next smallest angle exceeded a critical value, the smallest angle was discarded, and the process was repeated with the

new smallest angle. The critical angle (road) was 1.8mr in the x-view and 2.2mr in the y-view.

If this critical value was not exceeded, the track-finder made a collection of the smallest angles from each level which were within range of this smallest angle. It averaged them, and checked to see if the next-larger angle in any level was nearer the average than the angle actually used. If so, it discarded the one and included the better. If there were enough points included (2 or more in the x-view, 3 {if all in 80cm chambers, else 4} or more in the y-view), a track was formed using the corresponding sparks. This track was tested for goodness of fit as measured by the maximum deviation, and points could dropped out at this stage. If the track was found to be good, with no deviations greater than 0.17cm, and pointing to with 2.7cm of the vertex, its projection to the target center was averaged into the value of the vertex position, and the angles used were discarded. If no good track was found, the smallest angle was discarded.

Notice that the vertex varies in this algorithm. If it was found at the end of the cycle to have varied by more than 0.4cm from its initial value, the cycle was repeated once.

This algorithm was not intended to find neutral V's or any other decays-in-flight, and does not do so well. It is, however, good at finding tracks from the primary vertex, and has been estimated to be about 95% efficient in each view. The resolution varied, but was

about Ø.2mr to Ø.5mr in most places. The limit was 25 tracks in each view. It was my responsibility to adapt the upstream track-finder to our experiment.

4.1.2 Downstream Tracking

If there were two or more tracks in each view from upstream tracking, the downstream tracker was invoked.

Since in the the y-view a track was, to first order, unaffected by the magnet, downstream tracking began in the y-view. For each N-hodoscope (y-measuring) element which showed a hit, a window was established. In order to account for possible vertical focussing, the window was extended 15cm above and below the hodoscope boundaries. If an upstream y-view track pointed within this window a search was undertaken for a corresponding x-view track. This was done by searching in the tilted 8Øcm planes and the tilted planes in the first UI chamber for matches between upstream x-view and y-view tracks. Downstream, each hit M-hodoscope element which overlapped the N-hodoscope element in question was used to define a candidate downstream point. Each matched x,y track pair upstream was tested with each candidate M-hodoscope to define a muon track, about which was defined a fairly wide road. This road was searched for seed sparks in the drift chambers. Each one found was used to define a

muon track. This track was predicted using a "standard track" technique.

The new road appropriate to each new track was searched for confirming hits in all but the first four 80cm chambers, and if 60% or more of all the planes the track passed through had hits, the track was confirmed as a muon. For details see the thesis of Dr. Wei Guo Li (University of Illinois, forthcoming).

4.1.3 Fitting

If two oppositely charged muons were found the event was saved. To find the tracks more accurately it was necessary to fit them. A track could be defined by five parameters: its momentum (signed to indicate charge), its position at the target (x and y), and its direction at the target (dx/dz and dy/dz). It was actually more convenient to use the extrapolated position at the center of the CCM (z=0), but this does not affect anything. We used a routine for swimming (numerically integrating its trajectory using Maxwell's equations) a particle with known parameters through the magnetic field. The predicted track was compared with the sparks from the known track, and the fitter minimized the chi-squared with respect to the track parameters.

The chi-squared was calculated by expanding the predicted value for a track hit in a Taylor series, and keeping only the first two terms. The first term was calculated by swimming a track, but the derivatives of the position with respect to the track parameters were calculated using tables of coefficients appropriate for different momentum ranges. For details see the thesis of Dr. Wei Guo Li.

4.2 Acceptance Considerations

The acceptance may be roughly factored into two parts: a purely geometrical acceptance (does a muon hit a hodoscope or not?) and an acceptance due solely to tracking efficiency. For example, in the y-view, straight-line tracking efficiency upstream of the CCM declines in the central region, from about 96% at moderate y-slopes to about 93% within a few milliradians of the beam line. This decline is due to track confusion. By a fortunate coincidence, the M-hodoscope contained a gap into which most such low y-angle tracks flew; so this decline has little or no effect on our final acceptance.

Since muons may scatter in the hadron absorber, the geometrical acceptance in reality has "fuzzy" boundaries which depend on the muon momentum; and the tracking efficiency is actually a function of how close a track points to a hodoscope boundary. The track-finder permits a 2.5 cm deviation from a hodoscope. Since the average muon

momentum we found was 25 GeV/c (corresponding to a scattering distribution in x or y of 2 cm), I find that simple factoring of acceptance and efficiency is a reasonable approximation, with an error of less than 1%. This error estimate is based on taking the ratio of the average area of a scattering distribution which is outside the effective boundary of a hodoscope to the effective area of the hodoscope. The error rises with decreasing momentum, to about 1% at 6 GeV/c.

The tracking (as opposed to the geometrical) efficiency, was not a strong function of upstream y-slope, as can be seen in Figure 4-1, which shows the total tracking and geometric efficiency. Therefore, for each value of the momentum and upstream x-slope, I calculated an average tracking efficiency over the y-slopes which satisfied the geometric acceptances. By convention, a positive momentum particle had the same charge as the beam particle, and a negative momentum particle had the opposite charge. Given such a signed momentum and an upstream x-slope, I calculated the magnitude of the momentum and the upstream x-slope times the sign of the momentum, and interpolated the efficiency from the efficiencies of the four nearest (momentum,x-slope) points in my table. This technique served to give me the tracking efficiency for any muon which satisfied the geometric acceptances.

This technique provided me with a very flexible tool for studying di-muon acceptances, since I could now generate di-muons with arbitrary Feynman x and perpendicular momentum distributions and arbitrary spins; and could quickly calculate their acceptances without having to implant each muon track in data and track it. The error in monte-carlo acceptances is complicated, but it should be no worse anywhere than 5%.

4.3 Tracking Efficiency

In 100 different events I inserted, one at a time, 182 tracks with the same charge and total momentum, but different upstream x and y-slopes. For muons with momenta 5, 10, 15, 20, 25, 30, 35, 40, 45, and 50 Gev/c, I found the efficiency of the track finding for upstream x-slopes of -0.06 to 0.17, at 0.01 intervals, with upstream y-slopes of -0.05, -0.03, -0.01, 0.0, 0.02, 0.04 and 0.06. In the naive first approximation, a track with some charge and x-slope would be a mirror image of a track with the opposite charge and x-slope. Because different hodoscope elements had different inefficiencies, and because the array was not precisely symmetric about the vertical, this naive approximation did not give precise measurements of the tracking inefficiencies. However, since I looked for envelopes of the efficiency as a function of the slopes and momentum, with the geometry of the hodoscope array suppressing efficiency here and

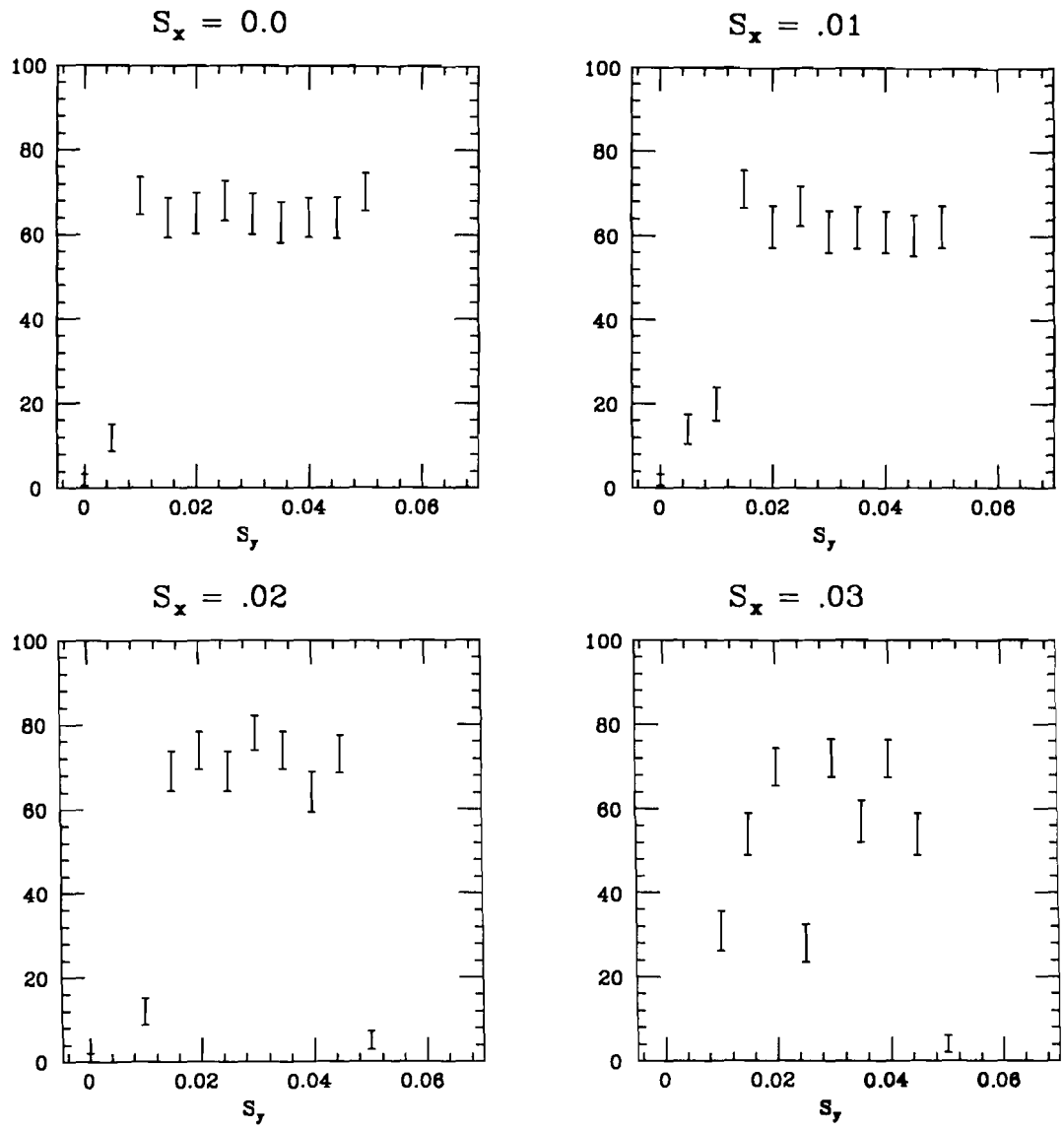

Figure 4-1

Overall tracking efficiency
as a function of y-slope
(includes geometric efficiency, responsible
for the sharp dips seen at low Sx)

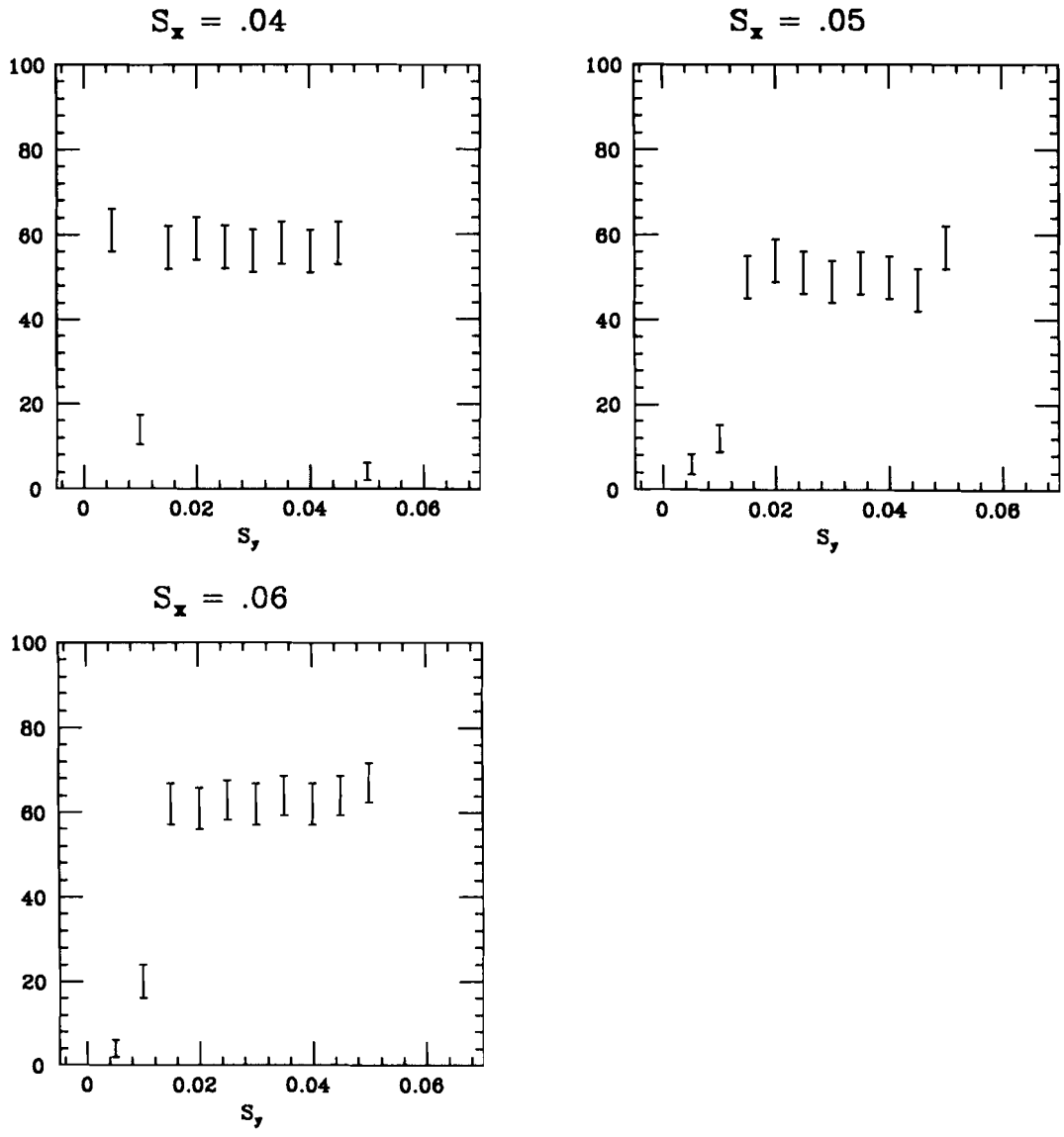

Figure 4-1
(continued)

Overall tracking efficiency
as a function of y-slope
(includes geometry)

there, I do not expect the hodoscope asymmetry to contribute to the error; especially since the the individual elements had similar, though not identical, inefficiencies. Vertical focussing differences only became important near boundaries of the muon hodoscopes.

To test the track finder, I took one of my pre-generated standard tracks and generated a random number (0,1) for each spark on the track. If it exceeded the efficiency for that plane, I omitted the spark, otherwise I inserted it into the list of sparks for that event. Dr. Wei Guo Li determined the overall efficiencies of each chamber (Ref 56), and I use his values in my monte-carlo. A chamber's inefficiency was doubtless position-dependent (lower in the central region), but I ignore this.

Obviously, if the track finder found every spark and calculated the momentum correctly to 5 decimal places, it was successful; while if it divided the sparks among several different tracks, it failed. For intermediate cases, I developed the following test. I assumed that this muon resulted from an omega decay. I further assumed that the other muon was found perfectly. If the track finder found a muon which used at least 60% of the appropriate sparks, had a momentum within 15% of the original, and—when combined with the second muon—had an invariant mass within 50 MeV of the omega, the track finder worked. If not, it failed.

For a particular found track, I histogrammed the quantity delta-m/m for various values of the second momentum. I called the original angle between the two tracks theta, and called the angle between the test track and the found track delta-theta. Since the change in angle between the two tracks enters in the cosine, the angle itself, since it is small, enters as the square. I therefore used the average of the square of the new angle, which is theta squared plus delta-theta squared. The final expression for the error in mass is

$$\left\langle \frac{\delta m}{m} \right\rangle = \left\langle \frac{\delta \eta}{\eta} \right\rangle = \frac{1}{4}\left[\frac{\delta p}{p} + \frac{2p(\Delta\theta)^2}{\eta^2}\right]$$

where eta is the mass divided by the square root of twice the unchanged second momentum. I averaged over the position of the second track, and required delta-m/m to be less than 0.06, which translates to an error in mass of 50 MeV for the omega, or 60 MeV for the phi.

When tracks which miss the hodoscope are omitted, there is little or no dependence on the y-slope. This was verified by picking a momentum and x-slope and slowly varying the y-slope. By omitting tracks which miss the hodoscope and averaging over any y-slope dependence, one creates Table 4-1 (Figure 4-2). There remains a good deal of raggedness due to low statistics.

To determine the tracking efficiency for any given muon track, I took its x-slope, multiplied this by the sign of the momentum (positive for same sign as beam, negative for opposite), took the absolute value of its momentum, and used linear interpolation among the four nearest points in the (x-slope,momentum) efficiency table.

Now I could quickly calculate the tracking efficiency of any given muon track and determine whether it struck the hodoscope array. The monte-carlo program generated 500,000 omegas evenly distributed over (0.0, 1.0) in Feynman-x and (0.0, 1.0 Gev/c) in perpendicular momentum. Each of the resulting 100 regions in (XF, Pperp) space had its own efficiency.

This procedure was used for omegas produced by pions and protons and for phis produced by pions and protons. These efficiencies are summarized in Tables 4-2 and 4-3. Different versions of the acceptance had to be made for pion- and proton-production since for the same Feynman-X, a meson produced by protons (250 GeV/c) had a greater lab momentum than one produced by pions (193 GeV/c).

4.4 Geometric Acceptance

The geometry of the detector excludes some possible particle directions and momenta. For example, in order to pass through the CCM a particle must have an upstream slope in the x-z plane of

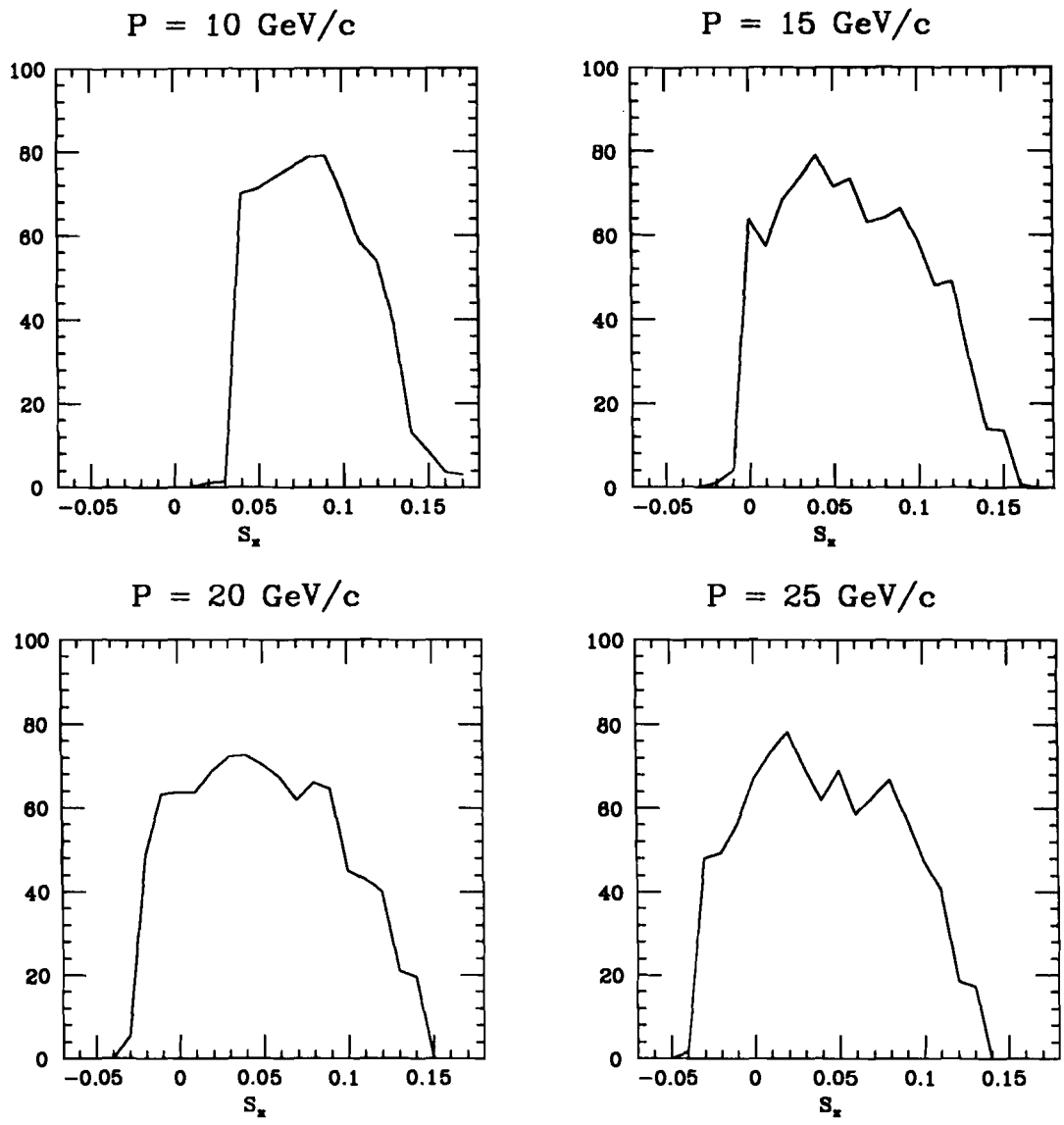

Figure 4-2

Tracking efficiency
as a function of x-slope and momentum

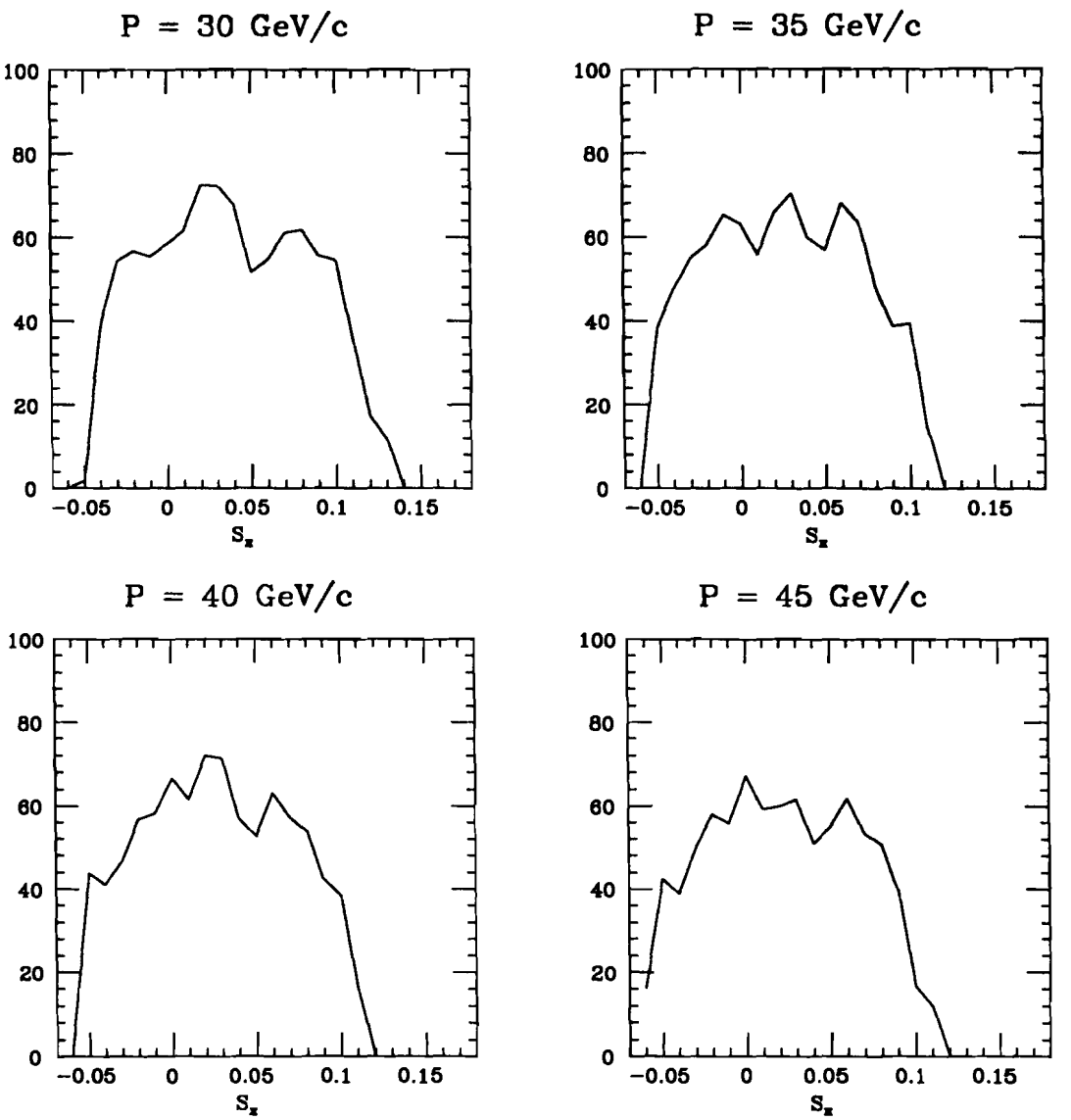

Figure 4-2
(continued)

Tracking efficiency
as a function of x-slope and momentum

Table 4-1
Muon Tracking Efficiencies
Averaged over Sy
(in per-cent)

x-slope Sx	Positive Muon Momentum GeV/c 10	15	20	25	30	35	40	45	50
-0.06	0.0	0.0	0.0	0.0	0.0	1.7	2.0	16.3	18.3
-0.05	0.0	0.0	0.0	0.0	1.8	38.5	43.8	42.4	44.6
-0.04	0.0	0.0	0.0	1.7	38.8	47.8	41.0	39.0	45.8
-0.03	0.0	0.0	5.5	48.0	54.2	55.0	46.8	50.2	47.4
-0.02	0.0	1.0	48.8	49.2	56.6	58.2	56.8	58.0	54.3
-0.01	0.0	4.0	63.4	56.2	55.5	65.3	58.4	55.8	44.6
0.00	0.0	63.8	63.6	67.3	58.3	63.2	66.6	67.2	56.2
0.01	0.0	57.2	63.6	73.3	61.3	55.8	61.5	59.3	54.8
0.02	1.0	68.4	69.0	78.2	72.4	65.7	72.0	60.0	57.0
0.03	1.3	73.4	72.3	69.5	72.3	70.3	71.3	61.7	70.3
0.04	70.0	79.0	72.6	62.0	67.7	60.0	57.0	51.0	54.3
0.05	71.2	71.4	70.3	69.0	51.7	56.8	52.5	55.0	59.5
0.06	73.8	73.2	67.3	58.5	54.5	68.0	63.0	61.8	55.3
0.07	76.2	63.0	61.8	62.8	61.0	63.5	57.3	53.4	36.3
0.08	78.8	64.0	66.0	66.8	61.8	48.0	54.0	50.8	46.8
0.09	79.0	66.2	64.6	57.5	55.6	38.8	42.4	39.7	39.6
0.10	69.2	58.4	45.0	47.2	54.5	39.6	38.4	16.7	14.6
0.11	58.3	48.0	43.0	40.5	36.3	15.2	16.2	12.0	13.8
0.12	54.0	49.0	40.0	18.7	17.2	0.0	0.0	0.0	0.0
0.13	39.0	30.5	21.0	17.3	11.8	0.0	0.0	0.0	0.0
0.14	13.0	14.0	19.5	0.0	0.0	0.0	0.0	0.0	0.0
0.15	8.5	13.7	0.0	0.0	0.0	0.0	0.0	0.0	0.0
0.16	3.7	0.8	0.0	0.0	0.0	0.0	0.0	0.0	0.0
0.17	3.0	0.0	0.0	0.0	0.0	0.0	0.0	0.0	0.0

Table 4-2
Pion-Produced Omega Efficiencies
(In per-cent)

	Pperp (GeV/c)									
XF	0.05	0.15	0.25	0.35	0.45	0.55	0.65	0.75	0.85	0.95
0.05	0.00	0.00	0.00	0.00	0.00	0.00	0.00	0.00	0.00	0.00
0.15	0.48	0.29	0.14	0.12	0.07	0.08	0.06	0.04	0.04	0.05
0.25	3.44	2.07	1.24	0.89	0.62	0.49	0.39	0.37	0.32	0.26
0.35	4.14	2.80	1.64	1.05	0.79	0.58	0.40	0.36	0.29	0.27
0.45	3.73	2.58	1.51	0.94	0.64	0.46	0.39	0.32	0.26	0.22
0.55	2.78	1.96	1.13	0.69	0.50	0.44	0.33	0.30	0.25	0.18
0.65	1.92	1.33	0.88	0.55	0.44	0.36	0.29	0.30	0.21	0.19
0.75	1.00	0.88	0.63	0.47	0.29	0.27	0.26	0.19	0.18	0.18
0.85	0.41	0.38	0.33	0.27	0.21	0.19	0.18	0.14	0.13	0.10
0.95	0.43	0.40	0.31	0.18	0.15	0.18	0.10	0.14	0.10	0.08

Proton-Produced Omega Efficiencies
(in per-cent)

	Pperp (GeV/c)									
XF	0.05	0.15	0.25	0.35	0.45	0.55	0.65	0.75	0.85	0.95
0.05	0.00	0.00	0.00	0.00	0.00	0.00	0.00	0.00	0.00	0.00
0.15	1.65	1.17	0.67	0.39	0.28	0.25	0.21	0.20	0.13	0.11
0.25	4.19	2.86	1.58	1.04	0.80	0.66	0.44	0.39	0.35	0.25
0.35	3.74	2.56	1.51	1.04	0.71	0.53	0.48	0.36	0.26	0.25
0.45	2.47	1.87	1.14	0.75	0.51	0.41	0.34	0.29	0.21	0.24
0.55	1.31	1.01	0.77	0.47	0.36	0.27	0.26	0.22	0.19	0.15
0.65	0.51	0.44	0.35	0.24	0.19	0.21	0.16	0.16	0.12	0.11
0.75	0.49	0.29	0.26	0.23	0.14	0.13	0.09	0.07	0.10	0.09
0.85	0.42	0.41	0.27	0.16	0.06	0.11	0.07	0.06	0.01	0.02
0.95	0.29	0.24	0.17	0.11	0.06	0.03	0.03	0.02	0.01	0.01

Table 4-3
Pion-Produced Phi Efficiencies
(In per-cent)

	Pperp (GeV/c)									
XF	0.05	0.15	0.25	0.35	0.45	0.55	0.65	0.75	0.85	0.95
0.05	0.00	0.00	0.00	0.00	0.00	0.00	0.00	0.00	0.00	0.00
0.15	0.84	0.85	0.71	0.55	0.43	0.37	0.33	0.30	0.17	0.24
0.25	6.25	5.71	4.84	3.70	2.74	2.05	1.68	1.40	1.15	1.08
0.35	9.00	8.22	6.37	5.33	3.97	3.07	2.33	1.87	1.60	1.33
0.45	8.25	7.25	6.04	5.04	3.70	2.95	2.15	1.74	1.52	1.35
0.55	6.41	5.46	4.89	3.77	3.00	2.34	2.00	1.68	1.43	1.11
0.65	4.70	4.47	3.73	3.04	2.42	2.03	1.58	1.36	1.13	1.03
0.75	3.63	3.39	2.92	2.48	2.03	1.53	1.28	1.07	1.00	0.80
0.85	3.05	2.69	2.33	1.97	1.52	1.17	0.99	0.84	0.75	0.61
0.95	2.36	2.33	1.87	1.45	1.14	0.93	0.86	0.65	0.64	0.55

Proton-Produced Phi Efficiencies
(in per-cent)

	Pperp (GeV/c)									
XF	0.05	0.15	0.25	0.35	0.45	0.55	0.65	0.75	0.85	0.95
0.05	0.01	0.00	0.01	0.01	0.00	0.01	0.01	0.02	0.02	0.00
0.15	3.23	2.98	2.55	1.98	1.44	1.21	0.93	0.80	0.71	0.55
0.25	8.44	7.57	6.38	4.97	4.23	2.96	2.27	1.94	1.53	1.44
0.35	7.78	7.50	6.10	4.74	3.76	2.82	2.16	1.85	1.41	1.23
0.45	5.97	5.12	4.37	3.65	2.70	2.30	1.99	1.53	1.28	1.10
0.55	4.15	3.79	3.18	2.71	2.10	1.63	1.44	1.19	1.11	0.83
0.65	2.97	2.94	2.36	1.75	1.50	1.24	0.99	0.92	0.72	0.67
0.75	2.50	2.12	1.76	1.26	1.07	0.91	0.84	0.61	0.65	0.53
0.85	1.93	1.49	1.50	1.20	0.89	0.67	0.57	0.44	0.44	0.32
0.95	1.58	1.49	1.42	0.99	0.82	0.54	0.47	0.27	0.19	0.21

less than 0.365. Any particle with abs(Dx/Dz) > 0.365 will miss the CCM, and consequently we will never know its momentum.

The requirement that the N hodoscope be hit is a strong one. It implies that the particle remained within y bounds on every wire chamber. Only if it goes out of bounds in x will it fail to pass through the active area of every chamber. It constrains the upstream y-slope of a muon to be less than 0.0678, neglecting vertical focussing effects.

The CCM swept away any charged particles with momentum less than 0.92 GeV/c, provided they were created upstream of the magnet. In addition, the N hodoscope requirement set a lower limit of 1.98 GeV/c on the momentum of muons. When I added the tracking requirement that the upstream track emanate from the target and pass through at least two of the 80 cm chambers (requires x-slope < 0.224), the minimum momentum a detectable muon could have had was 2.87 GeV/c (Figure 4-3).

In all of the above, I have assumed that the particle in question came from an interaction in the target, and not a decay in flight. This may seem odd, as the majority of our triggers came from meson decays in flight, not from muons produced in the target. The track-finder worked by matching upstream tracks to downstream hits, and if a meson decayed into a muon with the muon track widely different from the parent meson, the track-finder was unable to match the hits, and consequently failed to find the track. Thus we find

mostly decays in the forward direction, with the muon track nearly the same as that of the parent meson, and my assumption is a good approximation.

The difference in track between the parent and daughter is not great for a di-pion decaying to two muons. (Figure 4-4). For a 1.0 GeV/c**2 mass meson of zero width which decays into two pions, which subsequently decay into two muons, the resulting mass distribution is a narrow peak at 0.96 GeV/c**2 with a full width at half maximum of about 20 MeV/c**2. A 1.0 GeV/c**2 "di-pion" has about a 1.43 E-6 chance of decaying to two muons and being accepted. For a 1.2 GeV/c**2 meson decaying to two kaons which subsequently decay to muons, the peak is at 0.68 GeV/c**2, and is about 100 MeV wide. A 1.2 GeV/c**2 "di-kaon" has about a 3.05 E-5 chance of decaying to two muons and being accepted. The meson was assumed to be distributed in Xf and Pperp according to Branson et al's fits (Ref 13).

The J/psi can decay to two pions as well as two muons, with branching ratios of 0.011 and 0.074 respectively; but this would amount to only 0.06% of our sample, or about 1 event, so the possibility that J/psis arise from pion decays in flight may be discounted.

We see peaks which center on or about the omega, phi, and J/psi masses, with widths of 31.3 +/- 2.0, 24.3 +/- 3.2, and 58.9 +/- 2.5 Mev/c**2 respectively. Notice that our mass resolution becomes worse

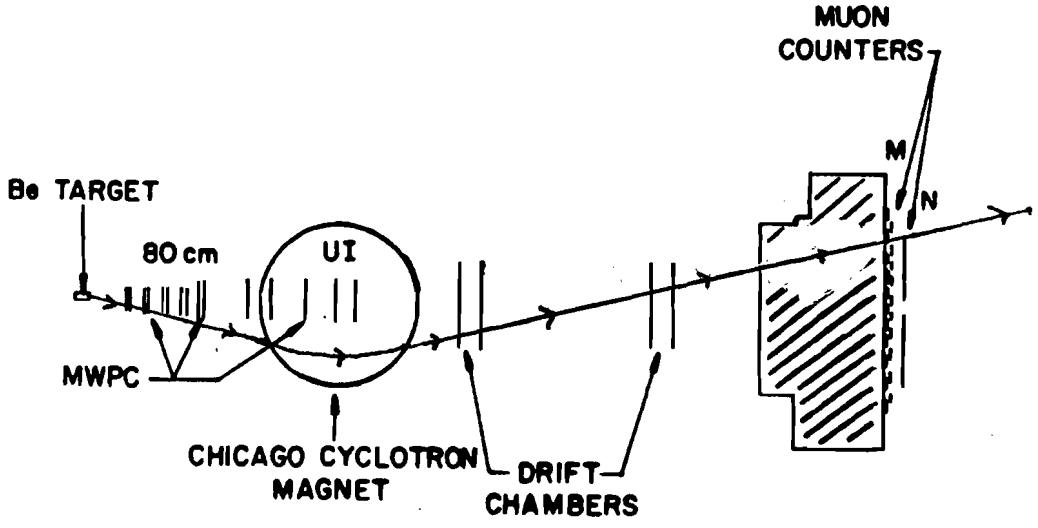

Figure 4-3

Minimum muon momentum track

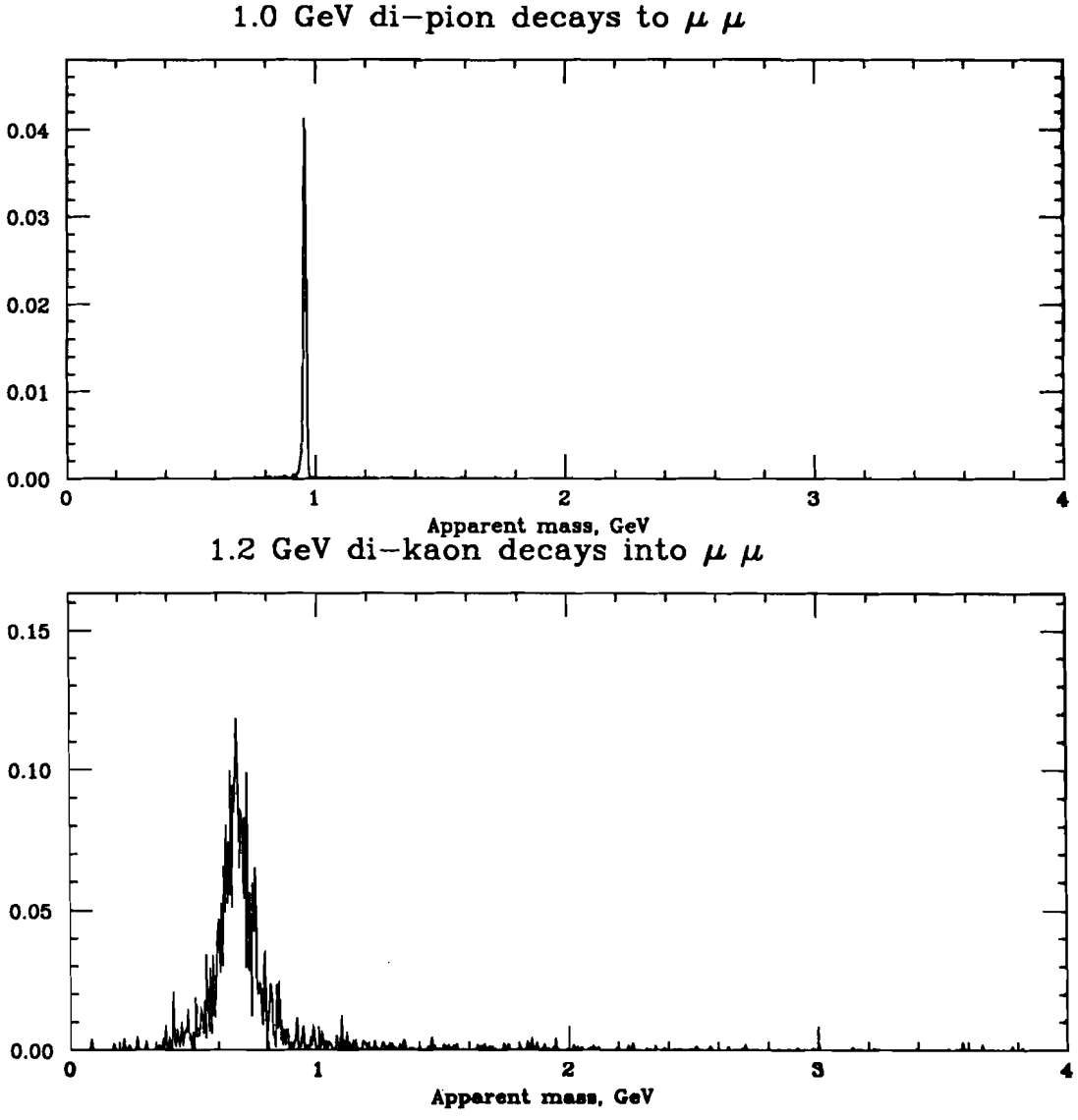

Figure 4-4

Apparent mass of

a) 1.0 GeV di-pion decaying to two muons
b) 1.2 GeV di-kaon decaying to two muons

at higher masses, as would be expected, but the relative resolution improves, going from about .04 to about .02. The resolution is about 20 MeV/c**2 near the omega and phi masses, and about 60 MeV/c**2 near the J/psi. For a meson with mass near the omega which decayed into two pions, which decayed to two muons, the resolution would be of the order of 35 MeV/c**2 plus the natural width of the meson.

I may assert that these three peaks represent true di-muon decays of the above-mentioned mesons. Unfortunately, the rho is naturally so wide that I cannot exclude the possibility that the rho peak contains nothing but di-pion decays: on the contrary, I estimate that we detect from between 2.5 to 3.0 times as many rhos as omegas. Previous work (Ref 51, 12, 1) suggest that rhos and omegas are produced in the ratio 1:1 in hadronic interactions, so I conclude that the rho peak contains the cascaded decay rho to two pions, which subsequently decay to two muons (and two neutrinos). There will also probably be a substantial fraction of pion punch-through as well.

Chapter 5

Method of Analysis

5.1 Di-muon Analysis

I required that the di-muon's perpendicular momentum (Pperp) be less than 1.Ø GeV/c. This cut about 1Ø% of the events. I began by producing mass plots with different Feynman-X (XF) intervals, in particular, Ø.Ø to Ø.1, Ø.1 to Ø.2, and so on, to Ø.9 to 1.Ø. I sometimes used intervals from Ø.Ø to Ø.2 etc., when the signal was hard to see. Our acceptance for omega mesons with negative XF was negligible. In fact, as you may see from Figure 5-1, our acceptance became too small to measure for XF less than about Ø.Ø5 . A set of such mass plots for the omega region (using pion data) is shown in Figures 5-2 though 5-3, in order of increasing XF. Figures 5-4 through 5-6 are mass plots of different intervals of perpendicular momentum. Similar figures for the phi are in Appendix B.

There may be seen clear omega signals in many of these, and less distinct signals in most of the rest. It is possible to convince yourself that there is a rho meson bump spreading out below the omega as well; but this is so hard to see that I cannot study it, and instead treat it as a background.

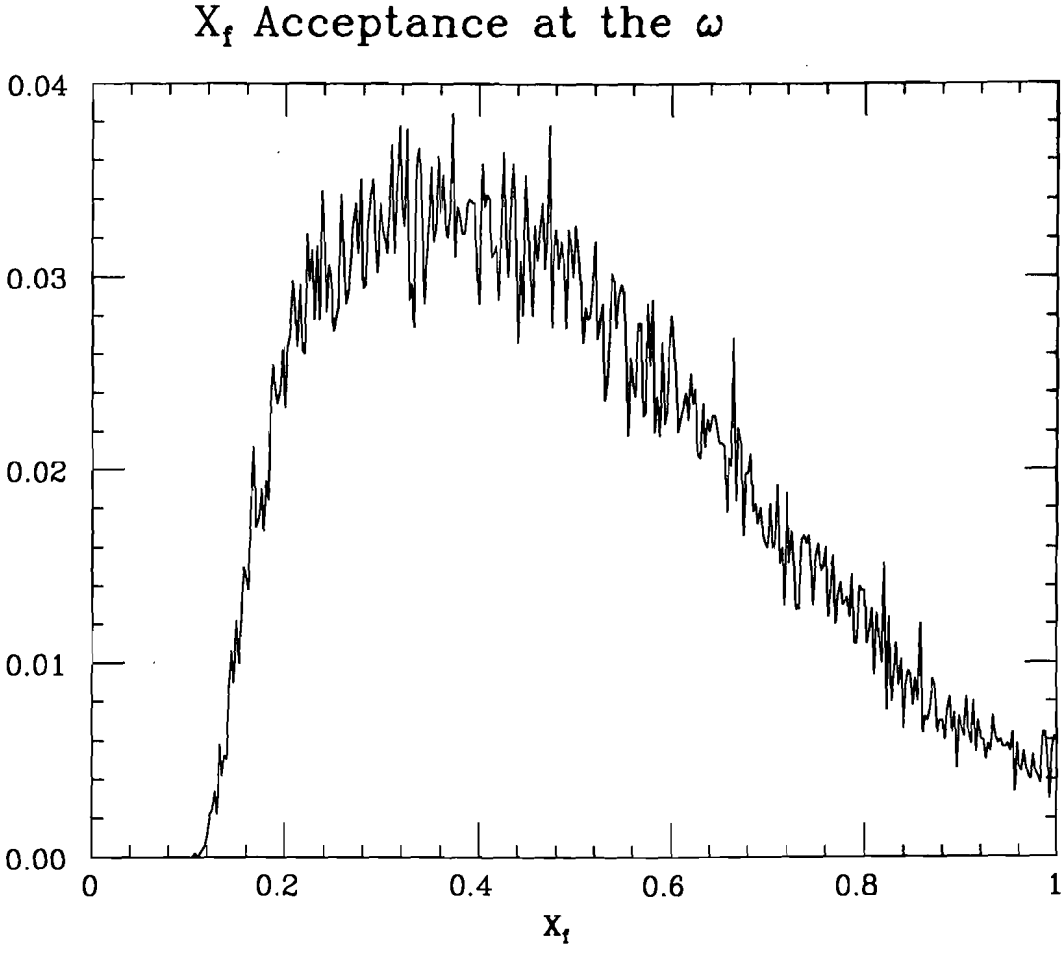

Figure 5-1

Omega acceptance in Feynman-X
Assumes exp(-3.Ø*Pperp**2)

I assumed that the mass plots could be well described by a narrow gaussian (for the omega), a wide gaussian (for the rho), and a quartic background produced as a sum of the first 5 Legendre polynomials. A fit using Legendre polynomials will in general be more "well-conditioned" than a fit using a simple power series. A wide gaussian and a quartic background will tend to interfere; that is to say, there will be strong correlations between the parameters describing the gaussian and the polynomial. Since I had decided against trying to study the rho, this interference is not important to the analysis. All I require is that the background for the omega peak be well fit.

I used MINUIT to fit this function, by first excluding the region around the omega mass, fixing the omega and rho areas at zero, and fitting only the quartic background parameters. Then I allowed the fitter to include the omega region, fixed the quartic background parameters, and allowed the omega and rho parameters to vary. To finish, I allowed everything to vary, and used the results of the final fit. The parameters describing the omega peaks are summarized in Table 5-1 and 5-2 for both pion- and proton-produced omega mesons.

This gave the number of omegas we accepted in each XF interval. These numbers were scaled by our acceptance for each interval, and fit to the various standard forms.

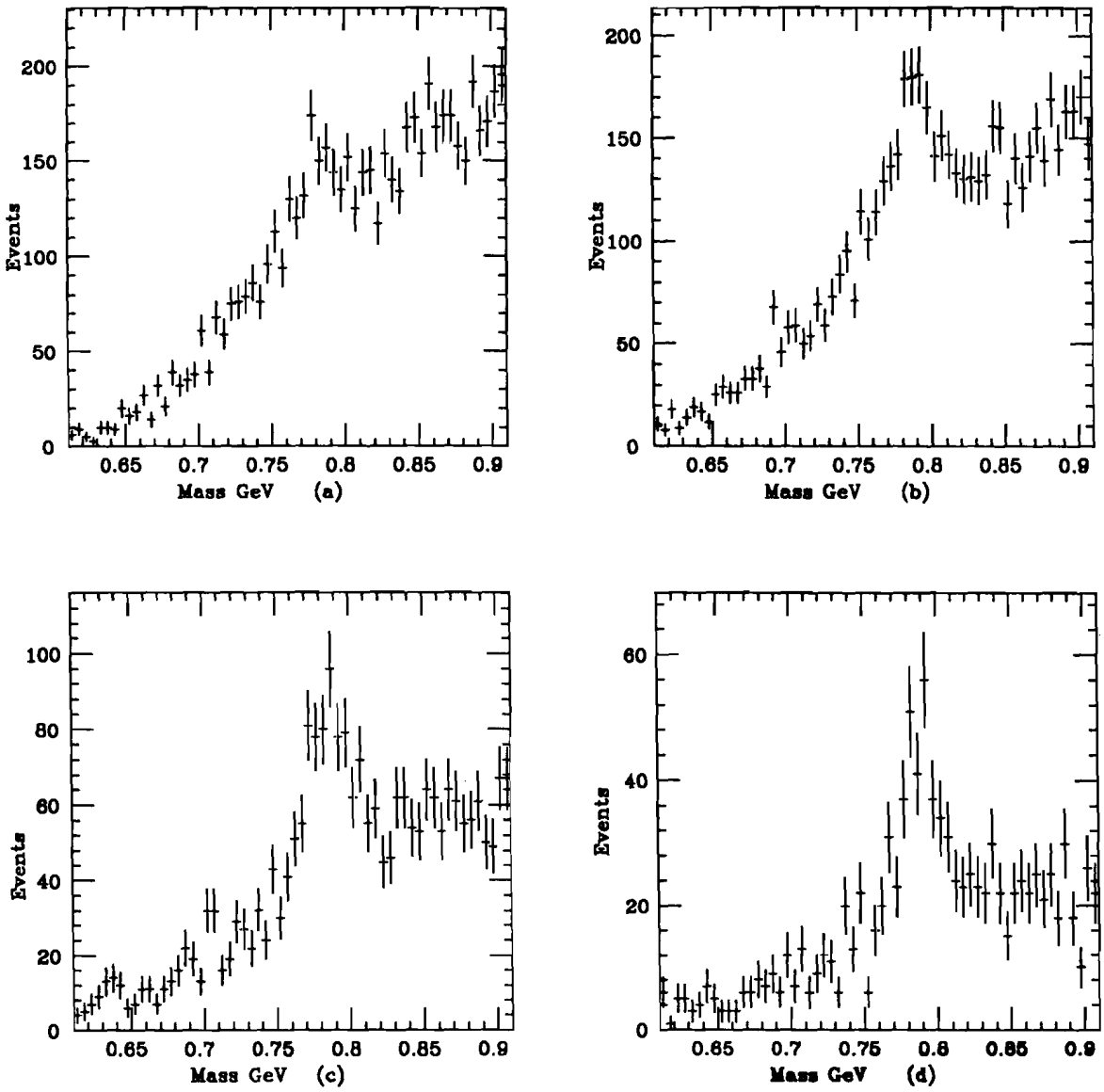

Figure 5-2

Di-muon production for Pperp < 1.0
5 MeV bins
a) 0.1 < XF < 0.2
b) 0.2 < XF < 0.3
c) 0.3 < XF < 0.4
d) 0.4 < XF < 0.5

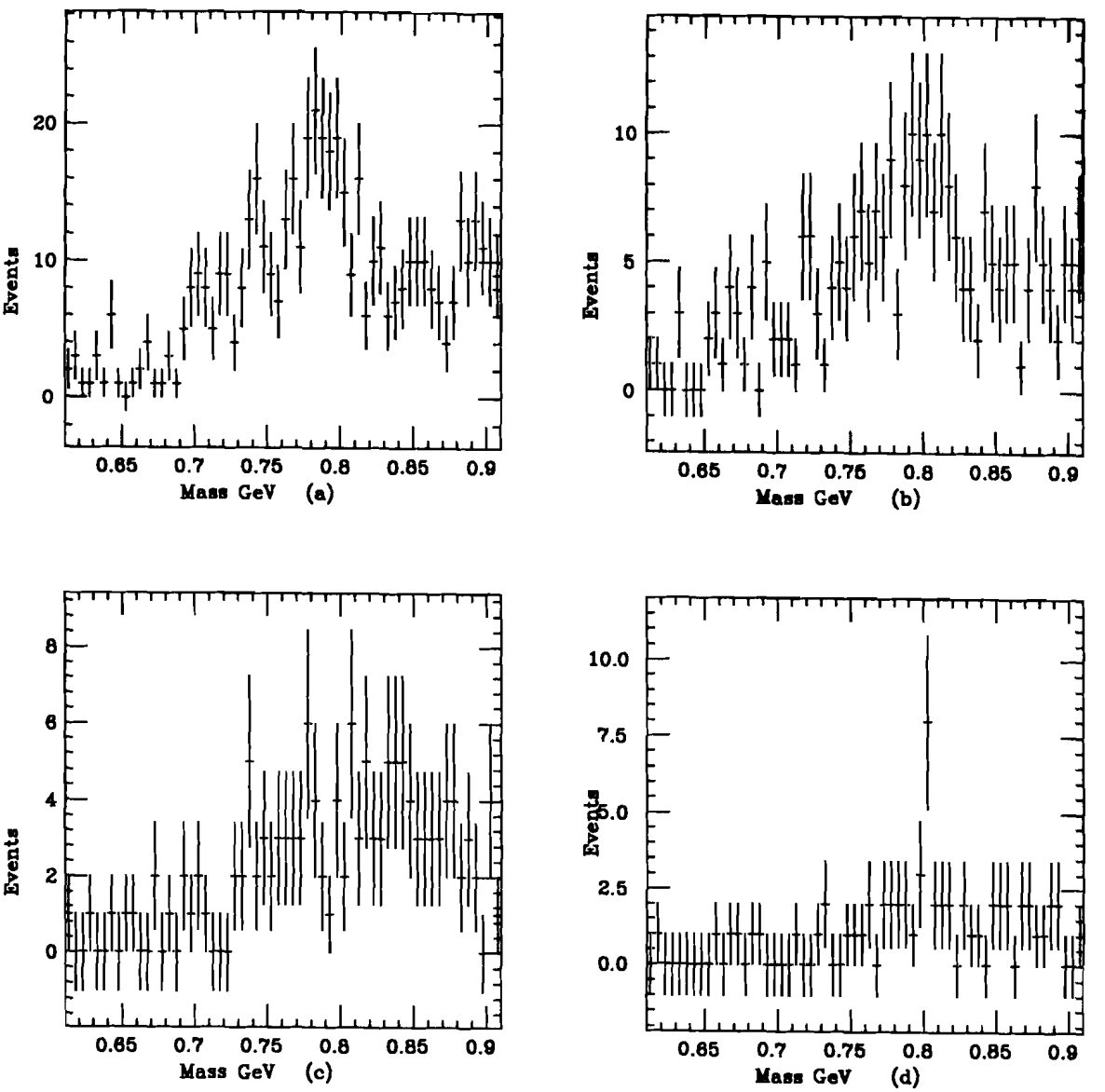

Figure 5-3

Di-muon production for Pperp < 1.0
5 MeV bins
a) 0.5 < XF < 0.6
b) 0.6 < XF < 0.7
c) 0.7 < XF < 0.8
d) 0.8 < XF < 0.9

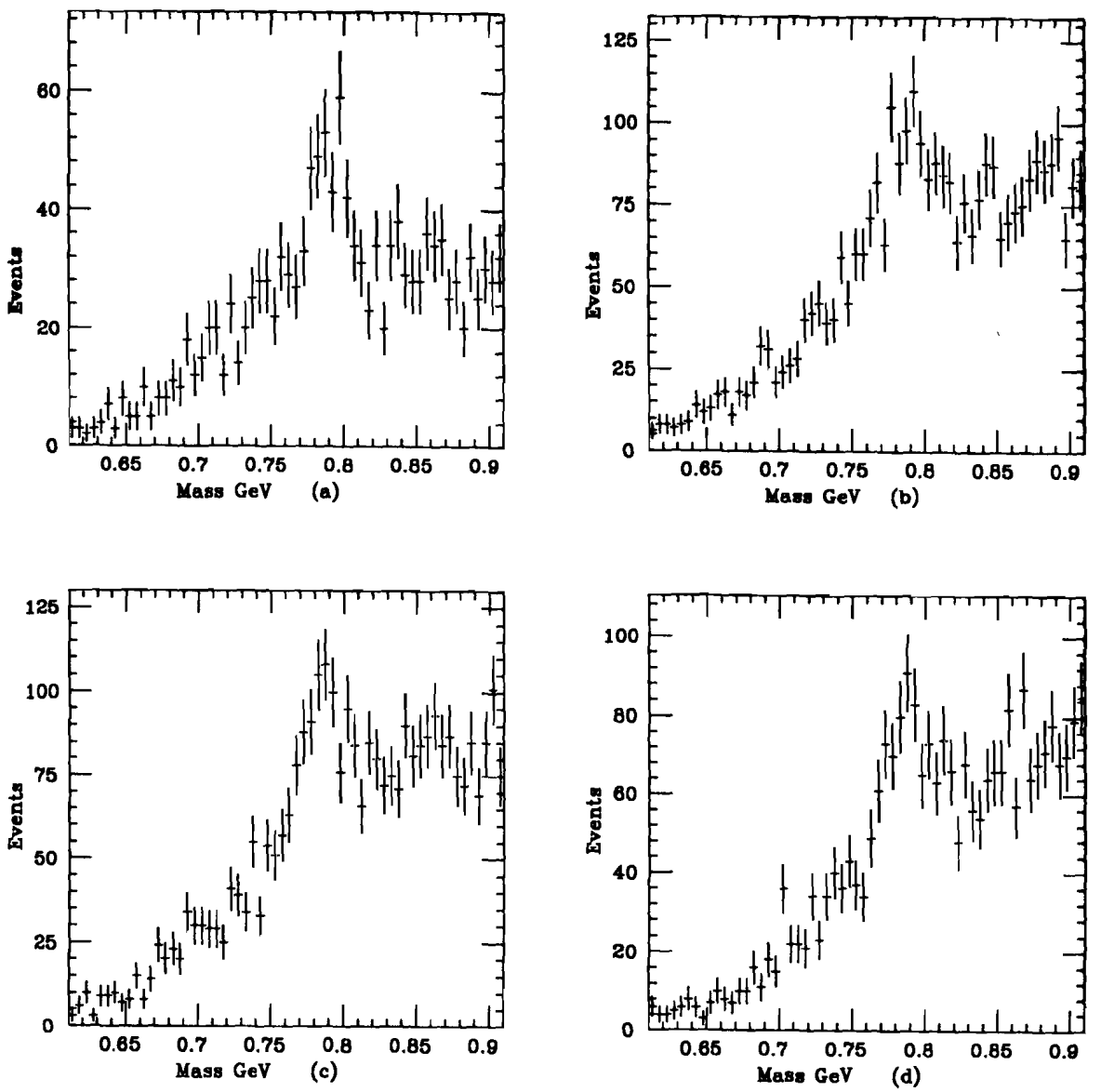

Figure 5-4

Di-muon production for 0.0 < XF < 1.0
5 MeV bins
a) 0.0 < Pperp < 0.1
b) 0.1 < Pperp < 0.2
c) 0.2 < Pperp < 0.3
d) 0.3 < Pperp < 0.4

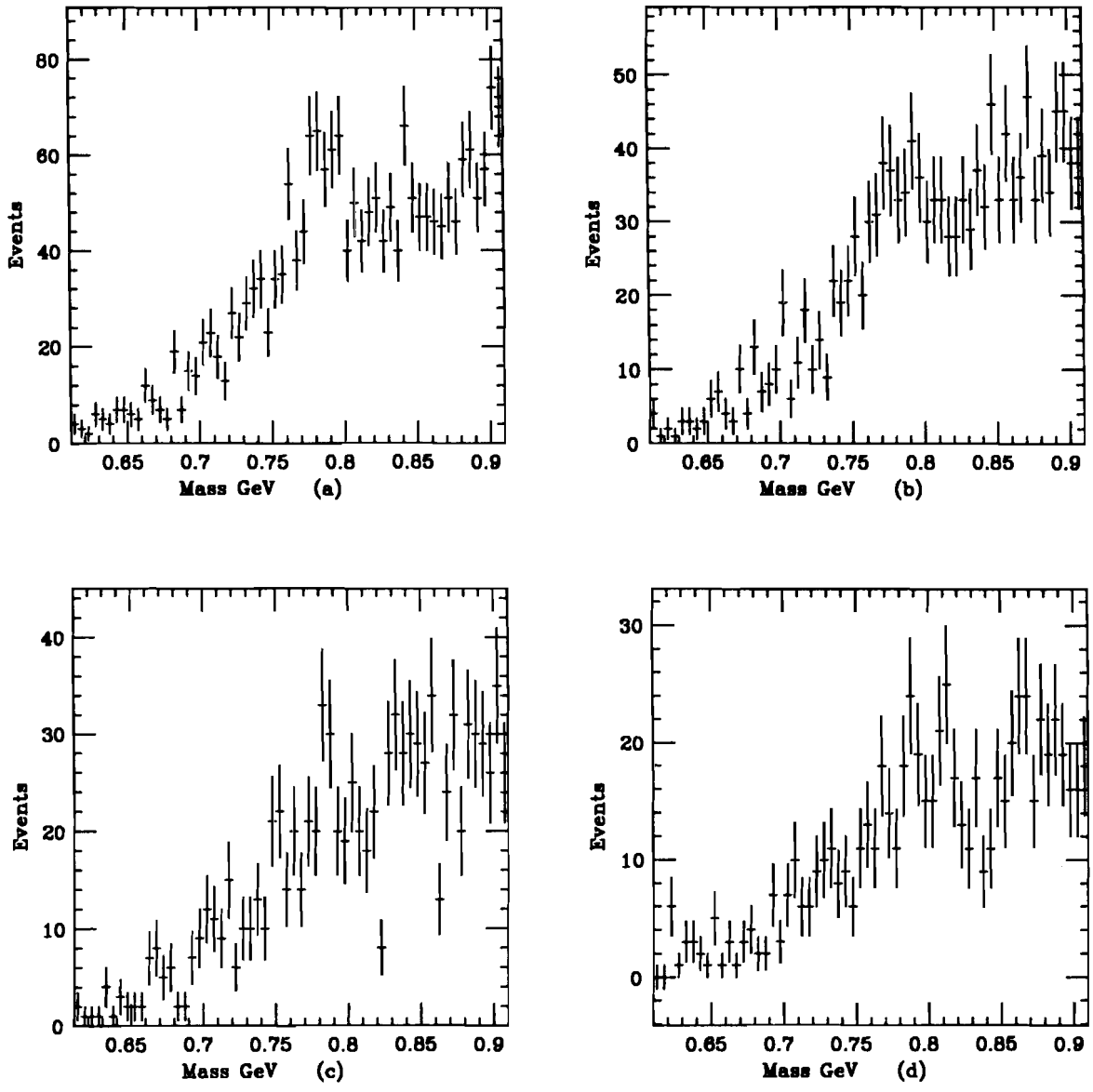

Figure 5-5

Di-muon production for 0.0 < XF < 1.0
5 MeV bins
a) 0.4 < Pperp < 0.5
b) 0.5 < Pperp < 0.6
c) 0.6 < Pperp < 0.7
d) 0.7 < Pperp < 0.8

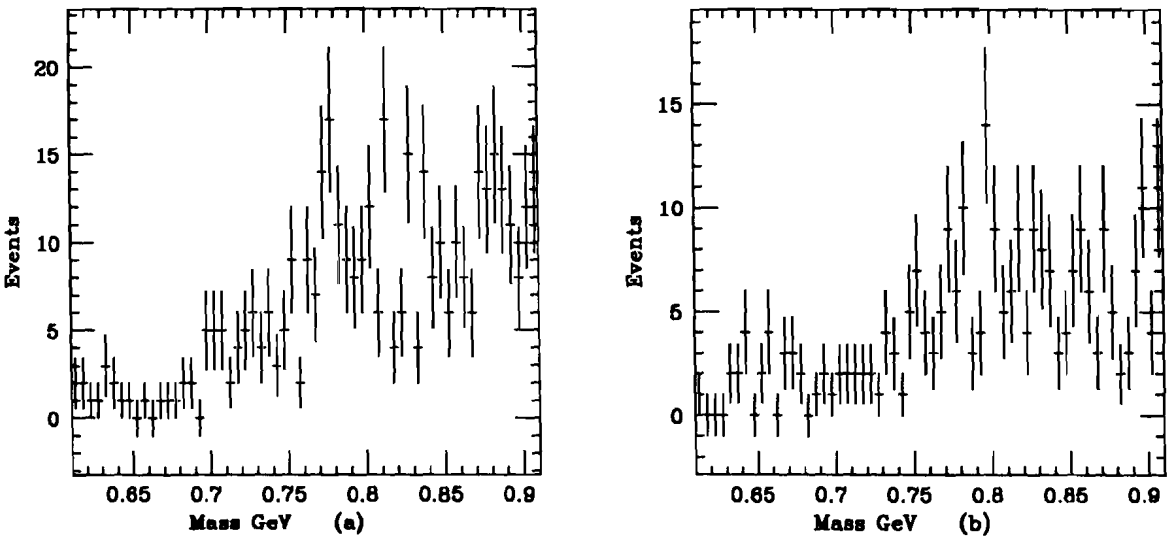

Figure 5-6

Di-muon production for 0.0 < XF < 1.0
5 MeV bins
a) 0.8 < Pperp < 0.9
b) 0.9 < Pperp < 1.0

Table 5-1
Numbers of observed omegas and phis for various XF and Pperp intervals when the beam is 193 GeV/c Negative Pions

OMEGA division	number	+/-	sigma MeV	+/-	peak MeV	+/-
xf .1,.2	240	34	11.3	2.0	782	2
xf .2,.3	275	36	10.7	1.8	788	2
xf .3,.4	322	43	14.2	1.6	785	2
xf .4,.5	194	19	12.7	1.3	788	2
xf .5,.6	52	12	10.6	2.3	789	3
xf .6,.7	33	22	20.0	2.9	790	7
xf .7,.8	6	4	2.9	2.1	779	6
xf .8,.9	13	5	19.0	15.4	790	11
pp 0.,.1	139	26	10.8	1.4	790	2
pp .1,.2	239	38	14.8	2.2	790	2
pp .2,.3	275	51	13.2	2.0	783	2
pp .3,.4	221	52	12.9	2.4	786	2
pp .4,.5	100	17	9.4	2.0	785	2
pp .5,.6	106	19	15.0	2.2	778	16
pp .6,.7	31	12	3.6	1.7	785	1
pp .7,.8	21	8	3.9	1.4	788	2
pp .8,.9	29	9	6.0	2.1	778	2
pp .9,1.	23	16	20.0	11.5	800	17

PHI division	number	+/-	sigma	+/-	peak	+/-
xf 0.,.1	13	6	2.0	1.7	1025	1
xf .1,.2	426	134	24.2	17.9	1018	5
xf .2,.3	295	50	11.5	2.4	1024	2
xf .3,.4	239	49	14.1	2.9	1024	2
xf .4,.5	52	18	4.8	2.2	1031	2
xf .5,1.	41	18	25.0	21.8	1009	16
pp 0.,.1	63	21	10.1	2.9	1039	3
pp .1,.2	89	20	6.3	1.5	1025	2
pp .2,.3	109	24	7.2	1.6	1020	2
pp .3,.4	114	29	7.8	2.4	1017	2
pp .4,.5	219	85	23.3	16.5	1023	6
pp .5,.6	201	49	16.4	3.5	1022	3
pp .6,.7	62	20	12.6	3.5	1025	6
pp .7,1.	117	43	11.2	4.7	1025	3

Table 5-2
Numbers of observed omegas and phis for various XF and Pperp intervals when the beam is 250 GeV/c Negative Protons

OMEGA division	number	+/-	sigma MeV	+/-	peak MeV	+/-
xf .1,.2	156	38	8.2	2.1	786	2
xf .2,.3	191	13	16.7	1.2	788	1
xf .3,.4	62	12	11.4	2.4	788	3
xf .4,.5	36	12	19.9	12.2	780	5
xf .5,.6	11	4	18.0	6.6	797	8
pp 0.,.1	21	14	8.0	3.5	790	11
pp .1,.2	101	20	12.5	2.6	788	3
pp .2,.3	70	20	8.0	1.9	775	3
pp .3,.4	104	18	12.2	2.4	790	3
pp .4,.5	62	17	19.0	9.4	826	8
pp .5,.6	20	12	5.0	2.5	785	3
pp .6,.7	59	13	20.0	15.8	799	6

PHI division	number	+/-	sigma	+/-	peak	+/-
xf 0.,.1	27	15	4.5	2.0	1023	3
xf .1,.2	150	47	10.4	3.8	1018	3
xf .2,.3	56	19	3.8	1.4	1022	1
xf .3,.4	104	36	20.5	5.3	1021	5
xf .4,.5	10	7	12.3	5.1	1009	8
xf .5,1.	9	15	25.0	21.0	1019	19
pp 0.,.1	85	29	25.0	15.9	1005	3
pp .1,.2	38	12	3.2	1.1	1027	1
pp .2,.3	110	33	15.5	4.1	1015	4
pp .3,.4	70	15	4.9	0.8	1021	2
pp .4,.5	100	23	16.8	4.1	1031	5
pp .5,.6	52	17	18.3	5.6	1030	8
pp .6,.7	27	9	3.5	1.3	1023	1
pp .7,1.	6	12	6.6	11.3	1005	26

5.2 Fitting To General Distributions

Several researchers (for example, Ref 9, 34) have found that the differential cross section $\frac{d^3\sigma}{dp^3}$ is only approximately factorable into functions of Feynman-X and perpendicular momentum. The deviation from exact factorability is small at our energies, so I will treat Pperp and XF separately.

Unfortunately, since our acceptance was not flat in Pperp and XF (see Table 4-8), calculating an acceptance for the omega as a function of Pperp requires some assumptions about its distribution as a function of XF, and likewise the acceptance as a function of XF requires assumptions about the Pperp distribution.

Our statistics were not adequate to allow simultaneous fitting of XF and Pperp distributions; so I began by taking the array (see Chapter 4) describing omega acceptance as a function of XF and Pperp, and folded in the distribution determined by the fit parameters of Antipov et al (Ref 8, B = 3.15 (GeV/c)**-2) as an initial guess for the Pperp distribution, and calculated the acceptance in XF. To determine the acceptance in Pperp, I folded the omega acceptance array with the distribution determined by Branson et al (Ref 13) for the XF distribution (D = 2.9).

I then scaled the data using these acceptances, and fit the acceptance-corrected Pperp distribution to

$$A * \exp(- B * Pperp^{**}2)$$

and the acceptance-corrected XF distribution to

C * (1.Ø - XF)**D /XF

I substituted these new parameter values for the initial guesses, and recalculated the acceptances as described above. After two iterations the process converged.

There are two prominent alternatives for the fitting procedure: varying the parameters to minimize the chi-squared of the deviation of the data from the fitting function, and minimizing the negative logarithm of the maximum likelihood function. The latter procedure is subject to less error when the number of data points is small, as was certainly the case here, so these were the values I used. When MINUIT is used to minimize the chi-squared, it returns an error for each parameter which is the variation in the parameter needed to change the chi-squared by 1.Ø, which is a 1-sigma change. I use the error returned from the chi-squared fit to estimate the error in the parameter found by the maximum likelihood method.

In several of the plots, the data looked poor, especially for the phi. I took the liberty of dropping low statistics (high error) points from the high and low ends of the plots, and in some instances also re-binned, so that instead of intervals Ø.1 GeV/c wide in Pperp the plot used Ø.2 GeV/c intervals. This gave satisfactory results in all but one of the cases: that of pion-produced phis distributed as a function of Pperp. In the mass plots used to create this distribution, there are 6Ø - 8Ø MeV/c**2 wide phi signals in the mass plots with Pperp < Ø.4 GeV/c and with Pperp > Ø.6 GeV/c, but the two remaining have phi widths of 16Ø - 22Ø MeV/c**2. There are

substantially more phis found in these mass plots. As a result, there is a peak in the Pperp distribution at about Ø.5 GeV/c . I omit this peak from the fit.

Many theorists prefer to fit the Pperp distribution to

A * exp(-B*Pperp)

a simple exponential instead of a gaussian. I decided to fit to this hypothesis as well. In addition, I decided to test a "null hypothesis": a distribution in XF without a pole at XF = Ø, since my data did not obviously display such a feature. To accomodate these, I fit the data under 4 hypotheses:

Hypothesis 1) The Pperp distribution was gaussian and the XF distribution was of the form (1-XF)**D /XF .

Hypothesis 2) The Pperp distribution was gaussian and the XF distribution was of the form (1-XF)**D .

Hypothesis 3) The Pperp distribution was exponential and the XF distribution was of the form (1-XF)**D /XF .

Hypothesis 4) The Pperp distribution was exponential and the XF distribution was of the form (1-XF)**D .

The results of these fits, together with their chi-squared values, are summarized in Tables 5-3 through 5-6. In some cases, the maximum-likelihood-minimization (ML) method resulted in a dramatic rise in the value of the chi-squared. When the chi-squared per

degree of freedom exceeded 2.0, I rejected the fit.

Notice that the exponent in the fits to XF distributions is not very sensitive to the form of the Pperp distribution; at most it changes by 4%, well within the error on the exponent. I used this stability to attempt a different fit to XF distributions, using the exponential Pperp hypothesis. The function was

$$F * (1 - XF)^{**}G / XF^{**}H$$

where H is allowed to vary as well. I allowed two cases: H positive and H unrestricted. The results are summarized in Table 5-7. Some improvement in the total chi-squared is obtained, but the chi-squared per degree of freedom is increased, and the value of H varies considerably between the chi-squared and maximum likelihood fits. I cannot regard these fits as satisfactory, and judge that further refinements of the fitting function are likely to be fruitless excercises.

The chi-squared per degree of freedom for Pperp fitting is smallest when the fitting function is gaussian. Generally the gaussian hypothesis and the exponential hypothesis result in fits with chisquared per degree of freedom which are about the same (as 0.45 vs 0.48, or 0.49 vs 0.53), but when they differ substantially, the gaussian is the better fit (1.10 vs 2.64). Notice that the fits are usually good in either case. The fits to the XF distribution have the smallest chi-squared per degree of freedom when the Pperp distribution is assumed to be gaussian. I can therefore tentatively assert that presuming the Pperp distribution to be gaussian gives a

better fit—and is more likely to be correct—than presuming it to be exponential.

The XF distributions are less well fit than the Pperp distributions. They seem to be better fit when the fitting distribution is (1-XF)**D rather than (1-XF)**D /XF . I have virtually no data in the critical region near XF = 0, so I cannot claim that the null hypothesis is correct, but it does fit this limited range of XF better. For example, the chi-squared per degree of freedom for pion-produced phis is 0.65 for the null hypothesis, vs 1.20 for fitting with the usual curve.

Figures 6-1 and 6-2 show the Pperp and XF fits to the data. For the Pperp distributions, I assumed that the XF distributions were of the form (1-XF)**D /XF. For the XF distributions, I assumed that the Pperp distributions were gaussian. The proton data is too ragged to trust for more than discovering general trends. The pion-produced omega data, for which I have better statistics, seems to the eye to be better fit by the (1-XF)**D /XF.

5.3 Fitting To Phenomenological Distributions

If the omega meson is produced by simple parton fusion, with no higher order complications, one may use the parton distributions calculated by other experimenters and theorists, and try to calculate

Table 5-3

Parameters Fit Using Hypothesis 1

Type	chi-squared A	chi-squared δA	chi-squared ch2/DF	maximum likelihood A	maximum likelihood δA	maximum likelihood ch2/DF	DF
Pion omega Pperp	4.4	0.5	1.10	4.2	0.5	1.26	6
Proton omega Pperp	3.4	0.9	0.45	3.5	0.9	0.46	2
Pion phi Pperp	1.9	0.3	0.65	2.5	0.3	1.24	5
Proton phi Pperp	3.5	1.3	0.49	3.5	1.3	0.49	3

Type	chi-squared B	chi-squared δB	chi-squared ch2/DF	maximum likelihood B	maximum likelihood δB	maximum likelihood ch2/DF	DF
Pion omega XF	2.0	0.2	1.27	2.0	0.2	1.42	4
Proton omega XF	2.6	0.8	1.01	2.1	0.8	1.15	3
Pion phi XF	4.5	0.7	1.20	3.7	0.7	1.92	2
Proton phi XF	3.7	0.9	2.23	2.3	0.9	8.35	1

This table uses hypothesis 1, that the Pperp distribution varies as EXP(- A * Pperp**2), and that the XF distribution varies as (1 - XF)**B /XF . DF is the number of degrees of freedom of each fit.

Table 5-4

Parameters Fit Using Hypothesis 2

Type	chi-squared A	δA	ch2/DF	maximum likelihood A	δA	ch2/DF	DF
Pion omega Pperp	4.4	0.5	1.14	4.2	0.5	1.31	6
Proton omega Pperp	3.4	0.9	0.45	3.5	0.9	0.46	2
Pion phi Pperp	1.8	0.4	0.62	2.4	0.4	1.17	5
Proton phi Pperp	3.5	1.3	0.49	3.5	1.3	0.49	3

Type	chi-squared B	δB	ch2/DF	maximum likelihood B	δB	ch2/DF	DF
Pion omega XF	3.7	0.5	1.11	4.2	0.5	1.66	4
Proton omega XF	5.3	1.2	1.77	4.6	1.2	2.37	3
Pion phi XF	6.9	0.8	0.65	6.7	0.8	0.73	2
Proton phi XF	6.5	1.0	0.60	5.7	1.0	1.55	1

This table uses hypothesis 2, that the Pperp distribution varies as EXP(- A * Pperp**2), and that the XF distribution varies as (1 - XF)**B. DF is the number of degrees of freedom.

Table 5-5

Parameters Fit Using Hypothesis 3

Type	chi-squared A	δ A	ch2/DF	maximum likelihood A	δ A	ch2/DF	DF
Pion omega Pperp	3.2	0.3	2.64	2.7	0.3	3.92	6
Proton omega Pperp	2.5	0.6	0.48	2.5	0.6	0.54	2
Pion phi Pperp	1.9	0.3	0.38	2.2	0.3	0.56	5
Proton phi Pperp	3.1	1.1	0.52	3.0	1.1	0.52	3

Type	chi-squared B	δ B	ch2/DF	maximum likelihood B	δ B	ch2/DF	DF
Pion omega XF	2.0	0.4	1.38	2.0	0.4	1.54	4
Proton omega XF	2.6	0.8	1.38	2.1	0.8	1.52	3
Pion phi XF	4.5	0.6	1.19	3.7	0.6	1.88	2
Proton phi XF	3.7	0.5	2.22	2.3	0.5	8.18	1

This table uses hypothesis 3, that the Pperp distribution varies as EXP(- A * Pperp), and that the XF distribution varies as (1 - XF)**B /XF . DF is the number of degrees of freedom.

Table 5-6

Parameters Fit Using Hypothesis 4

Type	chi-squared A	chi-squared δ A	chi-squared ch2/DF	maximum likelihood A	maximum likelihood δ A	maximum likelihood ch2/DF	DF
Pion omega Pperp	3.2	0.3	2.64	2.7	0.3	3.92	6
Proton omega Pperp	2.5	0.6	0.48	2.5	0.6	0.54	2
Pion phi Pperp	1.9	0.3	0.38	2.1	0.3	0.56	5
Proton phi Pperp	3.1	1.1	0.53	3.0	1.1	0.52	3

Type	chi-squared B	chi-squared δ B	chi-squared ch2/DF	maximum likelihood B	maximum likelihood δ B	maximum likelihood ch2/DF	DF
Pion omega XF	3.6	0.5	1.24	4.2	0.5	2.11	4
Proton omega XF	5.3	1.1	1.81	4.6	1.1	2.45	3
Pion phi XF	6.9	0.8	0.66	6.7	0.8	0.72	2
Proton phi XF	6.5	1.0	0.59	5.7	1.0	1.55	1

This table uses hypothesis 4, that the Pperp distribution varies as EXP(- A * Pperp), and that the XF distribution varies as (1 - XF)**B. DF is the number of degrees of freedom.

Table 5-7
Parameter Fits When the Denominator
Power is Variable

Type		chi-squared value	chi-squared error	chi-squared ch2/DF	maximum likelihood value	maximum likelihood error	maximum likelihood ch2/DF	DF
Pion	A	3.4	0.3	1.64	1.0	0.3	2.35	3
omega	B	0.1	0.1		1.5	0.1		
Proton	A	1.7	0.4	1.99	2.7	0.4	2.53	2
omega	B	1.4	0.1		0.8	0.1		
Pion	A	6.9	0.8	1.31	6.7	0.8	1.44	1
phi	B	0.0	1.6		0.0	1.6		
Proton	A	6.5	2.0	0.60/0	5.7	1.0	1.53/0	0
phi	B	0.0	1.1		0.0	1.1		

The above table contains, for each entry, the values of the power of (1-XF)**A and (1/XF)**B respectively, with B constrained to be non-zero.

Type		chi-squared value	chi-squared error	chi-squared ch2/DF	maximum likelihood value	maximum likelihood error	maximum likelihood ch2/DF	DF
Pion	A	3.6	1.5	1.48	1.0	1.5	2.21	3
omega	B	0.1	0.9		1.5	0.9		
Proton	A	1.7	0.2	1.84	2.8	0.2	2.36	2
omega	B	1.4	0.1		0.7	0.1		
Pion	A	8.0	0.3	1.20	6.6	0.3	1.50	1
phi	B	-0.5	0.1		0.0	0.1		
Proton	A	9.1	0.6	0.00/0	9.1	0.6	0.00/0	0
phi	B	-0.9	0.2		-0.9	0.2		

For each entry, this table contains the values of the power of (1-XF)**A and (1/XF)**B respectively, with B unrestricted.

This table uses the hypothesis that the XF distribution varies as EXP(-C * XF) (see Table 6-4), and that the XF distribution varies as (1 - XF)**A / (XF**B) . DF is the degrees of freedom.

the relative production rates. For example, the distributions used in Daum et al (Ref 28) in fitting to the phi combine naturally into three "product distributions" when used to determine the cross-section. There is a distribution describing the fusion of strange quarks (which for the omega I neglect), a distribution describing the fusion of light quarks, and a distribution describing the fusion of gluons. See Chapter 2 for more details.

I consider each "product distribution" to be independent, and try to fit the omega XF distribution with a linear combination of these two (three if studying the phis) phenomenological distributions. Since here I am studying production, I require that the coefficient of each phenomenological distribution in the sum be non-negative, to represent creation rather than annihilation. The phenomenological distributions are functions of the meson mass and the total available energy, so there are 4 sets of product distributions, one for each combination of meson type and beam type.

We do not understand our beam very well, so our normalization for cross-sections is unknown. I therefore cannot use these coefficients to describe absolute production rates, but only relative rates. Rather than list these coefficients, I will calculate the relative production of each process.

Before one can calculate relative production, one must know the normalization of the distributions involved. These were found by numerical integrations of the distributions in meson XF over the

interval in XF in which there was reasonable data. The relative production rates are in Table 5-8. Notice that there are frequently large differences between the chi-squared fit results and the maximum likelihood fit results. In only two cases are the calculated contributions even remotely stable, and in only one of these is the resulting ratio of relative productions good. Both of these are in the table of fits using the Daum et al phenomenological distributions; the Kuhn distributions seem quite similar.

For the Daum et al distributions and the pion beam, the relative production in the positive XF region of omegas due to light quark fusion and due to gluon fusion is calculated as 0.473 +/- 0.115 if the chi-squared fit is used and as 0.544 +/- 0.119 if the maximum likelihood fit is used. The Kuhn distributions give 0.430 +/- 0.126 and 0.483 +/- 0.126 for the same fits, respectively. If I treat these all as independent measurements of the same quantity, I get an average of 0.483 +/- 0.126 for the ratio of production of omegas by light quark fusion to production by gluon fusion in the Feynman-X region from 0.1 to 0.7, when the incident beam is negative pions at 193 GeV/c and the target is beryllium.

The only other ratio which is even partly stable is that for the pion-produced phi, and it has a chi-squared per degree of freedom greater than 2.5 . Nevertheless, using the chi-squared fit the ratio of phis produced by strange quark fusion to those produced by light quark fusion is 6.75 +/- 3.78 , and for maximum likelihood the same ratio is 4.17 +/- 1.56. The Kuhn values are 5.48 +/- 2.61 and 3.44

+/- 1.42 respectively. Daum et al find values which would translate to 2.1 for our experiment. Our numbers seem to be consistent with this, but our errors are quite substantial. Notice that I find little contribution due to gluon fusion.

From the fact that there are other strange particles in less than half of all phi events (not produced by K beams)one may conclude that the fusion of strange quarks from the sea can account for less than half of the phi production. The results of Daum et al are consistent with this, but my results are not.

The fit to proton-produced omegas has a fair chi-squared per degree of freedom, but the fit parameters have too much play. The production ratio (light quark to gluon) is found to be for the Daum fits, 0.179 +/- 0.108 (chi-squared) and 0.442 +/- 0.140 (maximum likelihood); and for the Kuhn fits, 0.344 +/- 0.268 (chi-squared) and 0.844 +/- 0.337 (maximum likelihood). Here the Kuhn distribution fits result in production ratios twice the size of the Daum results,

Table 5-8
Contributions of Daum "Product Distributions" to Meson production

	Chi-squared VALUE	+/- ERROR	ch2/DF	Maximum Likelihood VALUE	+/- ERROR	ch2/DF
pion omega						4 DF
STRANGE	0	0	1.39	0	0	1.52
LIGHT	1390	280		1620	280	
GLUON	2950	400		2980	400	
proton omega						3 DF
STRANGE	0	0	1.30	0	0	1.42
LIGHT	190	110		390	110	
GLUON	1050	120		890	120	
pion phi						2 DF
STRANGE	910	150	2.59	900	150	3.03
LIGHT	140	73		220	73	
GLUON	0	320		1	320	
proton phi						0 DF
STRANGE	480	520	2.19/0	0	520	6.08/0
LIGHT	0	200		79	210	
GLUON	180	320		480	320	

This lists the contributions of the STRANGE, LIGHT, and GLUON distributions, described in the text, in fits to the data Feynman-X distributions. All contributions are constrained to be non-negative. The above used the Daum et al distributions.

Table 5-8
Contributions of Kuhn "Product Distributions" to Meson production
(continued)

	Chi-squared VALUE	+/- ERROR	ch2/DF	Maximum Likelihood VALUE	+/- ERROR	ch2/DF
pion omega						4 DF
STRANGE	0	0	1.38	0	0	1.52
LIGHT	1310	330		1500	330	
GLUON	3040	430		3110	430	
proton omega						3 DF
STRANGE	0	0	1.30	0	0	1.43
LIGHT	330	250		700	250	
GLUON	960	140		830	140	
pion phi						2 DF
STRANGE	900	130	2.20	690	130	2.98
LIGHT	160	74		200	74	
GLUON	0	340		200	340	
proton phi						0 DF
STRANGE	350	390	2.25/0	0	390	5.99/0
LIGHT	0	310		120	310	
GLUON	250	230		470	230	

This contains the contributions of the Kuhn distributions when fit to our Feynman-X distributions. The units are arbitrary.

which casts doubt on the fitness of either distribution in the proton-produced omega data. Still, it agrees with the pion data in claiming that a majority of the omegas in this XF interval were produced by gluon fusion, as opposed to quark fusion.

The ratios of quark, gluon, and strange quark fusion contributions varied wildly between the chi-squared minimization and the maximum likelihood fit for the Morion distributions. Since these were not really appropriate for the mass regions in question, it comes as no suprise that they did not produce a good fit.

The TWOQ distributions were only used to try to fit the pion-produced omega distribution. The chi-squared and maximum likelihood fits were consistent, within errors. Both asserted 100% gluon fusion and 0% quark fusion. This seems unlikely. Using the extrapolated distribution for valence pion quarks instead gave the same result.

The contributions using the TWOQ distributions were:

For the chi-squared fit: Chi2/DF = 1.11

Light	0	+/- 1900
Gluon	4100	+/- 422

For the maximum likelihood fit: Chi2/DF = 1.94

Light	100	+/- 1900
Gluon	4700	+/- 422

Chapter 6

Summary

6.1 Perpendicular Momentum

As may be seen from Figure 6-1, the perpendicular momentum distributions of the omega and phi are fit somewhat better by the gaussian than by the exponential curves. The coefficients A of the gaussian curves are consistent with the so-called "universal" (Ref 59) slope parameter 3.1 +/- 0.2 (GeV/c)**-2. I find that, assuming the mesons' Feynman-X (XF) distributions are (1-XF)**C/XF (Table 5-3),

for pion-produced omegas A = 4.23 +/- 0.47

for proton-produced omegas A = 3.50 +/- 0.92

for pion-produced phis A = 2.49 +/- 0.36

for proton-produced phis A = 3.50 +/- 1.26

The units of A are (GeV/c)**-2.

No startling deviations were predicted, and none seem to appear, although the ratio of the distribution of pion-produced omegas to pion-produced phis has an A of 1.74 +/- 0.83, suggesting that phis are produced with larger Pperp than omegas, on the average. This is only a two-standard deviation effect, however, and may not be real.

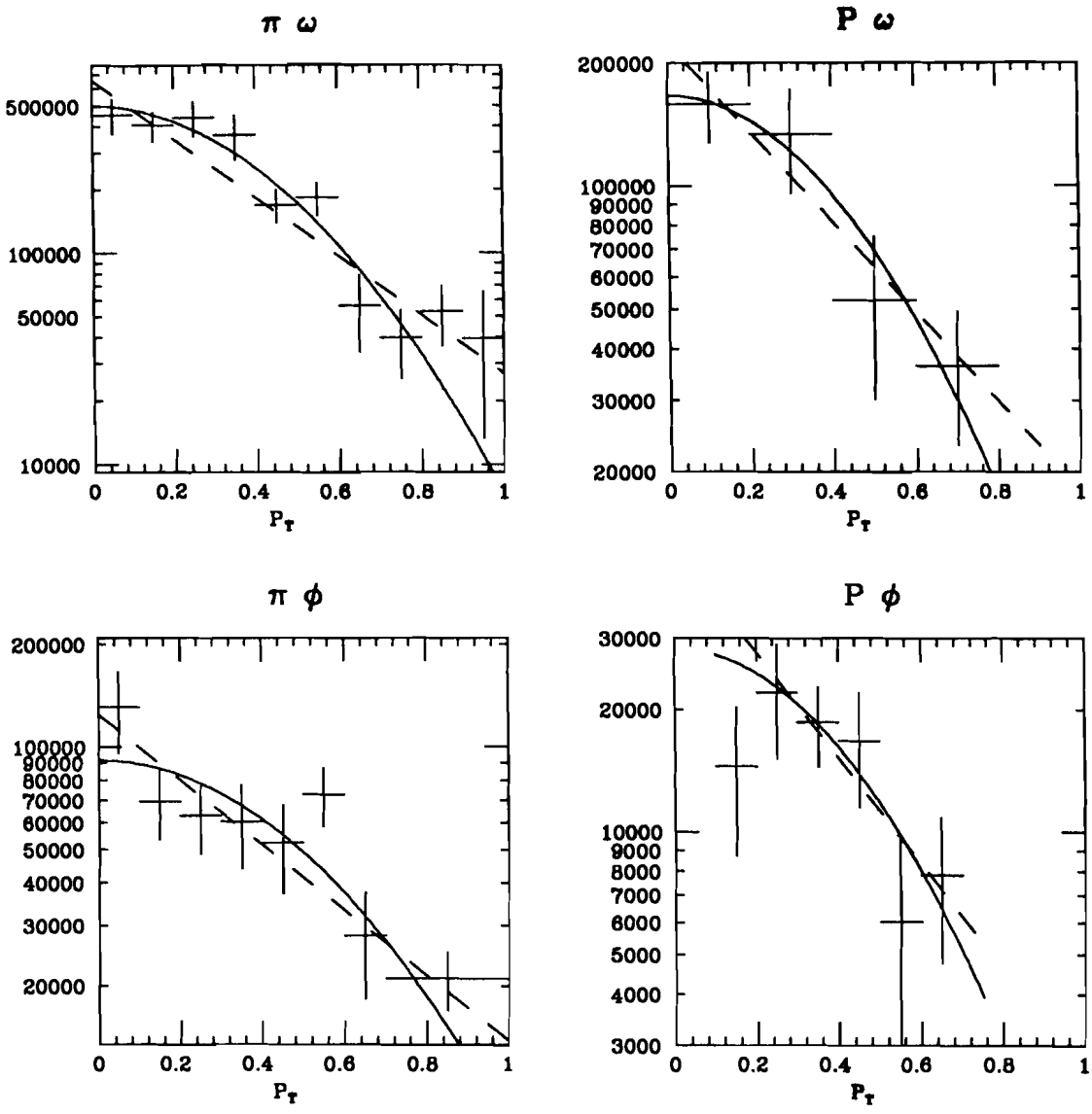

Figure 6-1

Perpendicular momentum distributions
exp (- A * Pperp**2) - solid
exp (- A * Pperp) - dashed

6.2 Feynman-X Distributions

The ratio of two Feynman-X distributions has the form (1-XF)**A. The ratio of the distribution for phis to that for omegas has A = 1.7 +/- 0.9 for the pion data and A = 1.6 +/- 1.7 for the proton data. Since the XF of the forward-going meson depends strongly on the XF of the beam particle parton involved, I can use the beam parton distribution as a rough estimate of the meson distribution. In the Daum et al distributions, the ratio of the pion strange quark distribution to the gluon distribution has an A of 1.4. As you can see, the ratios are roughly the same. For the proton, the ratio of strange quark XF distributions to gluon XF distributions has an A of about 4.0, which does not closely resemble 1.6 +/- 1.7. Nevertheless, it is clear that phi production falls off more rapidly in XF than omega production by pions.

6.3 Gluon Fusion And Quark Fusion

I made several fits of phenomonological "product distributions" to my meson XF distributions. If I treat all the results as independent, I find that for omegas produced by a negative pion beam on a beryllium target, with a Feynman-X between 0.1 and 0.7 and a perpendicular momentum less than 1.0 GeV/c, the ratio of omegas produced by light quark fusion to the ratio of omegas produced by

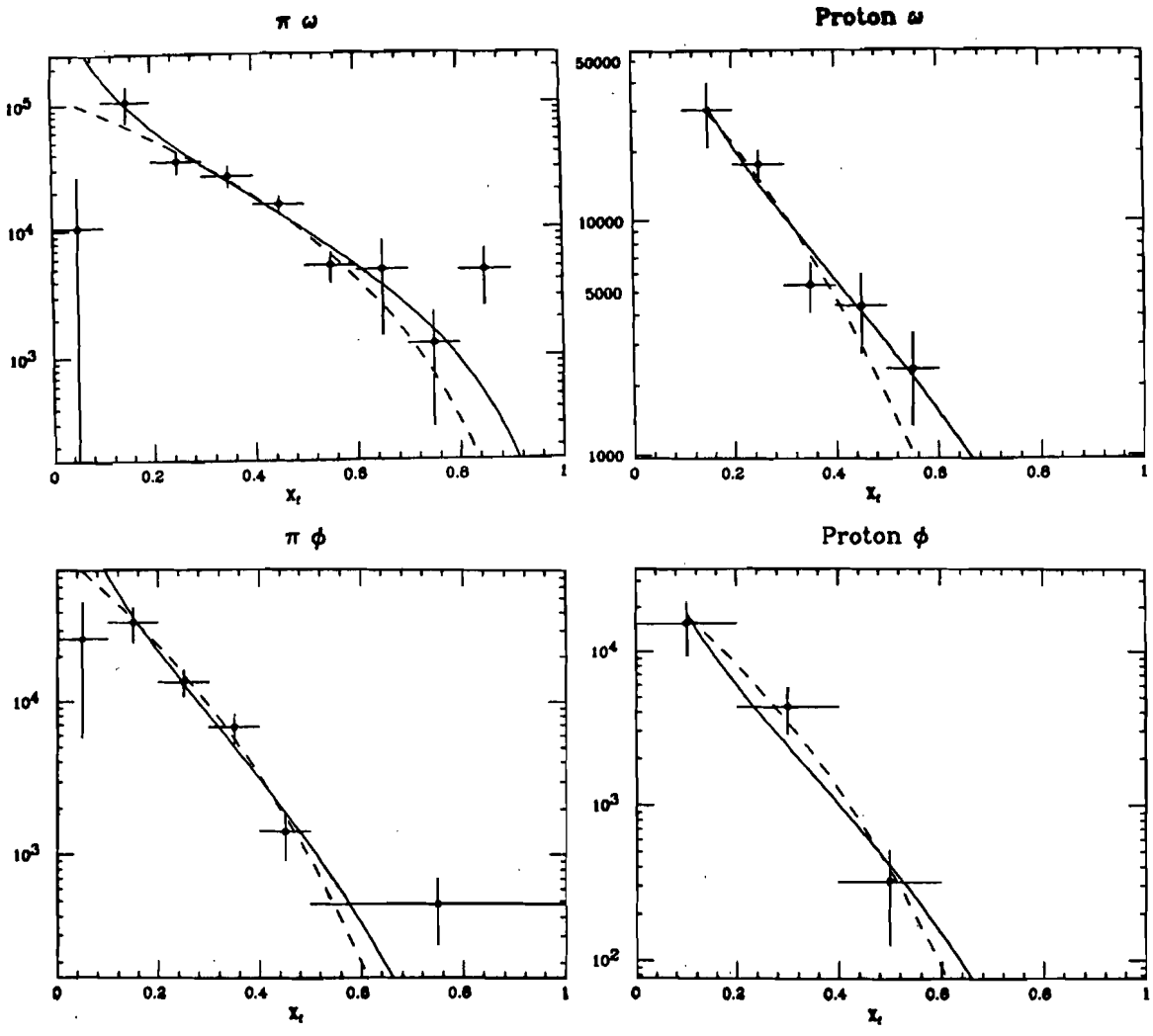

Figure 6-2

Distributions in Feynman-X
(1-XF)**E /XF - solid
(1-XF)**E - dashed

gluon fusion, in the simplest approximation, is 0.48 +/- 0.13. In other words, 32% +/- 9% of these omegas came from light quark fusion, and 68% +/- 9% came from gluon fusion. Though the gluon distributions were the same in both references, I used two independent estimates for the light quark distributions, and found good agreement between them.

This result contradicts the conclusions of other experimenters, some of whose conclusions were touched on in Chapter 2, who claim that both the rho and the omega are produced by quark fusion. These experiments did not study the Feynman-X distributions of the partons, but instead studied relative production rates by various beam particles on various targets, such as Be, or protons, or requiring multiple interactions in a nucleus.

There are several possible explanations of this discrepancy.

First, omegas could be produced primarily by gluon fusion. This is possible, but seems somewhat unlikely. The cross sections for rho production by pi-minus, K-minus, pi-plus, and K-plus are as follows (Ref 49, 64).

Cross Sections for rho

beam energy GeV/c	beam particle pi-	K-	beam energy GeV/c	beam particle pi+	K+
16	4.7	2.9	22,32	6.0	3.1
100	7.7	4.3 (mb)	147	9.8	7.7 (mb)

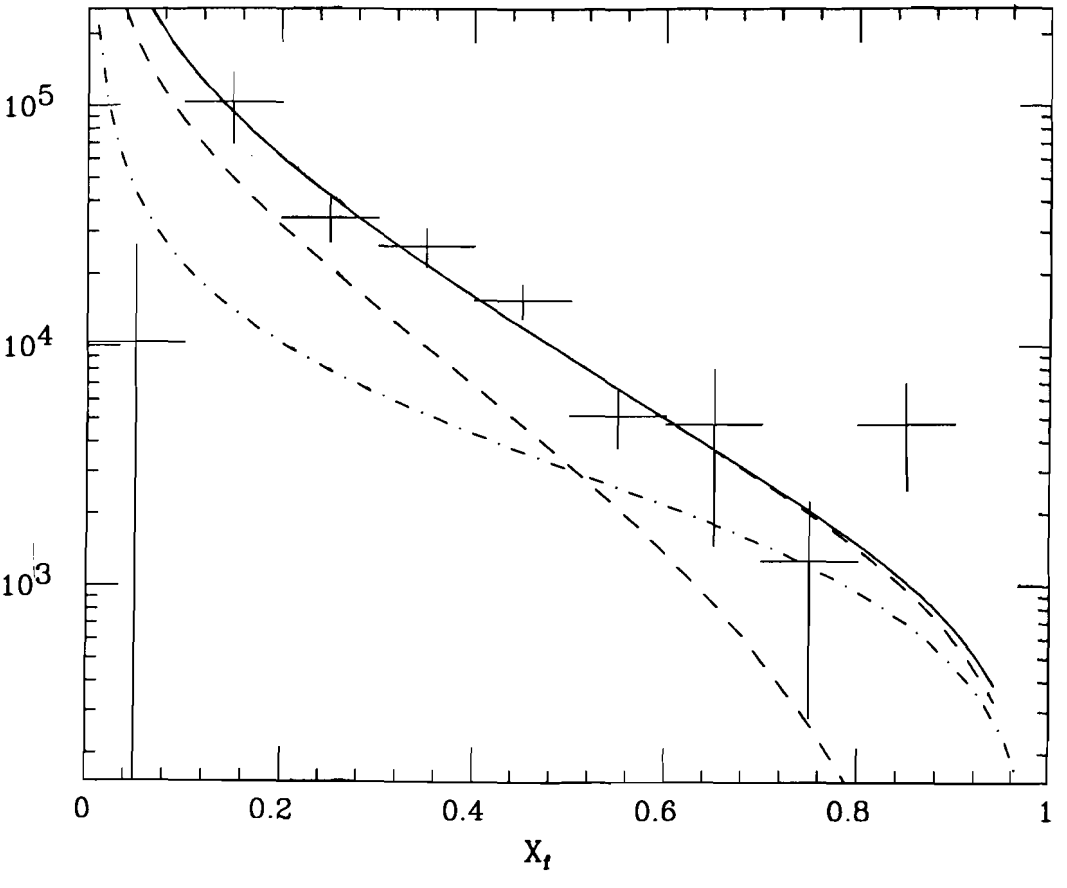

Figure 6-3 a

Pion-produced omega Feynman-X distribution
as fit by the "product distributions" of
Daum et al - solid
Kuhn - dashed (overlapping)
The quark fusion (dot-dash) and gluon fusion
(dashed) components are plotted below.

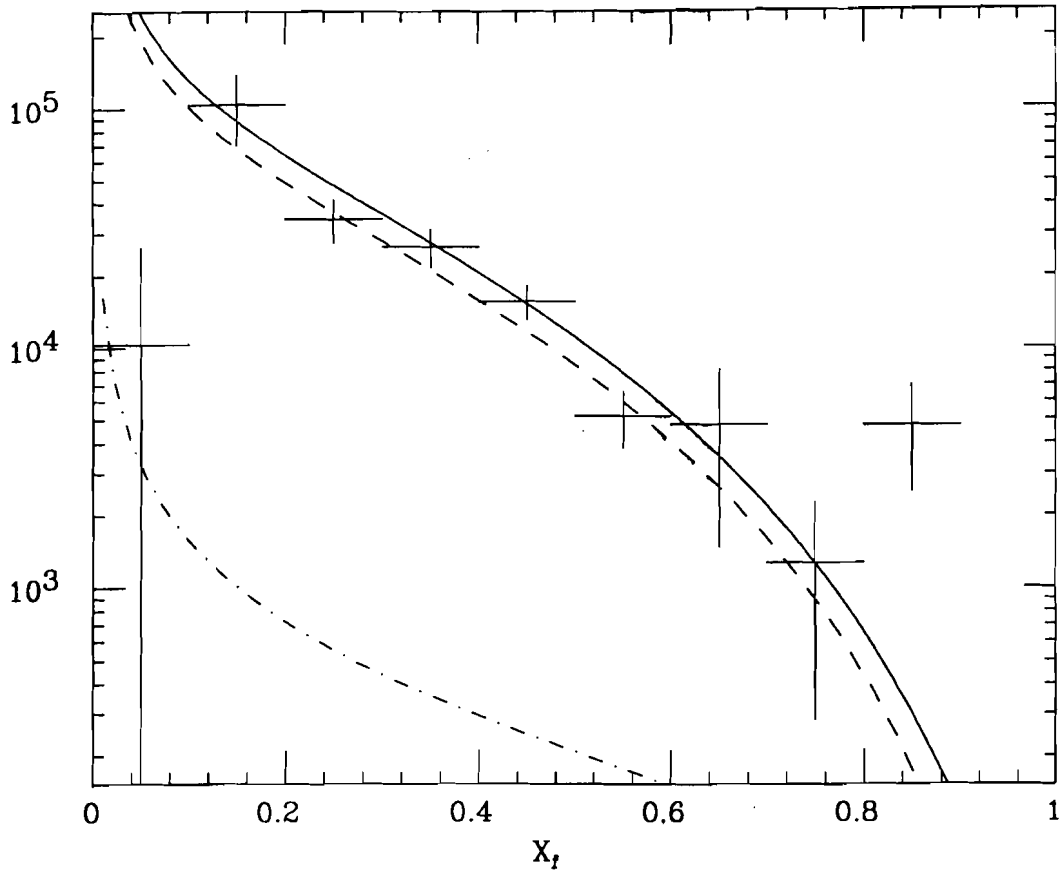

Figure 6-3 b

Pion-produced omega Feynman-X distribution as fit by the "product distributions" of the TWOQ parton distributions.
The quark fusion (dot-dash) and gluon fusion (dashed) components are plotted below.

If the mesons were formed by beam valence quark "dressing" (a scattered quark or anti-quark pair-produces an appropriate mate) the cross sections would be in the ratio 2:1:2:1. The above results are consistent with quark "dressing", though there seems to be some deviation at higher center-of-mass energies. Further, if the vector mesons are formed by "dressing" scattered valence quarks, then in the forward direction, with a kaon beam, the ratio of KØ* mesons to rho mesons produced should be about 1:1. Ref 5 finds this value. Finally, numerous calculations have been based on the hypothesis that the rho and omega are simple quark bound states, and have predicted reasonably accurate particle masses, decay rates, etc. Since the rho and omega both act like quark anti-quark bound states as far as predicting the behavior of other particles is concerned, and since the rho at least is known to be produced at rates consistent with its being produced by quark anti-quark fusion, I may conclude that the omega is also produced by quark anti-quark fusion. Note, however, that the most convincing evidence for this conclusion is based on data from experiments with relatively low center-of-mass energy: mostly from 4 to 6 GeV.

Second, my monte-carlo could be wrong, and the scaled data consequently distributed in some random fashion. This possibility I can partly test by looking at the relative cross sections of omega, phi, and J/psi. Unfortunately, the branching ratio for omega decaying to di-muons is not known. If I assume lepton universality, the branching ratio to two muons is, within errors, the same as for

decay to two electrons, namely (6.7 +/ Ø.4) E-5. If the omega decays similarly to the rho, with the branching ratio to two muons substantially greater than to two electrons, I find, using the rho decays as a guide, omega decays to two muons with a branching ratio of (9.8 +/- 1.9) E-5.

Since we did not well understand our beam or our live time, the numbers in Table 6-1 should not be used to try to calculate absolute cross-sections, only relative cross-sections.

Notice that when I assume the mesons are distributed with the "universal" Pperp distribution, and assume that the omega decays into two muons at the same rate as it does into two electrons, the phi to omega ratio is consistent with other measurements. See Tables 6-1 and 6-2.

There are not a great many measurements of the omega production cross-section, so it is hard to compare our ratio of J/psi to omega with results from other experiments; but if I compare our ratio to the ratio of the cross section of the J/psi to that of the rho, for a center of mass energy of about 6 GeV, the ratio is on the order of 1.4 E-4. Using the results of Ref 47 and 64 for production cross sections for rho and J/psi at a center-of-mass energy of about 2Ø GeV/c, I predict a ratio of about 3.Ø E-5 (12Ønb/4mb). I estimate the error as about +/- 1.Ø E-5 for the ratio of J/psis to omegas as produced by pions. Assuming the "universal" Pperp distribution and assuming that the branching ratio to two muons is the same as to two

electrons, I find that our ratio of J/psi to omega is 2.8 +/- Ø.5 E-5 for pion production and 5.5 +/- 1.2 E-5 for proton production. Using my own Pperp distributions (Section 6-1), I find 2.9 +/- Ø.6 E-5 and 5.6 +/- 1.2 E-5 instead. The pion-produced-meson ratio agrees surprisingly well with that predicted above.

The success of both tests, the phi to omega and the J/psi to omega total cross-section ratios, suggests that the monte-carlo is, apart from a scale factor, a good predictor of the actual acceptance.

Third, the parton distribution functions may be inappropriate. While some accurate measurements have been made of pion and proton valence quark distributions, the most accurate of these have been made at large Q**2 (25 (GeV/c)**2), though some go as low as 4.Ø (GeV/c)**2. For the omega and phi, the appropriate mass scale is Q**2 equal to Ø.61 and 1.Ø4. Attempting to use the Q-dependent corrections these experiments supply (Moriond) frequently results in nonsense, as these corrections were never meant to be used to extrapolate backwards. The gluon distribution functions have generally been predicted from sum rules rather than calculated from data, but some recent calculations (Ref 4Ø, 63) agree with the predictions.

The pion valence quark distributions from Daum and Kuhn are harder (in the sense of broader; containing a greater proportion of high XF quarks) than the Moriond distributions, and the TWOQ distributions are still harder. The trend seems real, and

Table 6-1

Acceptances for and Numbers Observed of
Omega, Phi, and J/psi Mesons

beam	acceptance for	omega	phi	J/psi
pion	A	.0064	.016	.033
	B	.0063	.023	
proton	A	.0082	.028	.055
	B	.0081	.030	

	number seen	omega	phi	J/psi
pion		2340 +/- 66	1729 +/- 83	383 +/- 24
proton		400 +/- 30	580 +/- 73	186 +/- 8

The acceptances calculated using my values for the coefficient "C" of exp(-C*Pperp**2) are called the "A-acceptances." Those calculated using C = 3.1 (GeV/c)**-2 are called the "B-acceptances."

Table 6-2

Ratio of Phi to Omega Production
Cross Section

A

Beam	e=mu	Scaled
Pion	.080 +/- .012	.118 +/- .028
Proton	.112 +/- .022	.164 +/- .044

B

Beam	e=mu	Scaled
Pion	.055 +/- .008	.080 +/- .019
Proton	.105 +/- .021	.154 +/- .042

Both tables assume a gaussian distribution of perpendicular momentum. The "A" table uses my calculated parameterization of the perpendicular momentum (see Section 6-1); while the "B" table uses the "universal" 3.1 coefficient.

I include two possible assumptions for the omega's branching ratio into two muons: The branching ratio may be equal to that for decay into two electrons (e=mu = 6.7 E-5), or the ratio may be equal to that for decay into two electrons times a factor given by the branching ratio for the rho into two muons divided by the branching ratio for the rho into two electrons (Scaled = 9.8E-5).

reasonable. Gluon distributions are supposed to become softer with increasing Q**2, but these are not yet very well understood, especially for pions. The gluon distributions are generally consistent with the simple counting rule predictions, so I assume minimal variation.

Fourth, the fit could be accidental, due to a bad point or two. In order to verify that the fit for pion-produced omegas is good, I repeated the fit six additional times, each time removing a different data point, using the Daum distributions. I tabulate the results below. Where the difference between the chi-squared and maximum-likelihood fit parameters exceeded the nominal error, I used the difference between the fit parameters as an estimate of the error.

The agreement is good, and I conclude that the fit is reasonable.

Fifth, the naive parton fusion model could be inappropriate at this mass scale. Although the model has been widely and usually successfully applied at mass scales of 2-3 GeV/c**2, it is not theoretically supposed to be very good below a mass scale of about 4 or 5 GeV/c**2. The model has to break down somewhere; apparently it breaks down at a scale greater than the omega mass. If I regard the fit to the pion-produced phi data as good, it would indicate that about 80% of all the phis produced by pions are produced by fusing

Table 6-3

The ratio of quark fusion to gluon fusion for chi-squared (chi) and maximum likelihood (max) fits, dropping points from the fit.

XF interval excluded	Type of fit	ch2/DF	Ratio
none	chi	1.39	0.47 +/- 0.12
	max	1.52	0.54 +/- 0.13
(0.1,0.2)	chi	1.82	0.65 +/- 0.45
	max	2.26	1.55 +/- 0.95
(0.2,0.3)	chi	0.85	0.14 +/- 0.22
	max	1.34	0.49 +/- 0.37
(0.3,0.4)	chi	1.52	0.53 +/- 0.17
	max	1.72	0.49 +/- 0.14
(0.4,0.5)	chi	0.93	0.30 +/- 0.13
	max	1.24	0.39 +/- 0.13
(0.5,0.6)	chi	0.59	2.24 +/- 2.41
	max	0.99	0.70 +/- 0.54
(0.6,0.7)	chi	1.82	0.39 +/- 0.09
	max	1.89	0.40 +/- 0.09

strange quarks from the sea: a result contradicted by experiments which have sought the left-over strange quarks. If my fit is good, the theory is also bad for mass scales of the order of the phi.

On the other hand, the "fireball model" (See Chapter 2) describes the data fairly well for intermediate XF. The fit has a chi-squared per degree of freedom of 5.3/3, and suggests an effective temperature of 1.34 +/- Ø.Ø3 El3 degrees Kelvin, or 1.15 +/- Ø.Ø2 GeV/c**2.

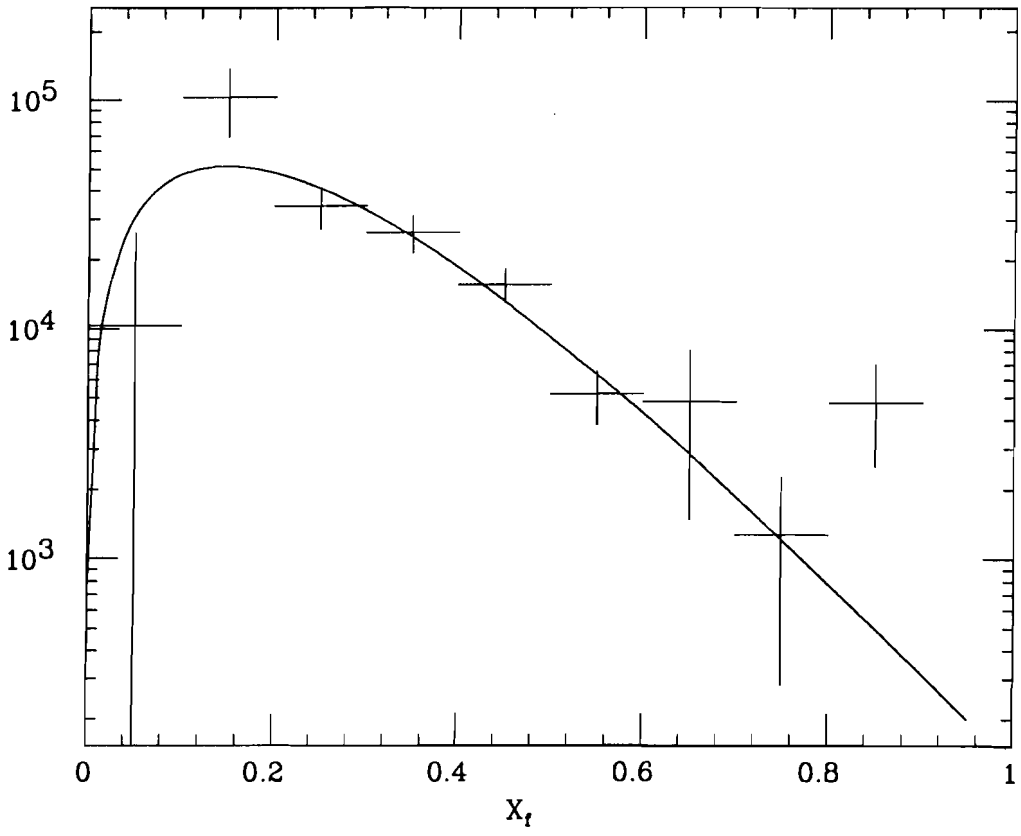

Figure 6-4

Fireball model fit to omega data
beta = 1/kT = 0.867 +/- 0.018

Appendix A

Minor Projects

2.1 Overview

I believe that I should not only report on what I found in my work, but what I was unable to find as well. Besides the thesis topic, I studied the rest of the mu+ mu- and mu+ mu- gamma spectrum to see if there was evidence for particles decaying to these states. In particular, I looked for a DØ signal, an eta-c signal, and anything decaying radiatively to the omega or phi.

To begin with, I looked for evidence for the eta(958) in either its mu+ mu- gamma channel or its omega gamma channel. Neither was seen: a fact that should not be too surprising in view of our extremely low acceptance for either. Further, there is no clear evidence for any other radiative decay to the omega in our data. Perhaps with better statistics something might appear, but for now: nothing. (Figure A-1)

Secondly, I looked for radiative decays to the phi. There is nothing convincing to be seen. In unpublished work by Dr. Paul Schoessow, he examined the phi gamma spectrum. His phi came from K+ K- events, and had a signal/noise of 1:1. Ours has a signal/ noise

of 1:4.5 . He saw nothing convincing either. (Figure A-2)

Thirdly, I looked for electromagnetic decays of the neutral charmed meson DØ. I have succeeded in putting limits on the decay DØ --> mu+ mu-. The theoretical limit is far lower, but I find no experimental limits on this decay in the literature. I describe this in detail in section A-2. (Figure A-3)

2.2 DØ

The formula of Shrock and Volosin (Ref 69), modified to describe the decay of the DØ to two muons, is

$$Br(D^0 \to \mu\mu) = \frac{G_F^2}{2\pi^4} \frac{(1-4m_\mu^2/m_D^2)^{\frac{1}{2}}}{(1-m_\mu^2/m_D^2)^2} \cdot Br(D^+ \to \mu^+ \nu_\mu) \cdot \frac{\tau(D^0)}{\tau(D^+)} \cdot \frac{1}{|V_{cd}|^2} \left(\sum_{i=d,s,b} m_i^2 \, Re(V_{ic}^* V_{iu}) \right)$$

$$\leq \frac{G_F^2}{2\pi^4} \frac{(1-4m_\mu^2/m_D^2)^{\frac{1}{2}}}{(1-m_\mu^2/m_D^2)^2} \frac{\tau(D^0)}{\tau(D^+)} \frac{Br(D^+ \to \mu\nu)}{|V_{cd}|^2} \left(\sum_{i=d,s,b} m_i^2 |V_{ic} V_{iu}| \right)^2$$

The mass ratio term is equal to Ø.997. The ratio of lifetimes is equal to Ø.478 +/- Ø.124 (Ref 73). The branching ratio of the D+ to a muon and neutrino is (Ref 73) less than Ø.Ø2. The constant term is about 5.336 E-13. Now all that remains is the factor involving the KM matrix elements. Using the numbers from Ref 73 and Ref 19 for the elements of the KM matrix, using the 4-angle parameterization of Kobayashi and Maskawa, I find the term involving the matrix elements varies from .133 to .137. Thus I find the branching fraction to be limited by:

Br(DØ --> mu+ mu-) < 6.9 +/- 1.8 E-16

In order to calculate the branching ratio for DØ from our data, I

calculate the ratio

$$Br_D = \frac{N_D}{N_\psi} \frac{\sigma_\psi Br_\psi}{\sigma_D} \frac{Ac_\psi}{Ac_D}$$

where the numbers of events are found from the data, the acceptances are calculated from the monte-carlo, and the cross sections are taken from Ref 10 and Ref 11 for the DØ and J/psi respectively. For pion beam, our DØ acceptance was Ø.14, and for the proton beam, our acceptance was Ø.16, with errors less than 1%. For the J/psi, our acceptance for the pion data was Ø.12 and for the proton data it was Ø.16.

In pion data, I find 110 +/- 150 (< 310 at 90% cl.) events in a peak at the DØ mass, and in proton data I find Ø +/- 76 (< 99 at 90% cl.) events. I find, assuming the cross section times the branching ratio for J/psi production is 8.88 +/- 1.44 nb (.074 * 120nb):

σ_{D^0}Br(DØ --> mu+ mu-) = 2.1 +/- 2.9 nb < 6.1nb (90% cl.)

Bailey et al (Ref 10) find a cross section from DØ (200 GeV/c pions) of 48 +/- 15 +/- 24 microbarns. This sets a limit of 1.4E-4 on the branching ratio of DØ into two muons, at the 90% confidence level, or a measurement of 4.4 +/- 7.0 E-5. If I assume that the branching fraction of DØ into two muons is simply the branching ratio of DØ into an electron plus anything, times the spin suppression factor (M(mu)/M(DØ))**2 , I can predict that the branching fraction for DØ into two muons must be less than 1.7 E-4. My limit on this branching fraction is lower than this naive prediction, but still far above

that of the canonical theory.

If the DØ had a substantial branching ratio into two muons, it would show up in e+ e- colliders as an enhancement of the ratio of hadrons to leptons at the DØ mass. Nothing was noticed by Grilli et al at Frascati (Ref 43), and no DØ was noticed by Cosme et al (Ref 26) in a more detailed study of the same region.

2.3 Eta-c

Unfortunately, the eta-c region is swamped by the J/psi. (Figure A-4) If one spark is mischosen for one of the muon tracks making up a J/psi, the J/psi mass can be as much as 1ØØ MeV wrong.

I cannot say with confidence that there is a signal present, though there is a slight enhancement. In the pion-produced di-muon data, MINUIT finds 17 +/- 11 eta-c events, which is less than 31 events at the 9Ø confidence level. This corresponds to a measurement for the cross section for eta-c times its branching ratio into di-muons of Ø.39 +/- Ø.26 nb, or a limit of .73nb at the 9Ø% confidence level.

In the di-muon plus gamma mass plot, MINUIT finds 26 +/- 16 J/psi events and 11 +/- 18 eta-c events, corresponding to limits of 47 and 34 events respectively at the 9Ø% confidence level. For the J/psi this corresponds to a measurement of the branching ratio to two muons and a photon of 2.5 +/- 1.6 %, or less than 4.6%. For the eta-c, this corresponds to a measurement of the cross section times

the branching ratio to two muons and a photon of 1.2 +/- 1.9 nb, or less than 3.7nb.

2.4 General

I invite the reader to compare the di-muon spectrum with the di-muon plus gamma spectrum. Figures 1-1 and 1-2 show the di-muon spectrum, Figure A-5 shows the (pion-produced) di-muon plus gamma spectrum, A background was calculated for the di-muon spectrum by combining positive muons from one event with negative muons from another. When this background is subtracted, one has Figure A-6. For di-muon plus photon events, a background was calculated by combining di-muons from one event with photons from another. When this background is subtracted, one has Figure A-7.

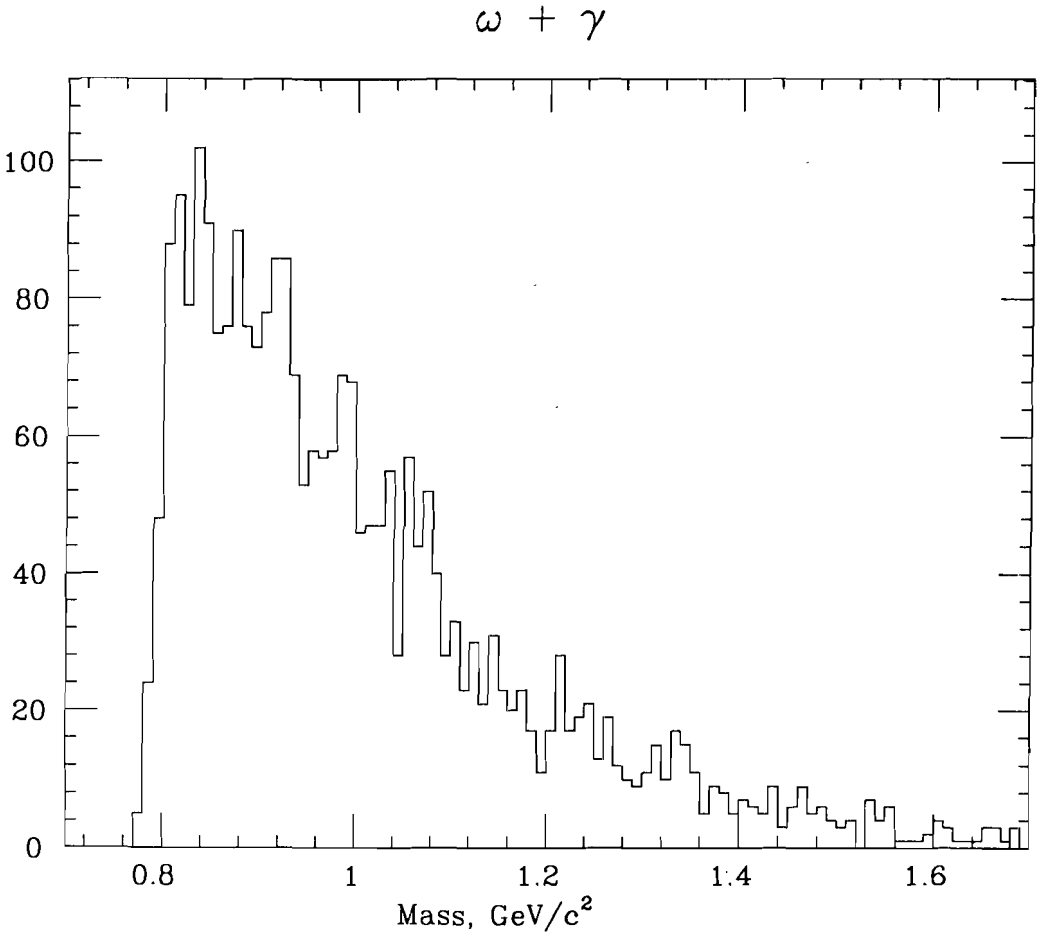

Figure A-1

Omega plus gamma masses

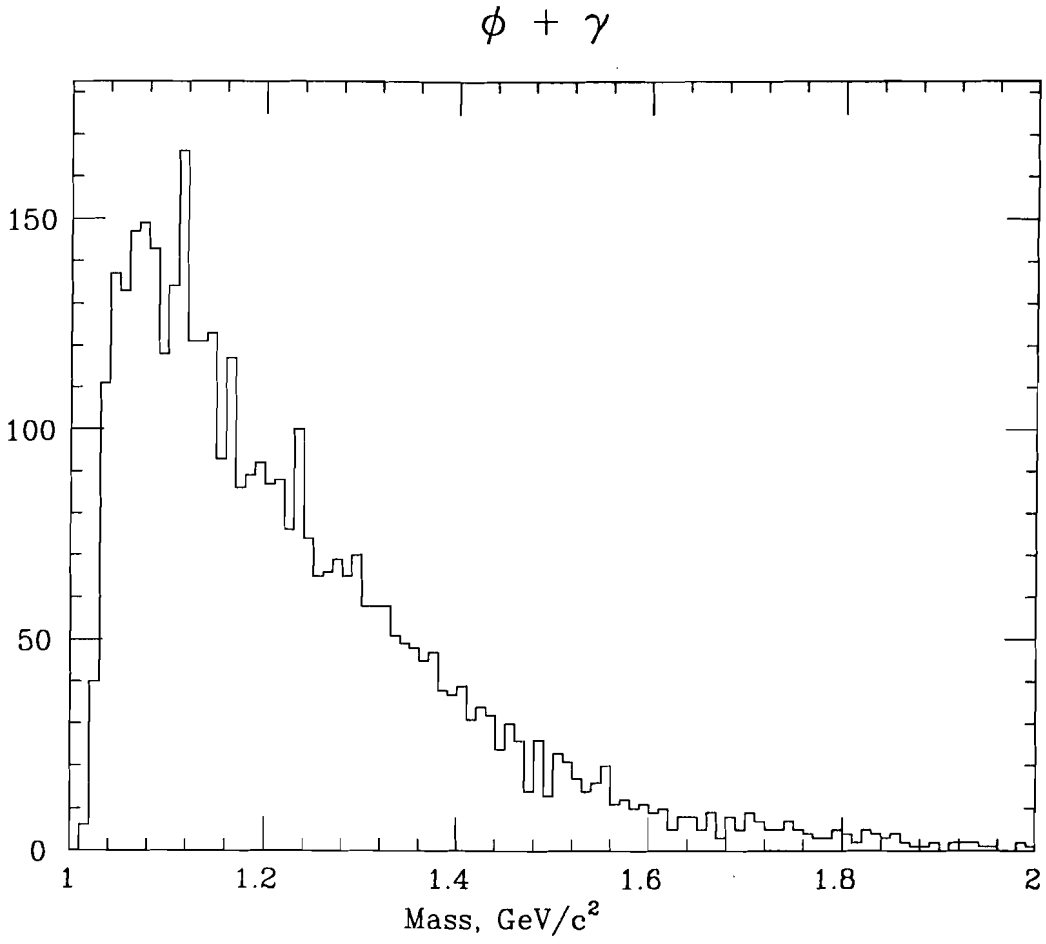

Figure A-2

Phi plus gamma masses

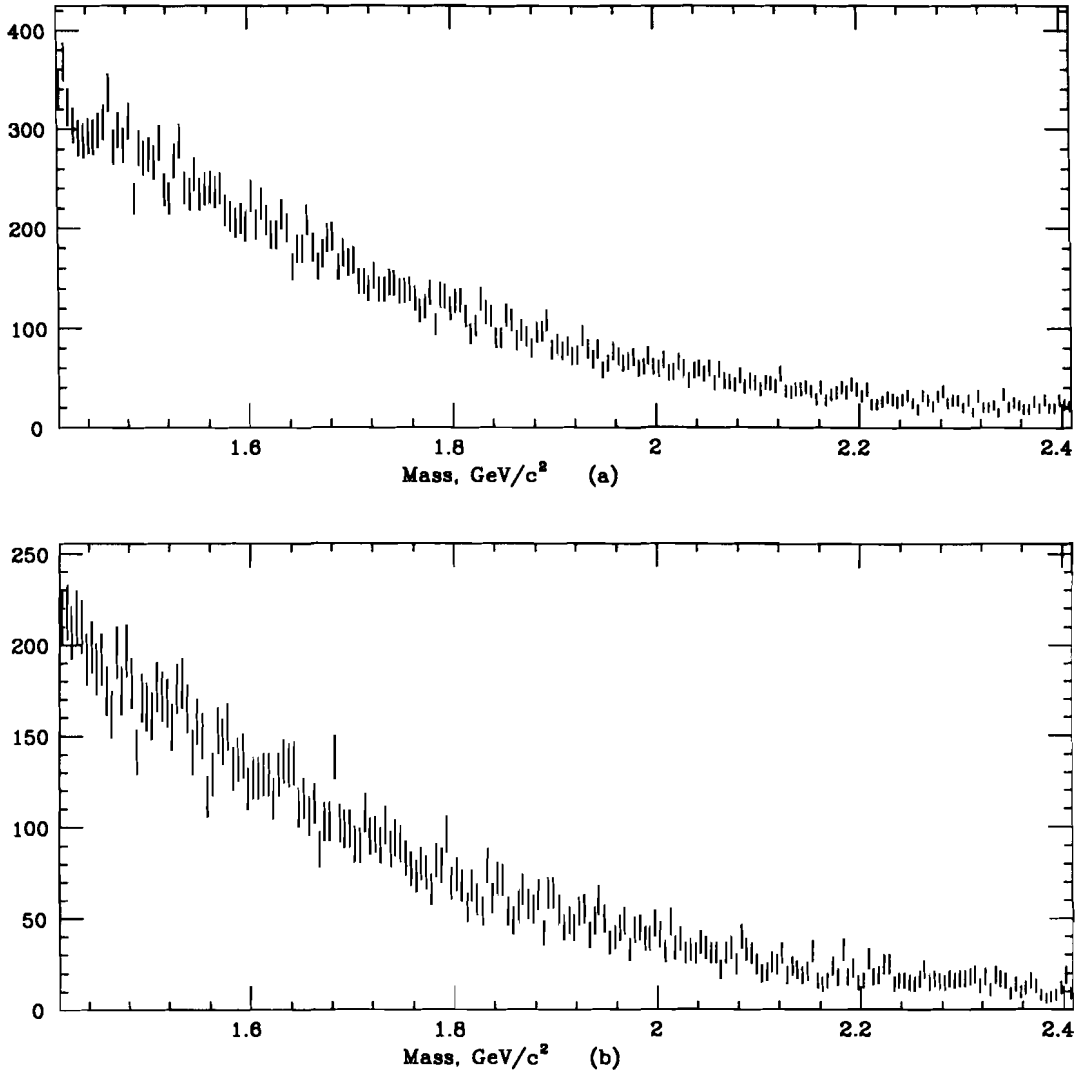

Figure A-3

Di-muon spectrum near DØ region
a) pion induced
b) proton induced

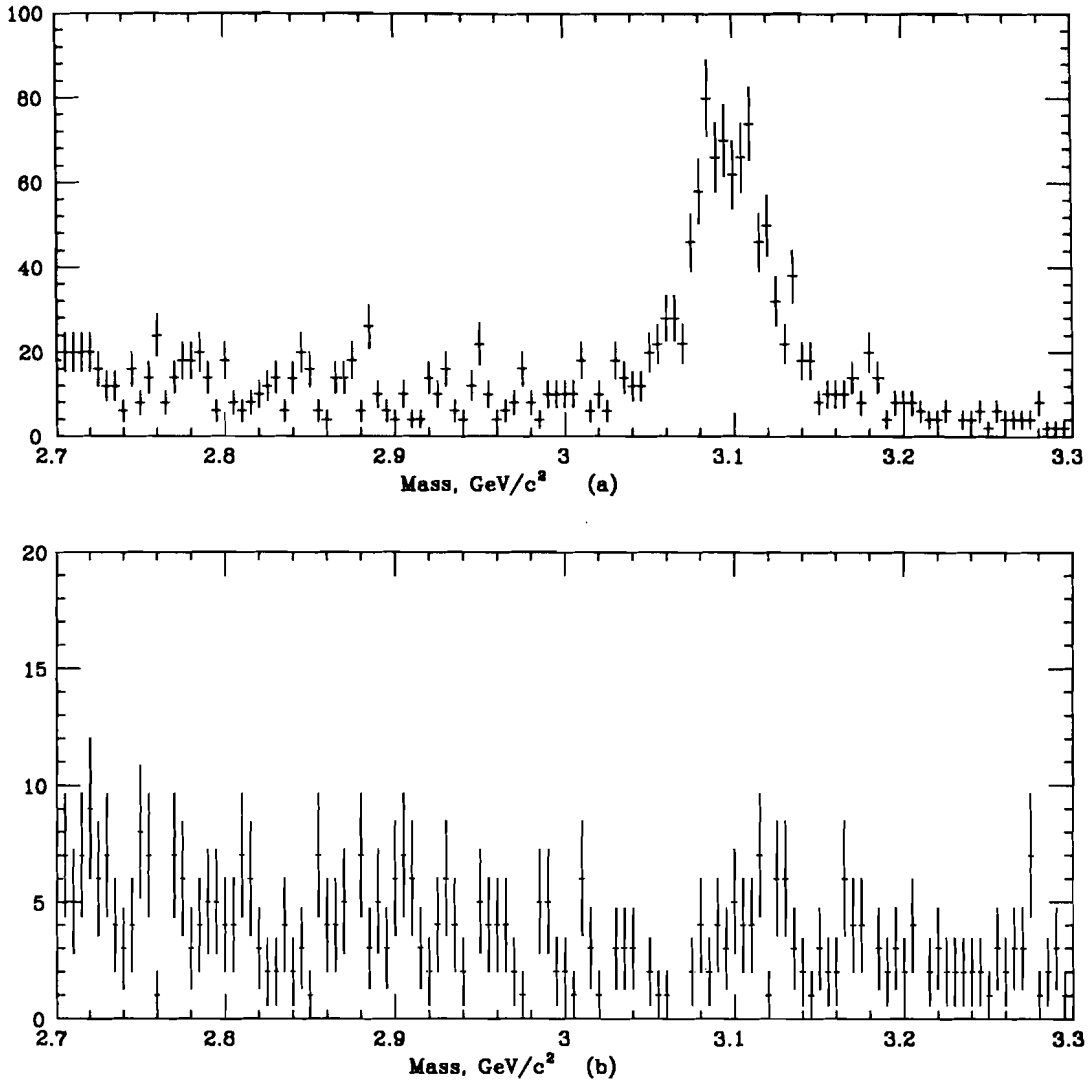

Figure A-4

J/psi and eta-c region
a) di-muon
b) di-muon + photon

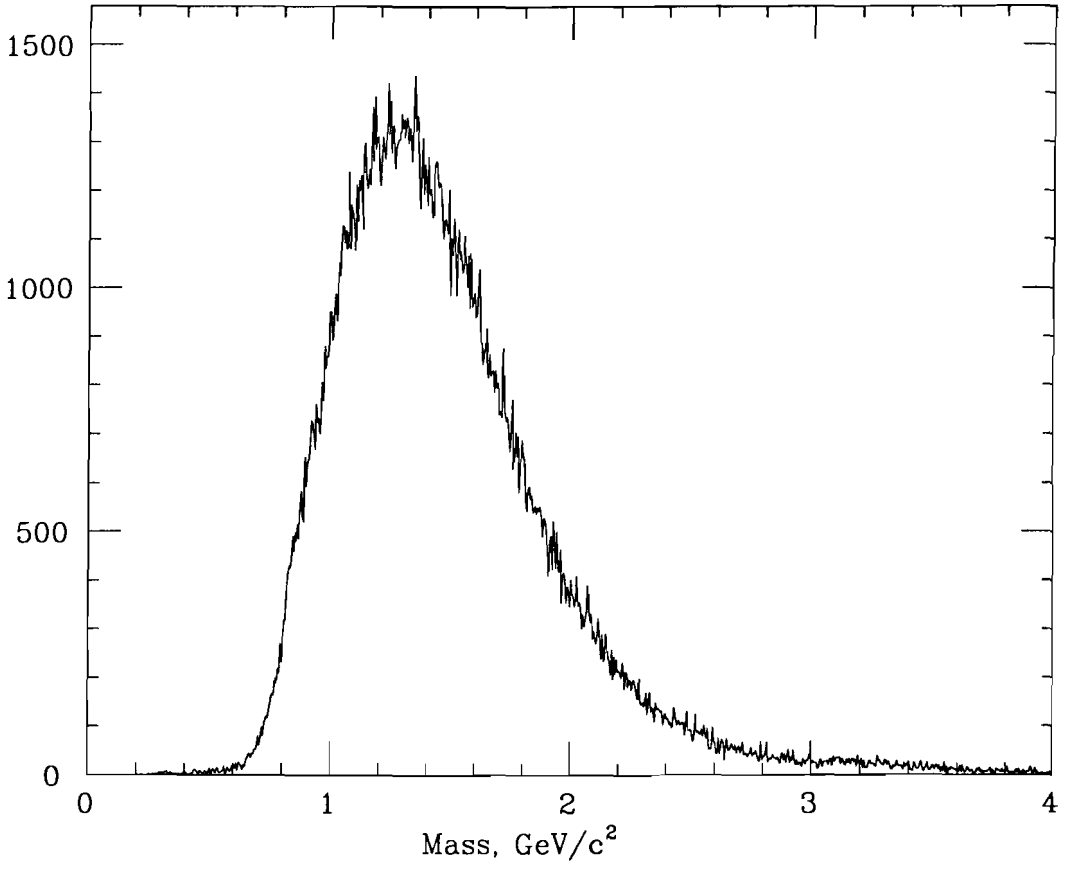

Figure A-5

Pion-produced mu+ mu- gamma masses

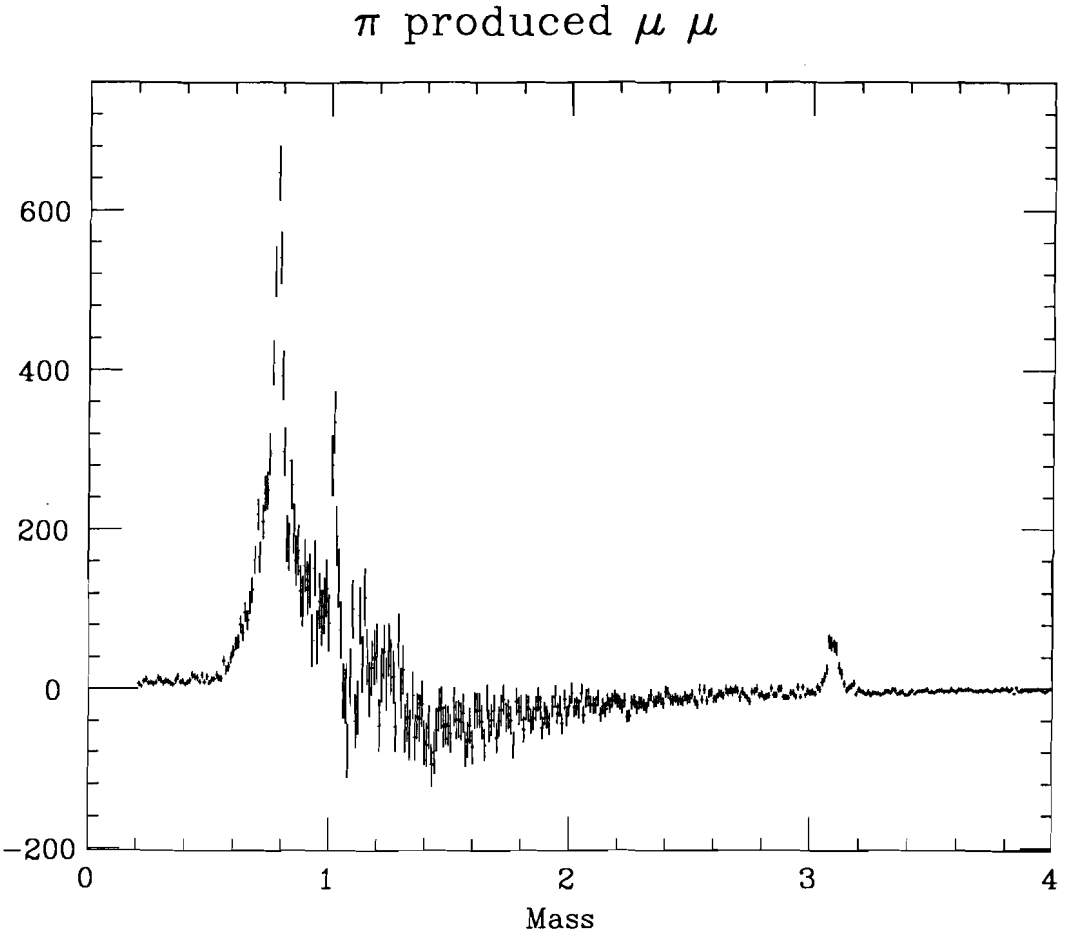

Figure A-6

Background subtracted di-muon spectrum
(pion data)

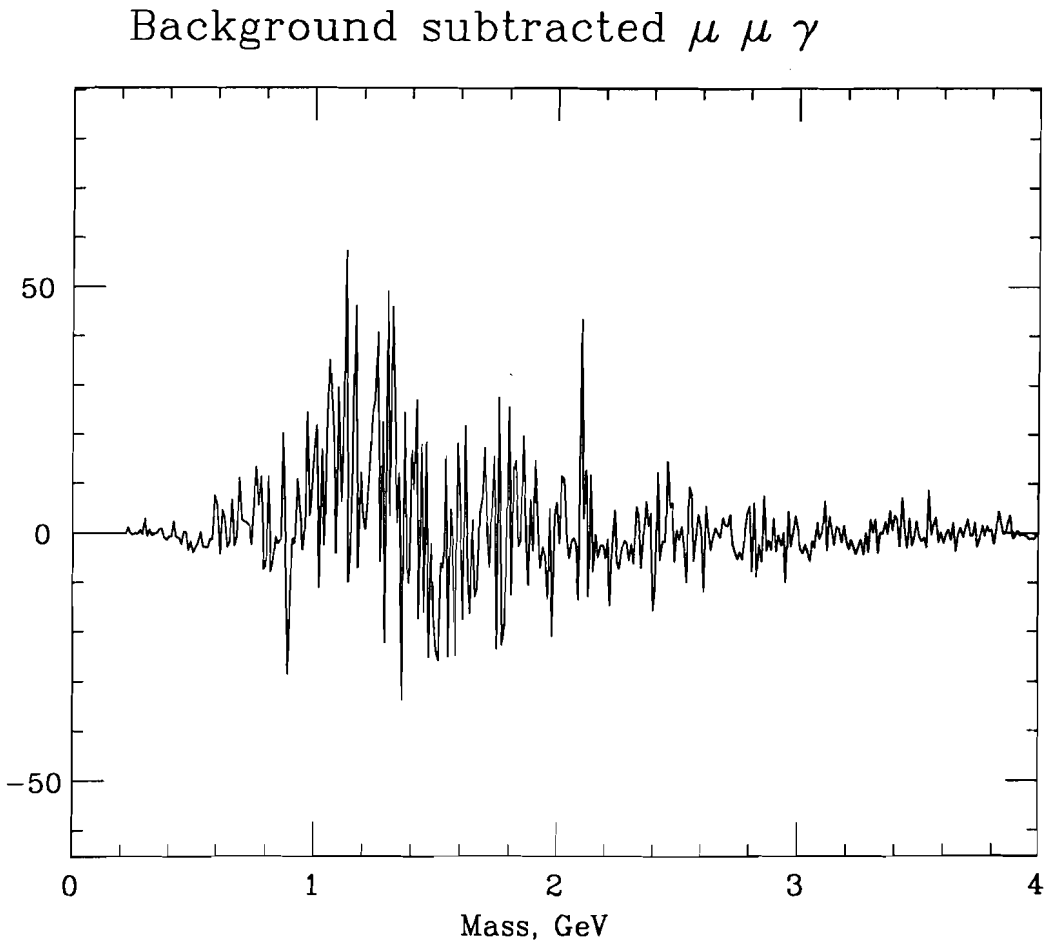

Figure A-7

Background subtracted mu+ mu- gamma spectrum (pion data)

Appendix B

Mass Plots

These are the rest of the mass plots. Figure B-1 shows the mass plots near the phi meson mass with pion-produced di-muons in different XF intervals. Figure B-2 shows the mass plots for the pion-produced di-muons near the phi mass in different Pperp intervals. Figure B-3 and B-4 are the same for the proton-produced di-muons, respectively, and Figures B-5 and B-6 are the same for the proton-produced omegas.

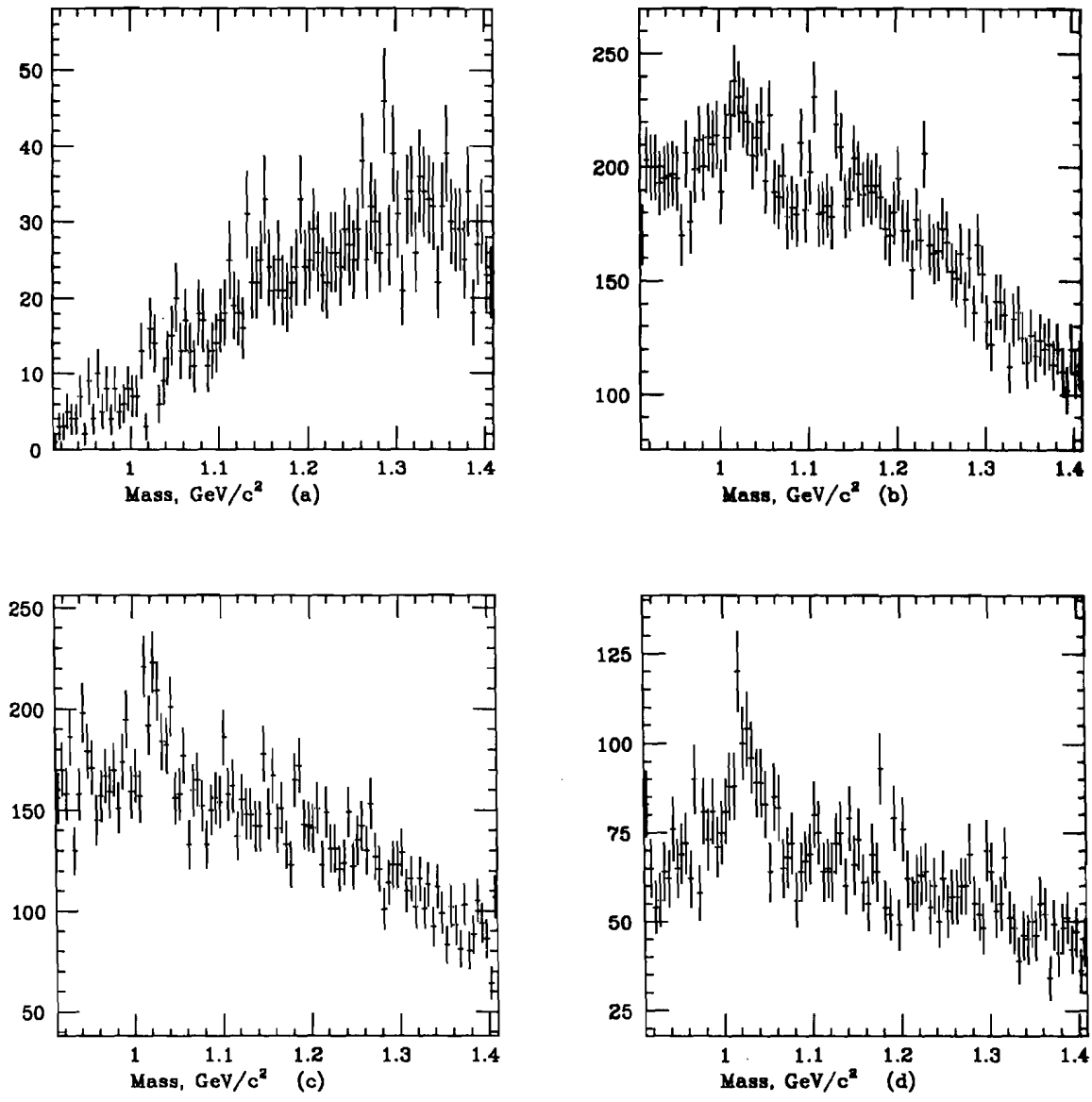

Figure B-1

Di-muon production for Pperp < 1.0
Pion-produced
5 MeV bins
a) 0.0 < XF < 0.1
b) 0.1 < XF < 0.2
c) 0.2 < XF < 0.3
d) 0.3 < XF < 0.4

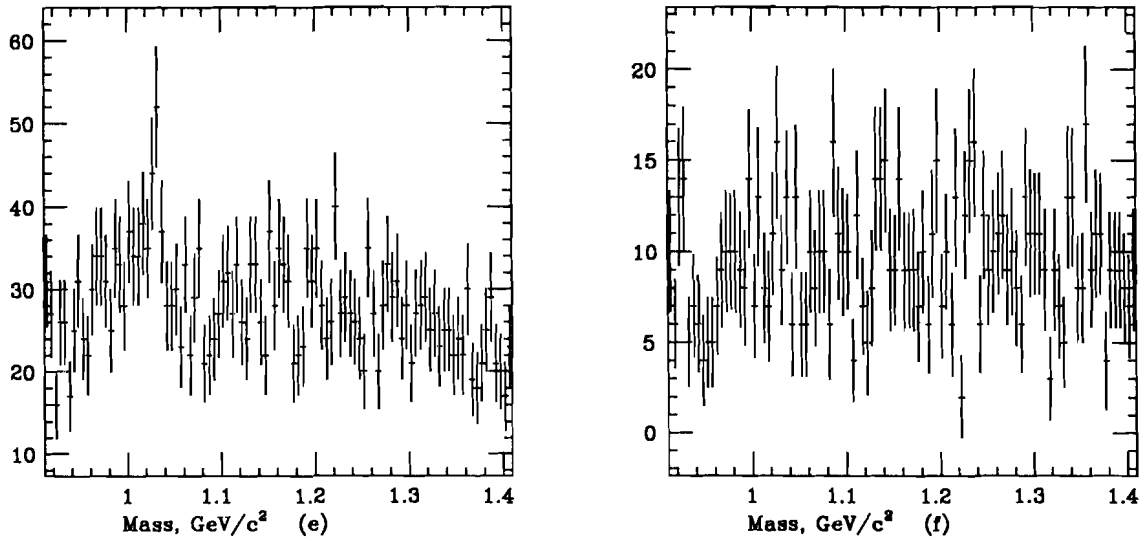

Figure B-1
(continued)
Di-muon production for Pperp < 1.0
Pion-produced
5 MeV bins
e) 0.4 < XF < 0.5
f) 0.5 < XF < 1.0

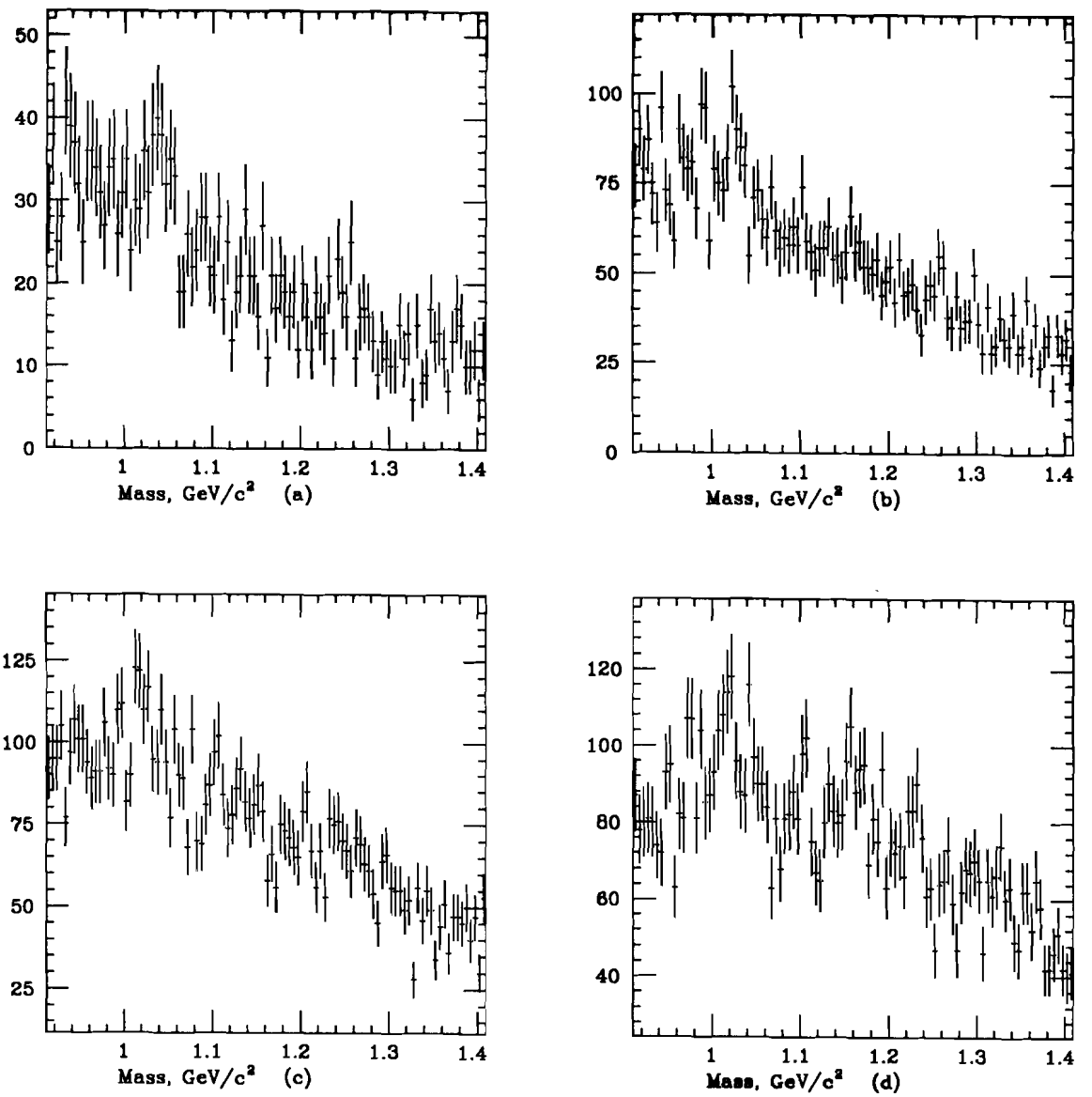

Figure B-2

Di-muon production for 0.0 < XF < 1.0
Pion-produced
5 MeV bins
a) 0.0 < Pperp < 0.1
b) 0.1 < Pperp < 0.2
c) 0.2 < Pperp < 0.3
d) 0.3 < Pperp < 0.4

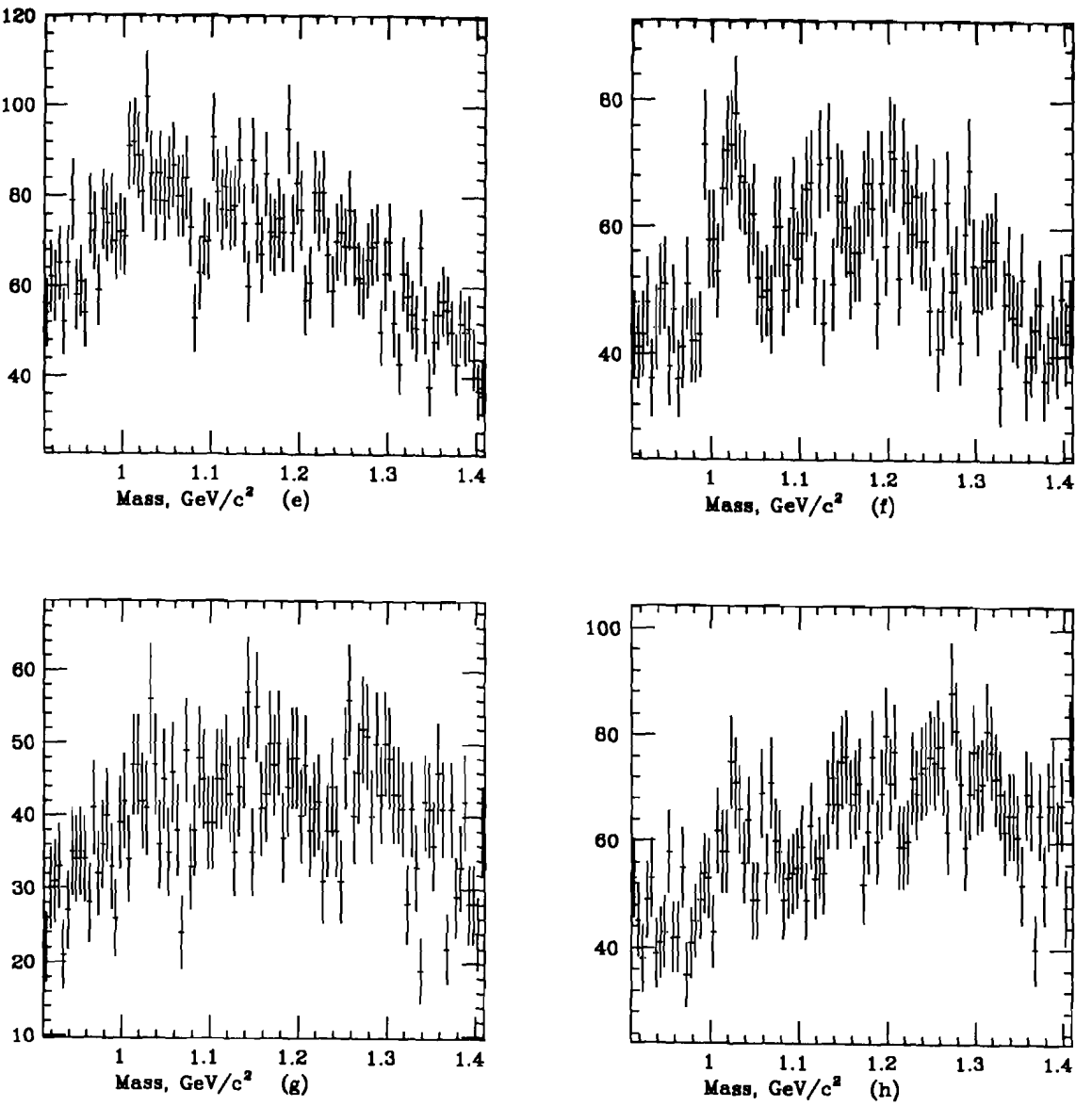

Figure B-2
(continued)
Di-muon production for 0.0 < XF < 1.0
Pion-produced
5 MeV bins
e) 0.4 < Pperp < 0.5
f) 0.5 < Pperp < 0.6
g) 0.6 < Pperp < 0.7
h) 0.7 < Pperp < 1.0

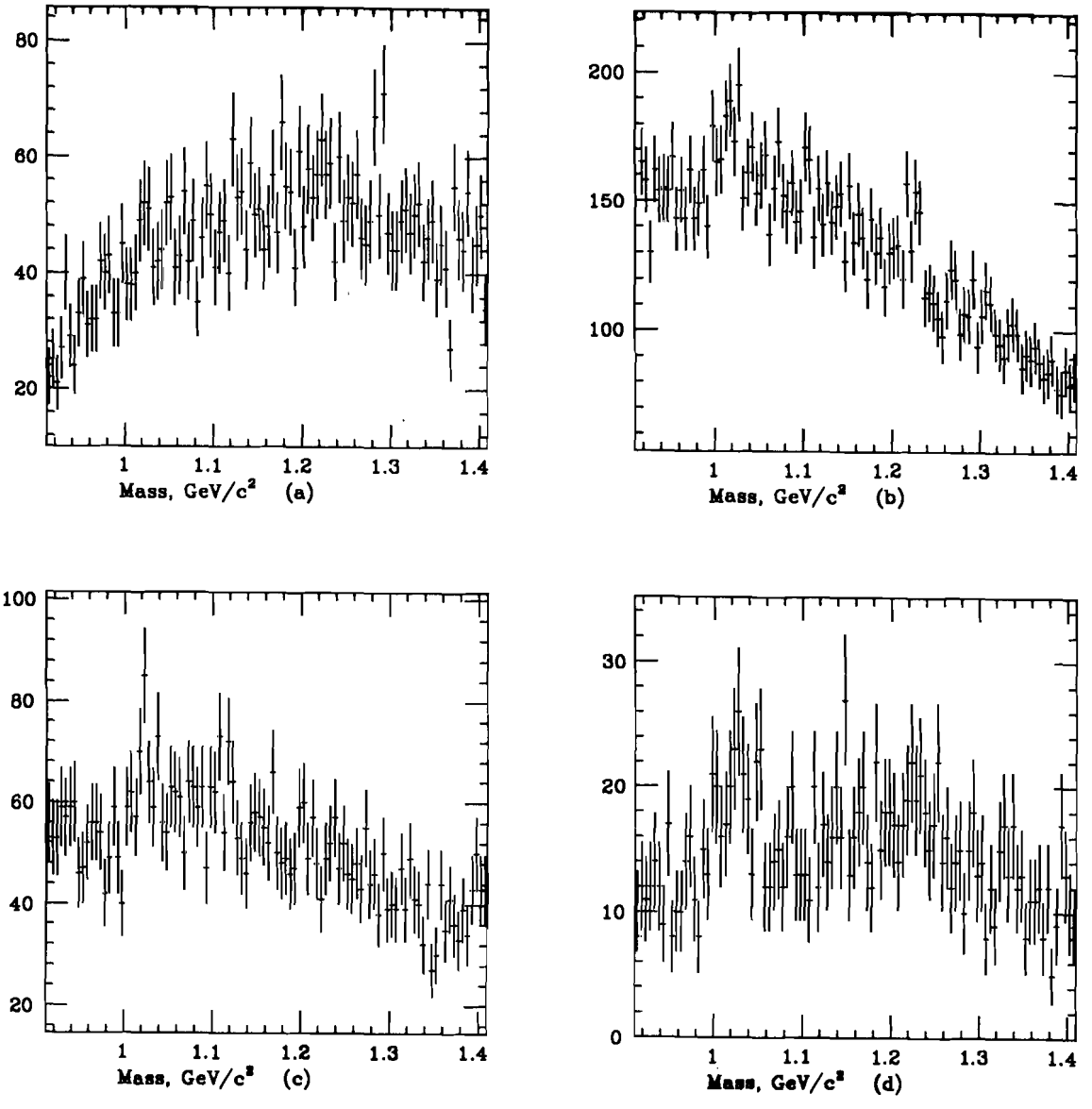

Figure B-3

Di-muon production for Pperp < 1.0
Proton-produced
5 MeV bins
a) 0.0 < XF < 0.1
b) 0.1 < XF < 0.2
c) 0.2 < XF < 0.3
d) 0.3 < XF < 0.4

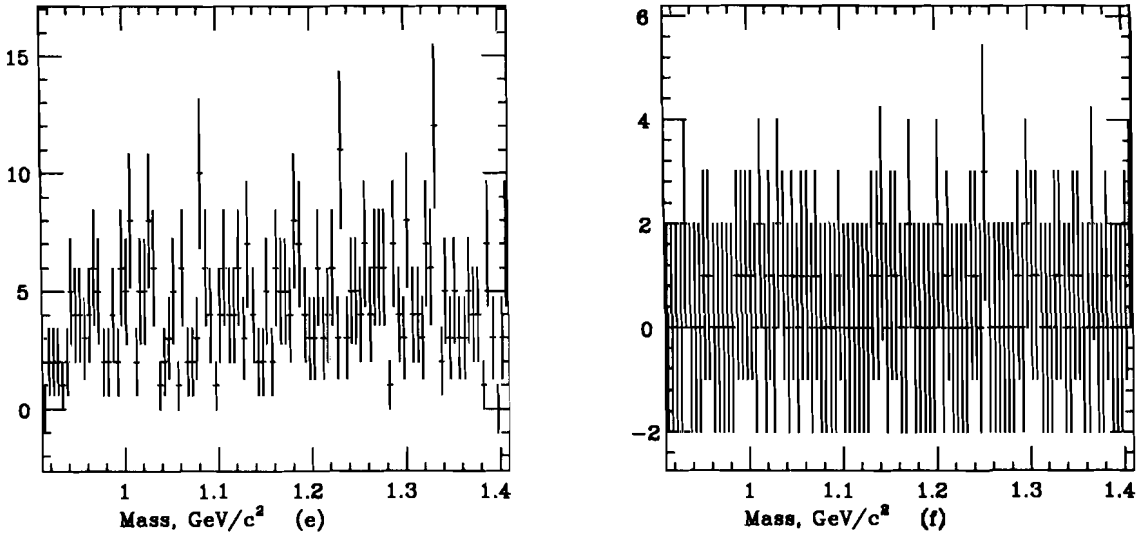

Figure B-3
(continued)
Di-muon production for Pperp < 1.0
Proton-produced
5 MeV bins
e) 0.4 < XF < 0.5
f) 0.5 < XF < 1.0

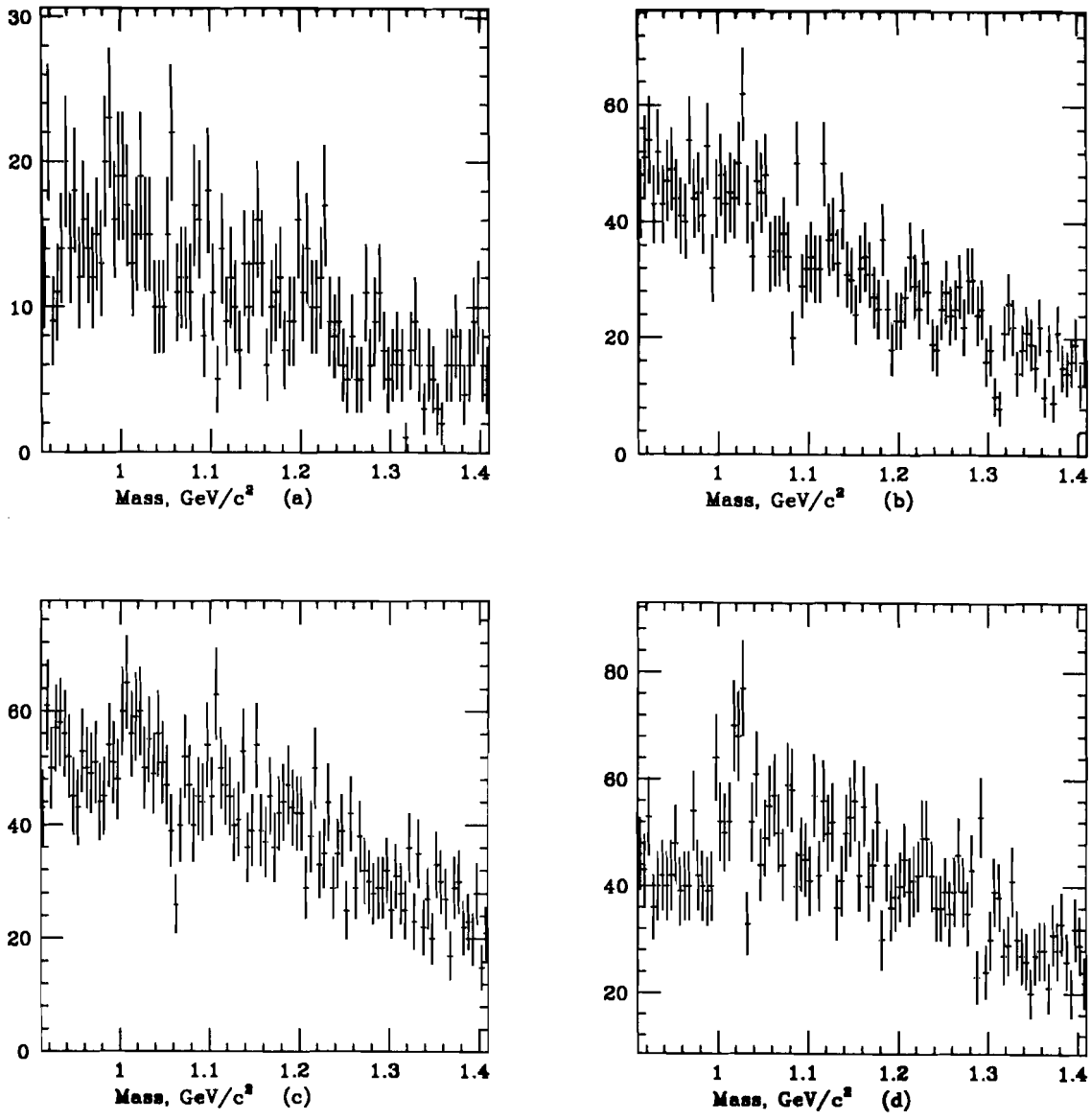

Figure B-4

Di-muon production for 0.0 < XF < 1.0
Proton-produced
5 MeV bins
a) 0.0 < Pperp < 0.1
b) 0.1 < Pperp < 0.2
c) 0.2 < Pperp < 0.3
d) 0.3 < Pperp < 0.4

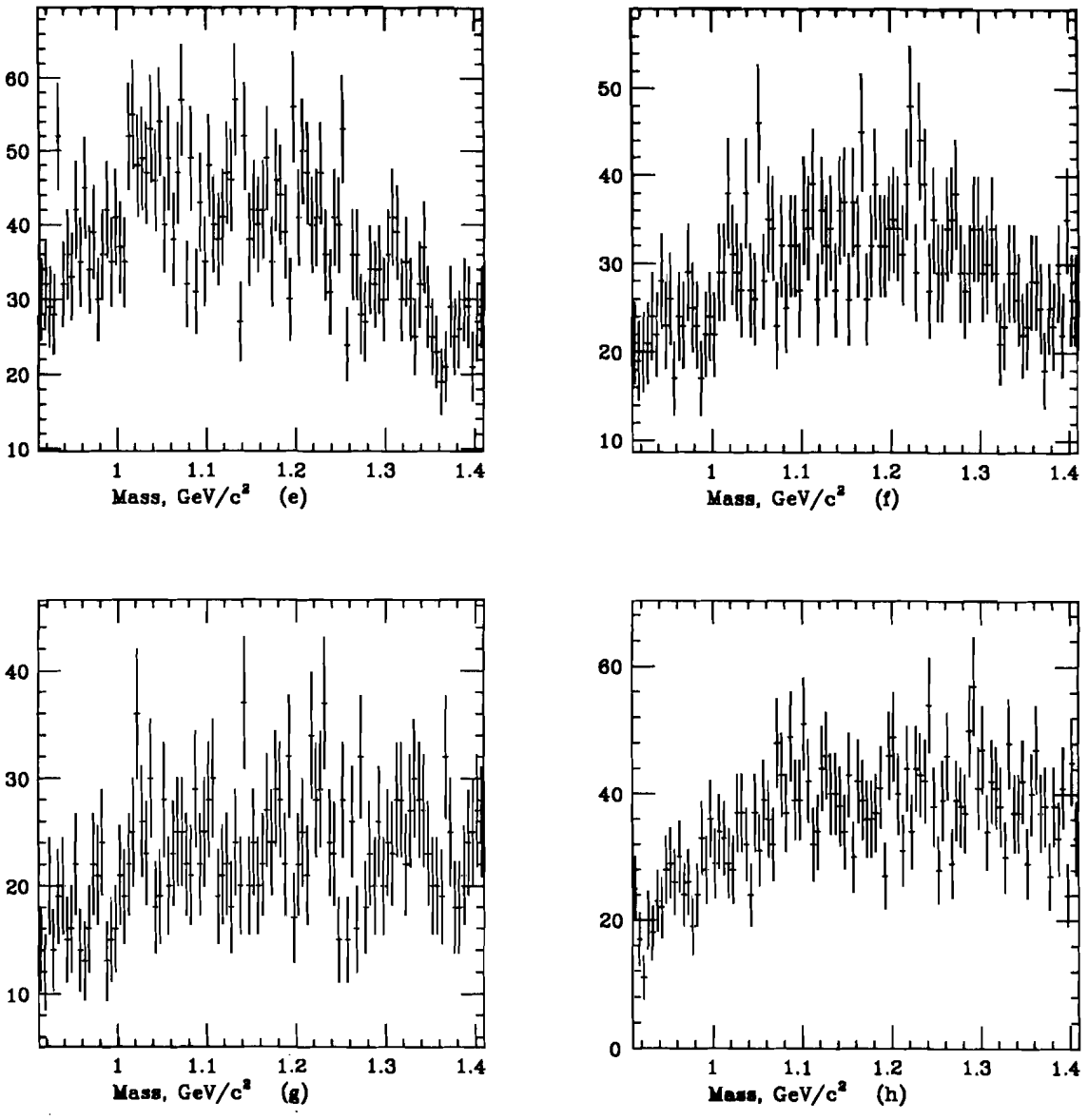

Figure B-4
(continued)
Di-muon production for 0.0 < XF < 1.0
Proton-produced
5 MeV bins
e) 0.4 < Pperp < 0.5
f) 0.5 < Pperp < 0.6
g) 0.6 < Pperp < 0.7
h) 0.7 < Pperp < 1.0

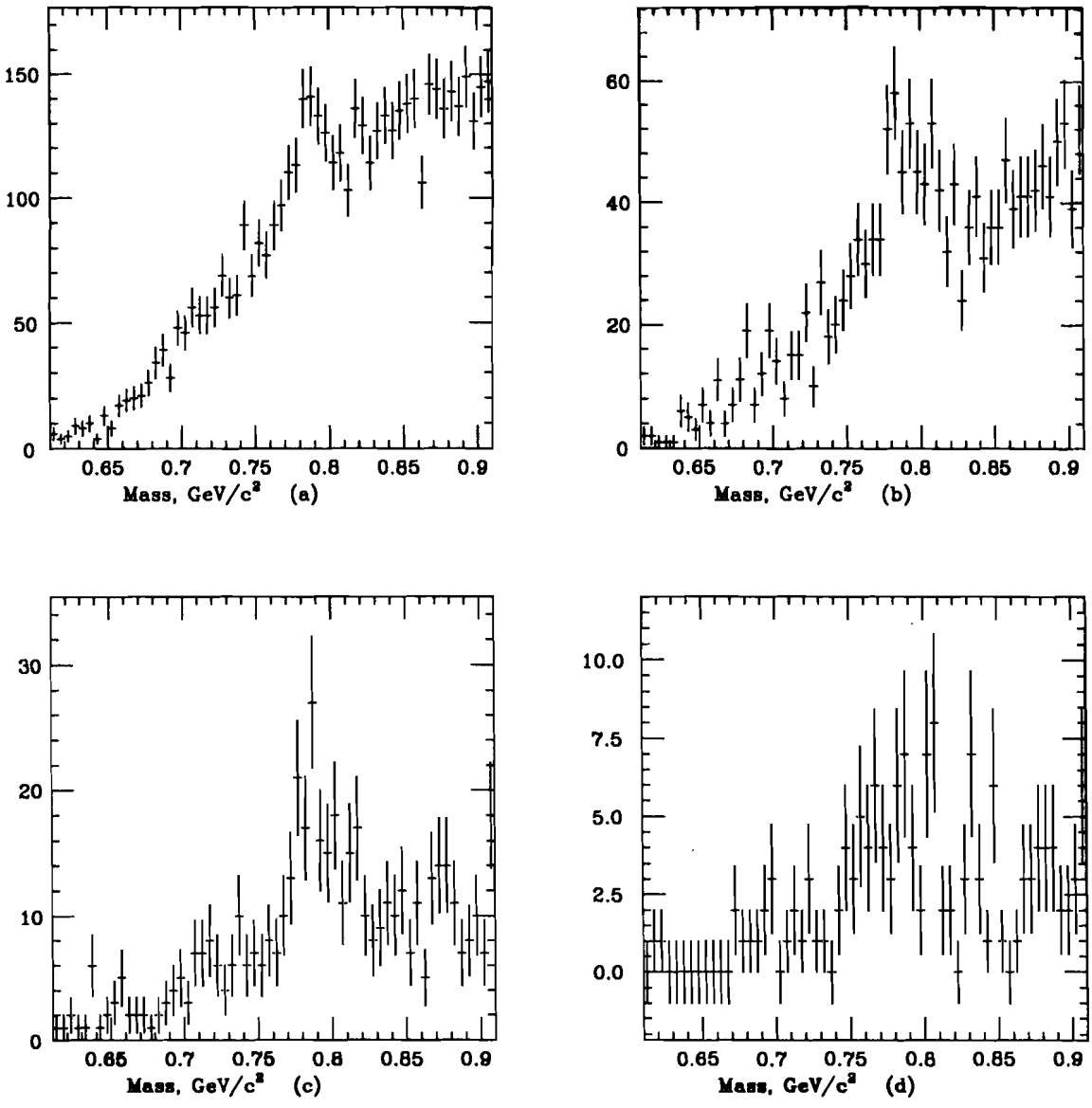

Figure B-5

Di-muon production for Pperp < 1.0
Proton-produced
5 MeV bins
a) 0.1 < XF < 0.2
b) 0.2 < XF < 0.3
c) 0.3 < XF < 0.4
d) 0.4 < XF < 0.5

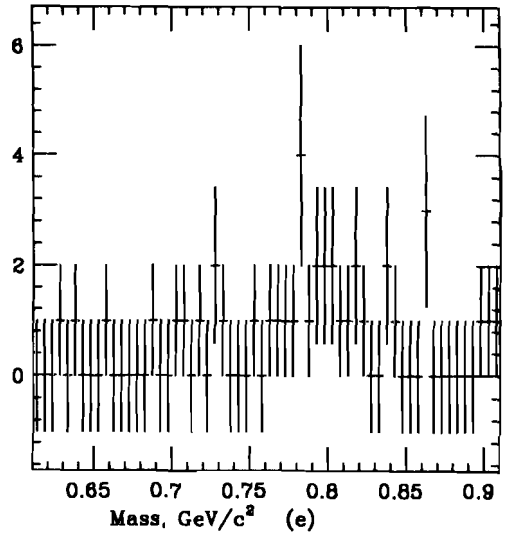

Figure B-5
(continued)
Di-muon production for Pperp < 1.Ø
Proton-produced
5 MeV bins
e) Ø.5 < XF < 1.Ø

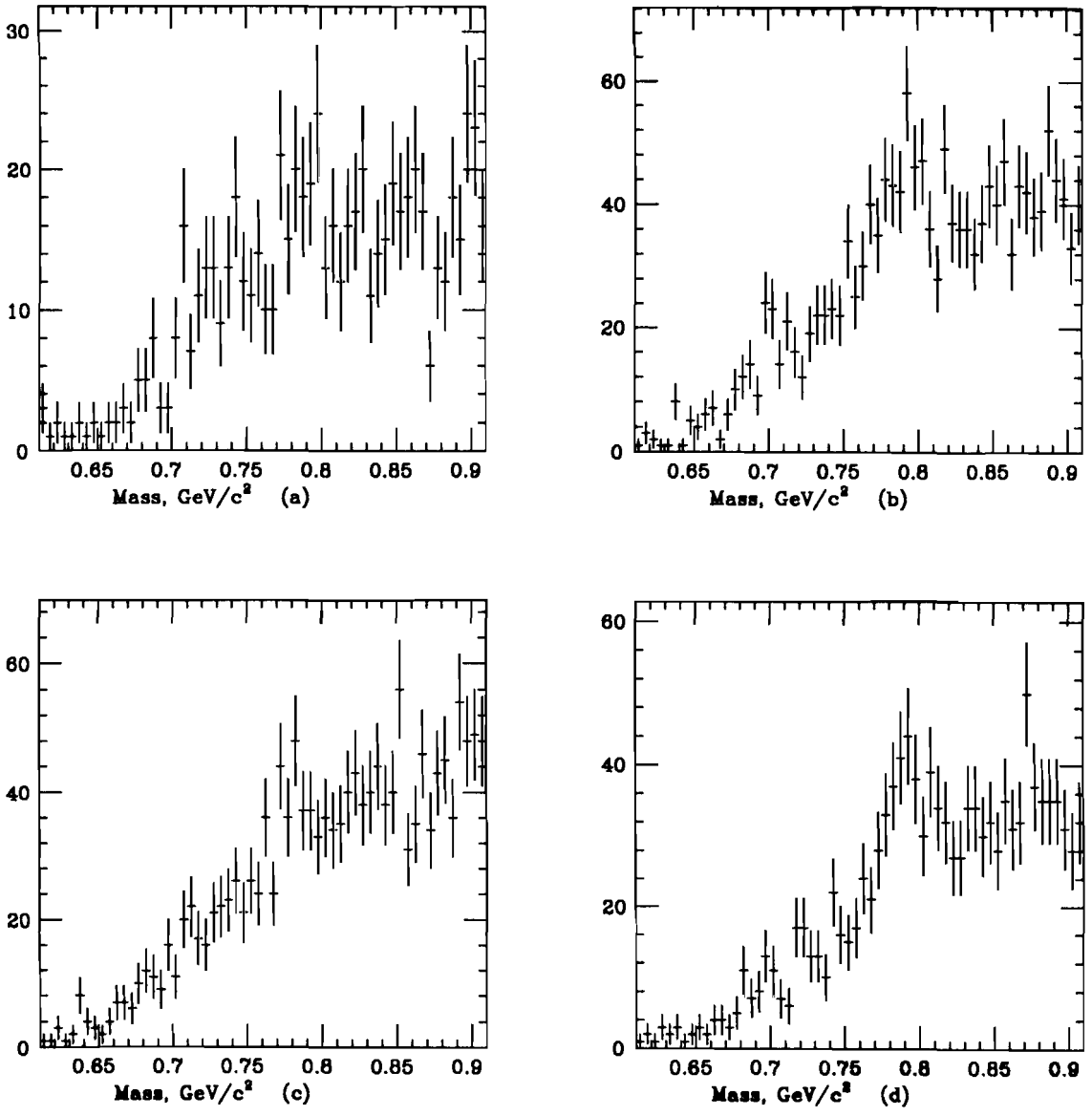

Figure B-6

Di-muon production for 0.0 < XF < 1.0
Proton-produced
5 MeV bins
a) 0.0 < Pperp < 0.1
b) 0.1 < Pperp < 0.2
c) 0.2 < Pperp < 0.3
d) 0.3 < Pperp < 0.4

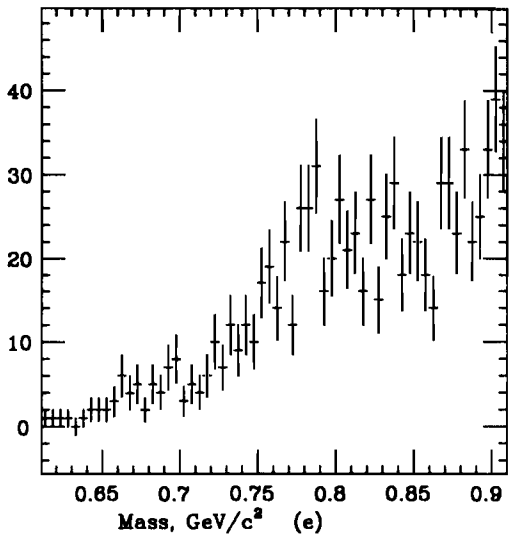

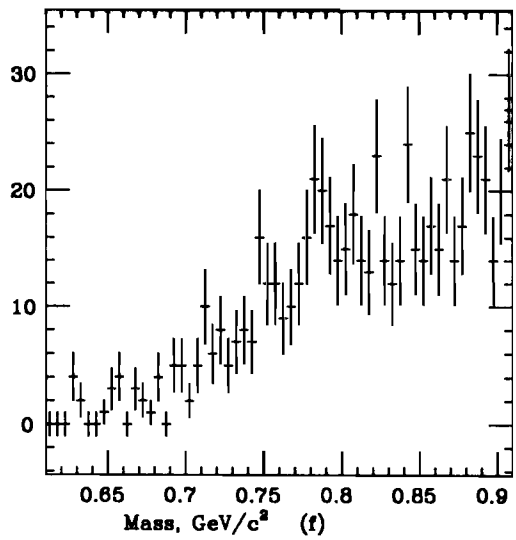

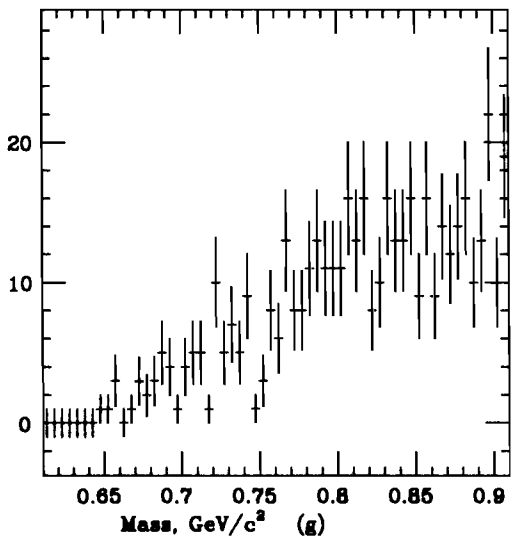

Figure B-6
(continued)
Di-muon production for 0.0 < XF < 1.0
Proton-produced
5 MeV bins
e) 0.4 < Pperp < 0.5
f) 0.5 < Pperp < 0.6
g) 0.6 < Pperp < 0.7

References

1 ABBCCLVW collaboration, Nucl. Phys B vol B118, p360 (1977)

2 M. Aguilar-Benitez et al, CERN-EP/84-73 preprint from CERN (1984)

3 K. Anderson et al, Phys. Rev. Lett. vol 42, p944 (1979)

4 N. Angelov et al, Sov. J. Nucl. Phys. vol 33, p828 (1981)

5 Y. Antipov et al, Sov. J. Nucl. Phys. vol 28, p670 (1978)

6 Y. Antipov et al, Sov. J. Nucl. Phys. vol 32, p348 (1980)

7 Y. Antipov et al, Sov. J. Nucl. Phys. vol 33, p194 (1981)

8 Y. Antipov et al, Sov. J. Nucl. Phys. vol 36, p829 (1982)

9 M. Arneodo et al, Phys. Lett. B vol 149B, p415 (1984)

10 R. Bailey et al, Phys. Lett. B vol 132B, p230 (1983)

11 R. Barate, XVIII Rencontre de Moriond, Gluons and Heavy Flavours, p315 (1983)

12 V. Blobel et al, Phys. Lett. B vol 48B, p73 (1979)

13 J. Branson et al, Phys. Rev. Lett. vol 38, p1331 (1977)

14 J. Branson et al, Phys. Rev. Lett. vol 38, p1334 (1977)

15 Howard Budd, Forward charge distributions associated with with hadronically produced J/psi particles, Thesis, University of Illinois at Urbana-Champaign, (1983)

16 C. Carlson et al, Phys. Rev. D vol 18, p760 (1978)

17 P. Charpentier, XVIII Rencontre de Moriond, Gluons and Heavy Flavours, p323 (1983)

18 L. Chau, Phys. Reports vol 95, p2 (1983)

19 L. Chau et al, Phys. Rev. D vol 29, p592 (1984)

20 L. Chau, Brookhaven preprint, Phenomenology of quark mixing- the b lifetime, CP violation, etc. (1983)

21 L. Chau et al, Brookhaven preprint, CP violation in the partial decay rates of charm and beauty mesons (1984)

22 L. Chau et al, Brookhaven preprint, Comments on the parameterization of the Kobayashi-Maskawa Matrix (1984)

23 P. Chiappetta et al, CPT-84/P.1696 preprint from Centre de Physique Theorique, France (1984)

24 G. Chu et al, Phys. Rev. D vol 10, p3672 (1974)

25 L. Clavelli et al, Phys. Rev. D vol 29, p57 (1983)

26 G. Cosme et al, Phys. Lett. B vol 67B, p231 (1977)

27 B. Cox et al, Phys. Rev. D vol 29, p63 (1984)

28 C. Daum et al, Nucl. Phys. B vol B186, p205 (1981)

29 A. Devoto et al, Phys. Rev. D vol 27, p508 (1983)

30 A. Donnachie et al, Nucl. Phys. B vol B112, p233 (1980)

31 A. Donnachie et al, Z. Physik C vol 4, p231 (1980)

32 A. Donnachie et al, Phys. Lett. B vol 95B, p437 (1980)

33 R. Feynman et al, CALT-68-651 CalTech Preprint (1978)

34 R. Horgan et al, Phys. Lett. B vol 81B, p215 (1979)

35 K. Kinoshita et al, Phys. Lett. B vol 68B, p355 (1977)

36 K. Kinoshita et al, Phys. Rev. D vol 17, p1834 (1978)

37 M. Gaillard et al, Phys. Rev. D vol 10, p897 (1974)

38 M. Gaillard et al, Phys. Rev. D vol 13, p2674 (1976)

39 M. Gluck et al, Phys. Rev. D vol 17, p2324 (1978)

40 M. Gluck et al, Z. Physik C vol 13, p119 (1982)

41 Thomas Graff, Comparison of pion- and proton- production of charmonium, Thesis, University of Illinois at Urbana-Champaign, (1984)

42 H. Grassler et al, Nucl. Phys. B vol B132, pl (1978)

43 M. Grilli et al, Nuovo Cimento vol 13A, p593 (1973)

44 V. Grishin et al, Sov. J. Nucl. Phys. vol 34, p703 (1981)

45 J. deGroot et al, Z. Physik C vol 1, pl43 (1979)

46 Stephen Hahn, Production of charmonium states in 225 GeV/c pi-minus beryllium interactions, Thesis University of Illinois at Urbana-Champaign, (1983)

47 P. Higgins et al, Phys. Rev. D vol 19, p65 (1979)

48 M. Hwang et al, Phys. Rev. D vol 29, pl27 (1984)

49 Kaon cross-sections. CERN-HERA 83-02 (1983)

50 D. Kaplan et al, Phys. Rev. Lett. vol 40, p435 (1978)

51 H. Kirk et al, Nucl. Phys. B vol B128, p397 (1977)

52 T. Kirk, Internal Fermilab E673 Memo, May 21, (1982)

53 T. Kirk, A Multihit Time Encoder System (MUTES), Fermilab, (1979)

54 J. Kuhn, Phys. Lett. B vol 89B, p385 (1980)

55 J. Leveille et al, Nucl. Phys. B vol B147, pl47 (1979)

56 W. Li, Internal Fermilab E673 Memo, Sept 29, (1982)

57 A. Likhoded et al, Sov. Phys. Usp. vol 21, pl (1978)

58 Patrick Lukens, Measurement of chi(3510) and chi(3555) production in 190 GeV/c piminus-beryllium interactions, Thesis, University of Illinois at Urbana-Champaign, (1983)

59 P. Malhotra et al, Z. Physik C vol 18, p53 (1983)

60 R. McElhaney et al, Phys. Rev. D vol 8, p2267 (1973)

61 T. Nunamaker, Nucl. Instr. Meth. vol 106, p557 (1973)

62 J. Owens, Phys. Rev. D vol 30, p943 (1984)

63 A. Para, XVIII Rencontre de Moriond, Gluons and Heavy Flavours, p27 (1983)

64 Pion cross-sections. CERN-HERA 83-01 (1983)

65 J. Pisut et al, Nucl. Phys. B vol B6, p325 (1968)

66 J. Proudfoot, Thesis, Oxford University, (1978)

67 R. Schindler et al, Phys. Rev. D vol 24, p78 (1981)

68 Paul Schoessow, Strange Quark Suppression in 225 GeV/c pi-minus beryllium interactions, Thesis University of Illinois at Urbana-Champaign, (1983)

69 R. Shrock et al, Phys. Lett. B vol 87B, p375 (1979)

70 S. Singh, Phys. Rev. D vol 6, p2646 (1972)

71 J. Varela, XVIII Rencontre de Moriond, Gluons and Heavy Flavours, p383 (1983)

72 H. Wahlen, XVIII Rencontre de Moriond, Gluons and Heavy Flavours, p13 (1983)

73 C. Wohl et al, Review of Particle Properties, April, (1984)

VITA

James Nugent Bellinger was born in New Orleans, Louisiana, on July 29, 1955. In 1973 he graduated from the American Cooperative School in Monrovia, Liberia. He studied at Southern Illinois University in Carbondale from 1973 to 1977, graduating with a Bachelor of Science in physics and a Bachelor of Science in mathematics. He then studied at the University of Illinois at Chicago Circle from 1977 to 1979, graduating with a Master of Science in physics. From 1979 to 1985 he studied at the University of Illinois at Urbana-Champaign, receiving a Ph.D. in physics in 1985. While a graduate student he worked as a teaching assistant for one and a half years, and as a research assistant for five years.